The effect of ionic liquids on the surface and photocatalytic properties of semiconducting materials

Anna Pancielejko [a], Malwina Kroczewska [b], Paweł Mazierski [a], Justyna Łuczak [b], Adriana Zaleska-Medynska [a]*

[a] Department of Environmental Technology, Faculty of Chemistry, University of Gdansk, 80-308 Gdansk, Poland

[b] Department of Process Engineering and Chemical Technology, Faculty of Chemistry, Gdansk University of Technology, 80-233 Gdansk, Poland

Corresponding author:

Adriana Zaleska-Medynska adriana.zaleska-medynska@ug.edu.pl

Abstract

Semiconductor mediated photocatalysis represents an environmentally friendly technology that could be used for the degradation of different pollutants in the gas and aqueous phases, for hydrogen generation, as well as, for CO_2-to-valuable product transformation reactions. Therefore, it is extremely important to accurately design a photocatalyst with the relevant features. In recent years, ionic liquids have often been employed as reagents for the synthesis of these materials. To address the issue of semiconductor-based photocatalytic preparation in the presence of ionic liquids, eight main paths of interaction between ionic liquid with the formed semiconductor particles in the solvothermal process were identified and described based on literature examples. The most critical aspects discussed here are understanding how an ionic liquid may behave during the solvothermal synthesis of semiconductor material particles and how its behavior may ultimately affect the properties of that material, as well as what techniques are available that allow us to assess the nature of this interaction mechanism.

Introduction

Semiconductor mediated photocatalysis utilizes the energy of light to activate a large number of chemical reactions that are thermodynamically uphill reactions under normal conditions, such as pollutant degradation in the gas and liquid phase, hydrogen generation, and CO_2 photoconversion. To optimize reaction conditions and to enhance the efficiency of the above-mentioned reactions a wide spectrum of semiconductors materials have been applied, including metal oxides (e.g. TiO_2, ZnO), metal chalcogenides (ZnS, CdS, CdSe, carbon nitride-based materials (g-C_3N_4), bismuth oxyhalides (BiOX, where X = F, Cl, Br, I), perovskite oxides (ABO_3), metal halide perovskites and double perovskites. The photocatalytic performance of those materials is affected by their structural and surface properties, such as:

(i) morphology;
(ii) surface area and porosity;
(iii) surface composition (dopants, vacancies, impurities);
(iv) electronic band structure (position of valence and conduction band edges and band gap value).

On the other hand, the above-mentioned properties could be designed throughout the introduction of ionic liquids (ILs) during semiconductor particle synthesis. ILs are usually built of large, organic cations and smaller anions, and due to their structure. ionic liquids could interact both with themselves and with other components during the synthesis of nano- and micromaterials. It is known that ILs could play the role of structuring agent through one of the following mechanisms: (*i*) stabilization of growing particles by the formation of a protective layer; (*ii*) stabilization of growing particles by higher viscosity of the ILs; (*iii*) interaction between growing particles and fluoride anions generated *in situ* throughout hydrolysis of IL containing [BF_4] and [PF_6] anions; (*iv*) ILs-based micellar aggregates employed as nanoreactors or soft templates; (*v*) agent promoting reduction of particles' precursor; and (*vi*) soft template for growing particles [1]. Moreover, for TiO_2 particles obtained in the presence of ionic liquids, it was found that the introduction of ILs during the synthesis of semiconductor material could affect their photocatalytic properties [2–9]. Our previous investigation has shown that ionic liquids could induce visible light activity of wide bandgap semiconductors such as TiO_2. Two main mechanisms have been pointed out to be responsible for this photoactivity: (*i*) formation of surface complex between ILs and TiO_2; and (*ii*) generating of mid-bandgap level in the structure of TiO_2 by interaction with non-metal dopants evolved from ionic liquids [10]. These mechanisms of visible light activity induction have been correlated with the stability of the ionic liquids during the solvothermal synthesis of TiO_2. Based on both experimental data and chemoinformatic analysis regarding TiO_2 synthesized in the presence of 23 different ionic liquids, it was found the dependency between the chemical structure of the ionic liquid, its durability at elevated temperature (e.g. condition of solvothermal synthesis) and type mechanism visible light induced photoactivity of finally obtained ILs-TiO_2. Generally, we can conclude that stable ionic liquids (not decomposed during solvothermal synthesis of TiO_2) could contribute into the formation of a charge-transfer (CT) complex between titania facial and adsorbed IL, while unstable ionic liquids (decomposed during solvothermal synthesis of TiO_2) could provide a non-metal atoms to be built into TiO_2 structure as dopants. The effect of ILs on the surface electronic properties of TiO_2 was also cleared up by using the reversed double-beam photoacoustic spectroscopy (RDB-PAS) technique, developed by the Ohtani research group [11]. These measurements added new information, namely the energy-resolved distribution of electron trap (ERDT) and conduction band bottom (CBB), that had not been previously noticed using conventional analysis such as X-ray powder diffraction (XRD) and X-ray photoelectron spectroscopy (XPS). Thus, RDB-PAS demonstrated that ILs are able to promote the formation of a surface amorphous layer shielded by hydrophobic organic residues, resulting in higher adsorption of phenol on the surface and finally higher efficiency of phenol degradation under visible light [12].

Considering the great practical pertinence of the application of ionic liquids for semiconducting photocatalyst preparation, there is already extensive literature on this topic. However, several previous reviews have focused only on selected aspects of these phenomena. Duan at al. [13] collected data on the employment of ILs as the reactant, solvent, and surfactant during the preparation of functional inorganic materials and then tried to verify whether it was an anion or cation from ionic liquids is nearby to the liquid-solid interface between ILs and fabricated material. Benefits of the usage of ILs compared to the employment of Deep Eutectic Solvents (DES) have been presented for the fabrication of both nanostructured TiO_2 [14] and a wider group of nanomaterials [15]. Property modulation of two-dimensional (2D) materials by ILs introduced during synthesis was discussed in relation to materials obtained by exfoliation, application of ILs as the gating layer to increase charge carrier density, as well as usage of ILs to fabricate 2D material electrodes and to boost crystallization process of perovskites in photovoltaic cells [16].

In this review, we collected literature on the preparation of semiconductor photocatalysts in the presence of ionic liquids and, on this basis, we determined the main mechanism for inducing photoactivity of the obtained materials, related to the presence of ionic liquids. The gathered data showed us that there are eight main ways in which ionic liquids can increase the photoactivity of semiconductors both when excited by UV and Vis radiation. As presented in Figure 1, ILs could control photoactivity throughout:

1. creation of new energy states by doping elements originated from ionic liquid (dopant presence could provoke an apparent narrowing of the semiconductor band gap and/or inhibit electrons and holes recombination);
2. surface defect formation throughout interaction between ionic liquid and growing semiconductor particles (surface defects affect recombination of photoinduced electron-hole pairs, cause an apparent narrowing of the semiconductor band gap, and provide additional active sites for catalytic reactions);
3. facilitating the charge transfer by enabling the formation of heterojunction in composite materials;
4. presence of surface complex able to absorb visible light throughout adsorption and chemical interactions between ionic liquids and semiconductor outer;
5. creation of specific facets beneficial for photocatalytic reaction;
6. affecting semiconductor particles size and porosity;
7. surface modification by the presence of ionic liquids at the surface of semiconductor materials affecting the interaction between the semiconductor surface and components of the reaction mixture (e.g. sorption properties);
8. controlling the thickness of synthesized materials towards obtaining ultrathin 2D materials (it results in shorter diffusion paths, faster charge carrier transport, and finally reduces the likelihood of charge carriers recombination).

Tables 1 to 8 present data collected from selected research articles regarding semiconductor photocatalysts manufacturing in the presence of ionic liquids. We decided to compile the data only from articles on the basis of which it is possible to clearly determine how the ionic liquids affect the photoactivity of the obtained semiconductor. In the following sections, we briefly discuss the principles of each of the mechanisms presented in Figure 1 and mentioned above with reference to specific examples. In the final part of each section, “known” and “unknown” facts regarding the specific impact of ionic liquids on the presented photoexcitation mechanism are summarized.

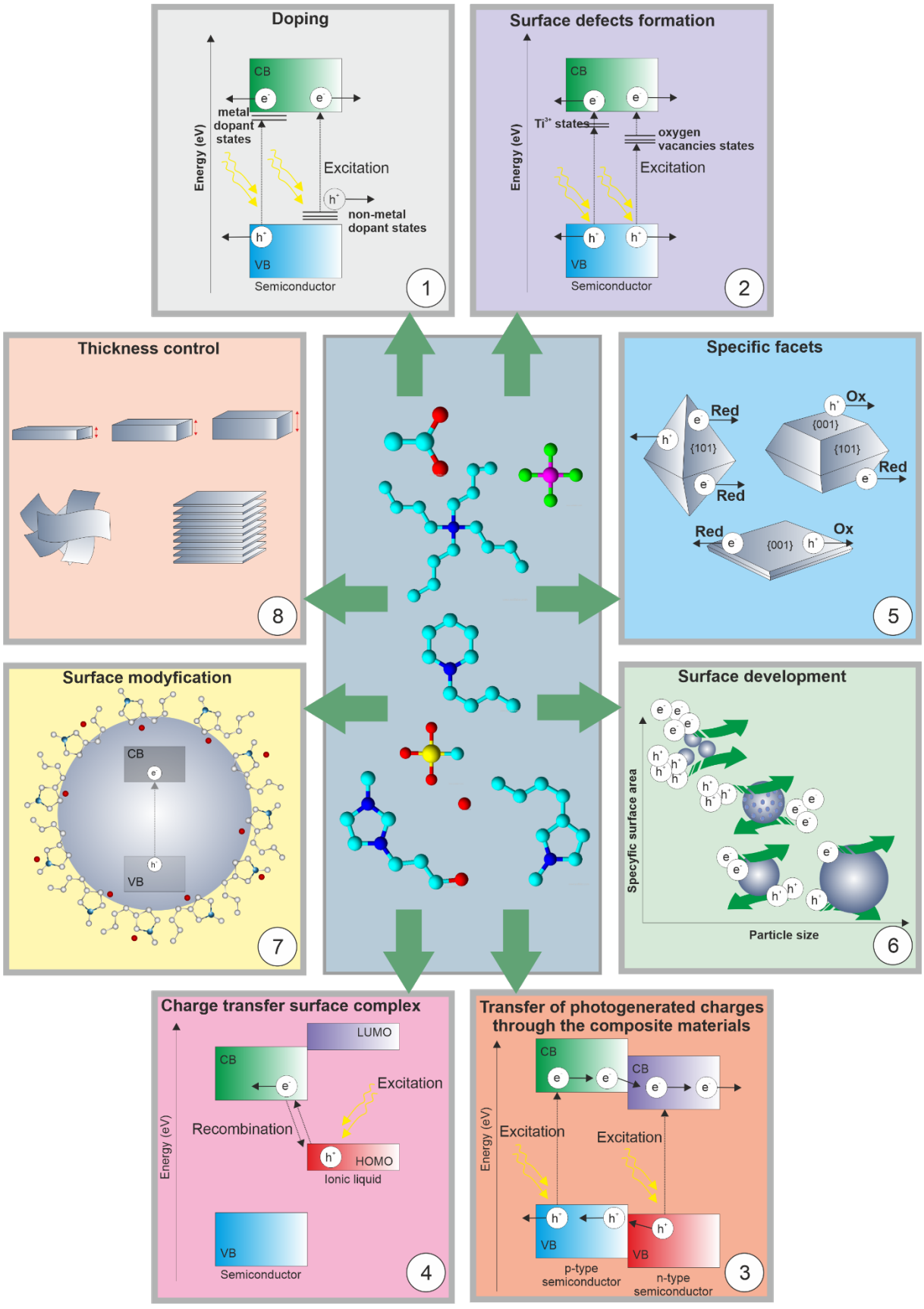

Figure 1. The main paths in which ionic liquids impact the properties of semiconductors and the mechanism of their photoexcitation

1) Doping elements originated from ionic liquid

Semiconductors with weak visible-light activity (*i.e.* having a bandgap ≥ 3 eV) can be modified by metallic or non-metallic elements to extend the wavelength of photoabsorption towards the visible region. The term "doping" means the incorporation of atoms or ions into the material's crystal lattice, that is, modification of the bulk structure of crystallites, but not modification of the surface[17]. The dopants, either through substitution or interstitial doping (or both), modulate the material's electronic structure. Doping may induce the formation of local intraband energy states (e.g. oxygen vacancy, OV) that become centers of optical excitation and relaxation[18,19]. These states should overlap with the band states of the semiconductor to transfer photoexcited carriers to the reactive sites at the catalyst surface within their lifetime[20]. Excitations from the localized states to conduction band (CB) may account for the extended absorption tail of absorption curve to the longer wavelengths with respect to undoped semiconductors (UV region)[21]. Another effect caused by doping is shifting the position of the conduction or valence band (VB), thereby narrowing the bandgap without introduction of any local states. In this case, a red-shift of the entire absorption edge toward the longer wavelength is observed, which favorably affects both light absorption and photocatalytic activity[22]. Absorption in the visible light region can also be attributed to dopant-induced defects, including surface reconstruction[23] and lower recombination rate of charge carriers[24].

Ionic liquid is most often used as an additive to the reaction medium in which the semiconductor is obtained. If IL decomposes under the synthesis conditions used, it becomes a source of non-metallic, e.g., B[25,26], N [7,27,28], F[29], I[30], P [31], C[26,28,32], S[33], Cl [34] or metallic species Fe [17,35] which may be embedded in the semiconductor structure. Studies conducted so far (summarized in Table 1) indicate that doped elements (one or more) were derived from the decomposition of the following ILs' cations: 1-ethyl-3-methylimidazolium[28,29,36], 1-butyl-3-methylimidazolium[25–27,30,31,33], 1-methyl-3-octylimidazolium[34,35,37], 1-butylpyridinium[7] or the ILs' anions: tetrafluoroborate[25–27,29], hexafluorophosphate[31], tetrachloroferrate[34,35], iodide[30], chloride[7,28,33,36].

Doping of elements in the crystal lattice can be proved through various techniques such as XPS (analysis of valency of doped elements)[17], XRD (shifts in diffraction peaks)[38], UV-vis absorbance spectra[39], or first-principles calculations[20], whereas photocatalysis by doped photocatalysts by the action spectrum analysis (analysis of resemblance of absorption and actions spectra)[40]. Yu *et al.* [26] used the XPS technique to confirm the substitutional (signal at 197.0 eV) and interstitial (signal at 193.6 eV) doping of B atoms derived from 1-butyl-3-methylimidazolium tetrafluoroborate into the TiO_2 lattice (formation of B-Ti species). In addition, the peak at 281.1 eV was assigned to the O-Ti—C bonds, resulting from the substitution of the oxygen atom with carbon. The XPS analysis also revealed the presence of the Ti^{3+} species in the titania structure, which according to the authors, facilitates the transition of photogenerated electrons and reduces the electron–hole recombination rate. However, the UV-Vis spectra performed for this material did not reveal a redshift of the absorption, which was concluded by the lack of band narrowing in doped TiO_2. The shift of the absorption edge toward the higher wavelength, in contrast, was observed for F-doped Pt/TiO_2 [29] (1-ethyl-3-methylimidazolium tetrafluoroborate was a source of fluoride) and N-doped TiO_2 [28,36] (N was derived from 1-ethyl-3-methylimidazolium chloride) compared to P25 TiO_2 used as a reference material.

Known: methods of using IL to incorporate non-metals into semiconductor lattices; examples of IL susceptible to decomposition during synthesis and being a source of dopants.

Unknown: effect of the IL-derived doping on the electronic structure of the material (band gap narrowing and/or localized states formation); conditions under which IL-derived mono- and codoping occurs; amount and distribution of doped elements, stability of the doped material under photocatalytic reaction condition, possibility of surface reconstruction.

Table 1. *Category: doping.* Preparation conditions, morphology, photocatalytic performance of photocatalysts prepared by ILs-assisted synthesis methods*,**.

Explanation of abbreviations used below in the column:
- *surface properties*: diameter (φ), thickness (th), length (l), width (w), crystallite size (D) specific surface area (S_{BET}), pore volume (V_p), pore size (φ_p), aspect ratio,
- *conditions*: photocatalyst content (C_{phot}), the concentration of model pollutant (C_0), sacrificial agent (sacr. agent), volume of solution (Vs), irradiation time (t),
- *efficiency:* yield (Y)/rate (r)/rate constant (*k*) of the most active sample (Y), and the reference sample (Y_{ref}), ↗ - increase, and ↘ decrease compared to the reference sample.

*The table includes all available information.
**The original sample label is given in italics.

Photocatalyst and original sample label	Ionic liquid and its role in the synthesis	Synthesis method	Surface properties	Photocatalytic performance				Mechanism details	Ref.
				Type of model reaction	Conditions	Light source	Yield (Y)/rate (r)/rate constant (*k*)		
TiO_2 *3TA400*	1-butyl-3-methylimidazolium tetrafluoroborate additive	microwave assisted synthesis	nanoparticles φ = ~10 nm S_{BET} = 99.71 m^2/g	Methyl orange degradation	C_{phot} = 1 g/L C_0 = 10 mg/L V_s = 200 mL t = 100 min	300 W Xe lamp (>400 nm)	Y = 84.2% *k* = 0.0173 1/min Y_{ref} = ~16% k_{ref} = 0.0014 1/min ↗	· doping by B, F; · band gap narrowing;	25
TiO_2	1-butyl-3-methylimidazolium tetrafluoroborate solvent	ammonia-driven hydrolysis of a titanium precursor in IL	rutile nanorods l = 5–20 mm th = 200–500 nm	Congo red degradation	C_{phot} = 1.2 g/L C_0 = 10 mM V_s = 10 mL t = 15 min	30 W (λ_{max} = 253 nm)	Y = 73% Y_{ref} = 18% (P25) ↗	· doping by N, C, F;	27
					C_{phot} = 1.2 g/L C_0 = 10 mM V_s = 10 mL t = 15-30 min	30 W (λ_{max} = 575 nm)	Y = 56% Y_{ref} = 9% (P25) ↗		
TiO_2 *T_{IL}-300*	1-butyl-3-methylimidazolium tetrafluoroborate additive	hydrothermal	nanocrystals	Rhodamine B degradation	C_{phot} = 2 g/L C_0 = 10^{-2} mM V_s = 20 mL t = 120 min	300 W Xe lamp (>420nm) 20 $mWcm^{-2}$	Y = ~100% Y_{ref} = ~50% ↗	· doping with B, C; · formation of Ti^{3+};	26
TiO_2 *TiO2_BenMIM(1:2)*	1-benzyl-3-methylimidazolium chloride N source and morphology directing agent	solvothermal	microparticles φ = 1.0-2.0 mm S_{BET} = 215 m^2/g	Phenol degradation	C_{phot} = 5 g/L C_0 = 0.21 mM V_s = 25 mL t = 60 min	1000 W Xe lamp (>420 nm)	Y = 44% r = 1.4 mmol/(dm^3·min) Y_{ref} = 13% r_{ref} = 0.4 mmol/(dm^3·min) ↗	· doping with N; · formation of Ti^{3+};	7

TiO_2 *TiO_2_BPy(1:3)*	1-butylpyridinium chloride N source and morphology directing agent						Y = 60% r = 2.3 mmol/(dm^3·min) Y_{ref} = 13% r_{ref} = 0.4 mmol/(dm^3·min) ↗		
TiO_2 *TiO_2_BMPyr(1:5)*	1-butyl-1-metylpyrrolidinium chloride N source and morphology directing agent						Y = 49% r = 1.7 mmol/(dm^3·min) Y_{ref} = 13% r_{ref} = 0.4 mmol/(dm^3·min) ↗		
TiO_2 *TiO_2_TBA(1:2)*	tetrabutylammonium chloride N source and morphology directing agent						Y = 46% r = 1.5 mmol/(dm^3·min) Y_{ref} = 13% r_{ref} = 0.4 mmol/(dm^3·min) ↗		
TiO_2 *N-TiO_2-600*	1-ethyl-3-methylimidazolium chloride N source and mesoporous template	solvent evaporation induced self-assembly	S_{BET} = 54 m^2/g	H_2 generation	C_{phot} = 1.3 g/L sacr. agent = MeOH V_s = 155 mL t = 360 min	450 W Xe lamp (>400 nm)	r = 39.1 mmol/(g·h) r_{ref} = ~3 mmol/(g·h) ↗	· doping with N;	36
TiO_2 *CNMT-0.75*	1-ethyl-3-methylimidazolium chloride C, N sources and a mesopore creator	solvent evaporation induced self-assembly	S_{BET} = 101 m^2/g	H_2 generation	C_{phot} = 1.3 g/L sacr. agent = MeOH V_s = 155 mL t = 360 min	450 W Xe lamp (>420 nm)	r = ~83 mmol/(g·h) r_{ref} = ~7 mmol/(g·h) ↗	· doping with N,C; · higher BET surface area; · smaller crystallite size;	28
TiO_2 *F-Pt/TiO_2*	1-ethyl-3-methylimidazolium tetrafluoroborate F source$^-$	solvothermal	nanocrystals φ = 10 nm	H_2 generation	C_{phot} = 1 g/L sacr. agent = TEOA V_s = 10 mL t = ~48h	300 W Xe lamp	r = 4399 mmol $r_{ref\ (P25)}$ = 517 mmol ↗	· doping with F	29
BiOCl *Fe/BiOCl*	1-methyl-3-octylimidazolium tetrachloroferrate source of Cl and Fe,	solvothermal	porous microspheres φ = 1 μm S_{BET} = 38.3 m^2/g	Methylene blue degradation	C_{phot} = 0.2 g/L C_0 = 10 mg/L + 3ml H_2O_2 30wt.% V_s =100 mL t = 75 min	300 W Xe lamp, (>400 nm)	Y = 90.3% Y_{ref} = 22% ↗	· doping with Fe^{3+}	34

	template			Rhodamine B degradation	C_{phot} = 0.2 g/L C_0 = 10 mg/L V_s =100 mL t = 25 min		Y = 75% Y_{ref} = 20.9% ↗		
				Bisphenol A degradation	C_{phot} = 0.5 g/L C_0 = 10 mg/L + 3ml H_2O_2 30wt.% V_s =100 mL t = 210 min		Y = 98% Y_{ref} = 50% ↗		
$Bi_2O_2CO_3/Bi_2WO_6$ *0.3I-$Bi_2O_2CO_3/Bi_2WO_6$*	1-butyl-3-methylimidazolium iodide I source	solvothermal	microspheres S_{BET} = 27.73 m^2/g	H_2 generation	C_{phot} = 0.5 g/L sac. agent 10 vol% MeOH, V_s = 50 mL 3% Pt, t = 3 h	H_2: 300 W Xe arc lamp (≥420 nm) TC, RhB: 500 W Xe lamp (380 nm < λ < 780 nm)	Y = 186.22 mmol/(g·h) Y_{ref} = ~30 mmol/(g·h) ↗	· doping with I; · lower electron-hole recombination;	30
				Tetracycline degradation	C_{phot} = 0.50 g/L C_0 = 20 mg/L V_s = 50 mL t = 60 min		Y = 80% Y_{ref} = ~70% ↗		
				Rhodamine B degradation	m_{phot} = 50 mg C_0 = 10 mg/L V_s = 50 ml t = 120 min		Y = 99.9% Y = 10.9% ↗		
$BiPO_4$ *C-$BiPO_4$-2*	1-methyl-3-octylimidazolium dihydrogen phosphate C source	solvothermal	rod-like structure l = 80 nm w = 30 nm	4-chlorophenol degradation	C_{phot} = 0.30 g/L C_0 = 10 mg/L V_s = 100 mL t = 120 min	250 W Hg lamp	Y = 82.7% k = 0.0519 1/min Y_{ref}=58.1% k_{ref}=0.0333 1/min ↗	· doping with C; · lower electron-hole recombination;	37
ZnO *S-1*	$[MIM]\{(CH)_2\}_3[MIM](SCN)_2$ source of S^{2-}, templating agent, and modifier of ionic force during reaction	hydrothermal	cactus-like ZnO_xS_{1-x} nanostructures S_{BET} = 25.15 m^2/g	Methyl orange degradation	C_{phot} = 0.5 g/L V_s =80 mL t = 450 min	30 W high-pressure Hg lamp	Y = 100% Y_{ref} = 100% after longer irradiation time ↗	· doping of S^{2-} ions; · higher number of oxygen vacancies; · higher number of crystallite defects;	32

g-C_3N_4 *7.8% CN-Cl*	1-butyl-3-methylimidazolium chloride additive, Cl source	calcination	layered, cavity structure;	Rhodamine B degradation	C_{phot} = 1 g/L C_0 = 10 mg/L t = 90 min	500 W Xe lamp (>420 nm)	Y = ~95% k = 0.02888 1/min Y_{ref} = ~60% ↗	· intercalation of chlorine	33
g-C_3N_4 *Fe-CN-2*	1-methyl-3-octylimidazolium tetrachloroferrate Fe source	wet impregnation	thin sheets	Rhodamine B degradation	C_{phot} = 0.2 g/L C_0 = 10 mg/L V_S = 100 mL t = 150 min	300 W Xe lamp (>400 nm)	Y = 96% k = 0.0182 1/min Y_{ref} = 74% ↗	· doping with Fe	35
g-C_3N_4 *3%-P/g-C_3N_4*	1-butyl-3-methylimidazolium hexafluorophosphate P source	calcination	sheet structure φ_{pores} = 55-80 nm	Tetracycline degradation	C_{phot} = 1 g/L C_0 = 50 mg/L V_S = 50 mL t = 120 min	300 W Xe lamp (>385 nm)	Y = 85% k = 0.01544 1/min Y_{ref} = 40% ↗	· doping with P	31
				Methylene blue degradation	C_{phot} = 1 g/L C_0 = 50 mg/L V_S = 50 mL t = 120 min		Y = 80% k = 0.0082 1/min Y_{ref} = 30% ↗		

2) Surface defects formation

The atomic structure of photocatalysts, when disrupted or compromised, can lead to the formation of defects that can play a crucial role in influencing their optical, electronic, and photocatalytic properties. Defects (e.g., oxygen, and sulfur vacancies) can act as active sites for photocatalytic reactions. This enhancement stems from the defects' ability to curtail the recombination of photoinduced electron-hole pairs, narrow the energy band, and provide additional active sites for catalytic reactions[41]. Among the most prevalent defects in oxide photocatalysts are oxygen vacancies (OVs), typically intrinsic in nature. These vacancies form when oxygen atoms within the crystalline structure undergo partial reduction, introducing two extra electrons[42]. The generation of OVs can occur during crystal growth, through the introduction of dopants, or as a consequence of specific crystal phase formations. Manipulating the concentration of OVs within photocatalysts is achievable through various means, such as modifying synthesis conditions employing post-synthesis treatments like annealing at specific temperatures, adjusting synthesis atmospheres, or subjecting the material to irradiation. These strategies offer a feasible approach to control and regulate the concentration of OVs, thereby influencing the overall photocatalytic performance of the material.

The role of ILs in the synthesis of TiO_2 materials wherein the interaction between the ILs and TiO_2 induces the intentional formation of oxygen vacancies has gained much attention. The induction of oxygen vacancies in TiO_2 is a pivotal step in the generation of Ti^{3+} species. So far, ILs such as 1-decyl-3-methylimidazolium chloride[2], 1-benzyl-3-methylimidazolium chloride[7], 1-butyl-1-metylpyrrolidinium chloride[7], 1-butylpyridinium chloride[7], tetrabutylammonium chloride[7], 1-methylimidazolium tetrafluoroborate[43], 1-butyl-3-methylimidazolium tetrafluoroborate[3,44,45], 1-butyl-3-methylimidazolium chloride[2,44], 1-ethyl-3-methylimidazolium tetrafluoroborate[3], and 1-methyl-3-octylimidazolium tetrafluoroborate[3] have been used.

The formation of defects on the surface of other photocatalysts (e.g., ZnO, BiOBr, BiOI, $BiVO_4$) has been observed in the presence of 1-ethyl-3-methylimidazolium bromide[46], 1-butyl-3-methylimidazolium bromide[46–48], 1-hexyl-3-methylimidazolium bromide[46], 1-methyl-3-octylimidazolium bromide[46–48], 1-hexadecyl-3-methylimidazolium chloride[49], tetrabutylammonium hydroxide[50], tetrabutylphosphonium hydroxide[51], 1-cetyl 3-methylimidazolium bromide[47,48], 1-dodecyl-3-methylimidazolium bromide[47,48], 1-butyl-3-methylimidazolium tetrafluoroborate[48], 1-butyl-3-methylimidazolium hexafluorophosphate[48], 1-methoxyethyl-3-methylimidazolium bromide[52], 1-octyl-3-methylimidazolium copper trichloride[53], 3-butyl-1-methylimidazolium tetrachlorobismate[54], 3-butyl-1-methylimidazolium vanadate[54], 3-(2-methoxyethyl)-1-methylimidazolium tetrachlorobismate[54], 3-(2-methoxyethyl)-1-methylimidazolium vanadate[54], 1-ethyl-3-methylimidazolium iodide[55], 1-ethyl-3-methylimidazolium dihydrogen phosphate[56], 1-butyl-3-methylimidazolium chloride[49], and 1-ethyl-3-methylimidazolium tetrafluoroborate[57]. Within Table 2, we have highlighted various examples where ILs have contributed to creating defects or local distortions.

The influence of ILs on the formation of defects was corroborated and validated through multiple spectroscopic techniques, including Electron Paramagnetic Resonance (EPR), Electron Spin Resonance (ESR), Photoluminescence (PL) spectroscopy, and XPS. Based on them, it can be stated that the surface defects, specifically Ti^{3+}, are attributed to the contribution of ILs, both imidazolium[2,44], and non-imidazolium ones[7]. The ILs contribute to incorporating Ti^{3+}into the bulk TiO_2 through the partial decomposition of the imidazolium cation and the hydrolysis of anion[43]. The partial decomposition of ILs results in the co-

adsorption of decomposed elements and surface modification (e.g., Ti-O-N species)[3,7,45]. This indicates that ILs are involved in the initial stages of synthesis and influence the composition of the final TiO_2 product. It is confirmed that the IL precursor plays a pivotal role in dictating the morphology, and crystallinity, and the growth mechanism is intricately linked to electrostatic interactions with IL cations[46,50,52]. The incorporation of ILs enhances photocatalytic performance through the formation of defects and the influence of alkyl chain size[49,54].

However, in the case of other photocatalysts than TiO_2, the role and importance of the use of ILs in relation to the defects is much less discussed. It is unclear on what basis ILs, which potentially contribute to the formation of defects, while their interaction with precursor materials and reaction conditions may influence the defect formation process, are selected. There is a lack of information about the behavior of ILs in the reaction medium. Understanding the fate of ILs during the synthesis process and developing methods to remove any residual ILs or by-products is crucial for ensuring the purity and functionality of the final materials. Further research in this area is essential to understand the dynamics of ILs during synthesis, their impact on defect formation, and the steps needed to ensure the removal of any residual ILs.

Known: contribute to surface defects formation (particularly Ti^{3+}); facilitate the incorporation of Ti^{3+} into bulk TiO_2 through imidazolium cation decomposition and anion hydrolysis; partial IL decomposition leads to co-adsorption (Ti-O-N species); influence the initial synthesis stages, shaping the composition of the final product; determines morphology, crystallinity, and growth mechanism via electrostatic interactions.

Unknown: role in formation and photoactivity other than TiO_2 photocatalysts; basis for ILs selection (what properties are the most important, how they interact with precursor materials, and how reaction conditions influences the defect formation process).

Table 2. *Category: surface defects formation.* Preparation conditions, morphology, photocatalytic performance of photocatalysts prepared by ILs-assisted synthesis methods*, **.

Explanation of abbreviations used below in the column:
- *surface properties*: shape (s), diameter (φ), thickness (th), length (l), width (w), crystallite size (D) specific surface area (S_{BET}), pore volume (V_p), pore size (φ_p), aspect ratio,
- *conditions*: photocatalyst content (m_{phot}), the concentration of model pollutant (C_0), sacrificial agent (sacr. agent), volume of solution (Vs), irradiation time (t),
- *efficiency:* yield (Y)/rate (r)/rate constant (*k*) of the most active sample (Y_{phot}), and the reference sample (Y_{ref}), ↗ - increase, and ↘ decrease compared to the reference sample.

*The table includes all available information.
**The original sample label is given in italics.

Photocatalyst and original sample label**	Ionic liquid and its role in the synthesis	Synthesis method	Surface properties	Photocatalytic performance				Mechanism details	Ref.
				Type of model reaction	Conditions	Light source	Yield (Y)/rate (r)/rate constant (*k*)		
TiO_2 *$TiO_{2\text{-}F\ vacuum}$*	1-butyl-3-methylimidazolium tetrafluoroborate additive	solvothermal microwav	cube-like or truncated octahedral bipyramidal nanocrystals φ = 20 nm D = 20.2 nm φ_p = 11.68 nm V_p = 0.23 cm^3/g S_{BET} = 94.13 m^2/g	Methylene blue degradation	C_{phot} = 2 g/L C_0 = 20 mg/L V_s = 100 mL t = 90 min	300 W Xe lamp (>400 nm)	Y = 97.3% Y_{ref} =46.8% ↗	· formation of Ti^3 · shorted diffusion length · lower electron-hole recombination	44
TiO_2 *S_6*			cube-like or truncated octahedral bipyramidal nanocrystals φ = 20 nm D = 20.3 nm φ_p = 11.68 nm V_p = 0.23 cm^3/g S_{BET} = 94.13 m^2/g	Benzyl alcohol oxidation	C_{phot} = 1 g/L C_0 = 0.01 mmol V_s = 20 mL t = 90 min		Y = ~23 mmol/g Y_{ref} = ~5 mmol/g ↗		
TiO_2 *$TiO_{2\text{-}Cl}$*	1-butyl-3-methylimidazolium chloride additive		nanorods φ = 20 nm D = 13.5 nm φ_p = 8.81 nm V_p = 0.33 cm^3/g S_{BET} =	Methylene blue degradation	C_{phot} = 2 g/L C_0 = 20 mg/L V_s = 100 mL t = 90 min		Y = ~52% Y_{ref} = 46.8%		

			129.12 m^2/g						
TiO_2 *HDM-TiO_2*	1-butyl-3-methylimidazolium tetrafluoroborate additive	solvothermal	microspheres l = 15–25 nm φ_p = 4-20 nm S_{BET} = 131 m^2/g	Methylene blue degradation	C_{phot} = 0.2 g/L C_0 = 0.02 mg/L V_s = 100 mL	300 W	k= 1.54x10^{-3} min^{-1} k = 0.46 x 10^{-3} min^{-1} ↗	· more OVs · increased specific surface area	45
TiO_2 *TiO_2_B(1:2)*	1-butyl-3-methylimidazolium chloride additive	solvothermal	microparticles φ = 0.5-4.0 mm D = 7.2 nm V_p = 0.059 cm^3/g S_{BET} = 202 m^2/g	Phenol degradation	m_{phot} = 7.5 mg C_0 = 0.43 mM t = 80 min	150 W Hg lamp	r = 5.9 µmol·dm^{-3}·min^{-1} r_{ref} = 5.2 µmol·dm^{-3}·min^{-1} ↗	· higher content of Ti^{3+} · smaller particles · higher crystallinity · larger BET surface area · more regular and smooth shape	2
TiO_2 *TiO_2_D(1:2)*	1-decyl-3-methylimidazolium chloride additive		microparticles φ = 0.5-4.0 mm D = 8.4 nm V_p = 0.065 cm^3/g S_{BET} = 218 m^2/g		m_{phot} = 7.5 mg C_0 = 0.43 mM t = 80 min		r = 5.5 mmol·dm^{-3}·min^{-1} r_{ref} = 5.2 mmol·dm^{-3}·min^{-1} ↗		
TiO_2 *TiO_2_BenMIM(1:2)*	1-benzyl-3-methylimidazolium chloride additive	solvothermal	microparticles φ = 1.0-2.0 mm D = 54 nm V_p = 0.101 cm^3/g S_{BET} = 207 m^2/g	Phenol degradation	C_{phot} = 5 g/L C_0 = 0.21 mM V_s = 25 mL t = 60 min	1000 W Xe lamp (>420 nm)	Y = 44% r = 1.4 µmol·dm^{-3}·min^{-1} Y_{ref}=13% r_{ref} = 0.4 µmol·dm^{-3}·min^{-1} ↗	· higher content of Ti^{3+} · doping of N · OVs formation	7
TiO_2 *TiO_2_BMPyr(1:5)*	1-butyl-1-metylpyrrolidinium chloride additive		microparticles φ = 1.0-2.0 mm D = 57 nm V_p = 0.104 cm^3/g S_{BET} = 213 m^2/g				Y = 49% r =1.7 µmol·dm^{-3}·min^{-1} Y_{ref}=13% r_{ref} = 0.4 µmol·dm^{-3}·min^{-1} ↗		
TiO_2 *TiO_2_BPy(1:3)*	1-butylpyridinium chloride additive		microparticles φ=1.0-2.0 mm D=43 nm V_p=0.105 cm^3/g S_{BET} = 215 m^2/g				Y = 60% r = 2.3 µmol·dm^{-3}·min^{-1} Y_{ref} = 13% r_{ref} = 0.4 µmol·dm^{-3}·min^{-1} ↗		

TiO_2 *TiO_2_TBA(1:2)*	tetrabutylammonium chloride additive		microparticles φ = 1.0-2.0 mm D = 58 nm V_p = 0.100 cm^3/g S_{BET} = 209 m^2/g				Y = 46% r = 1.5 μmol·dm^{-3}·min^{-1} Y_{ref} = 13% r_{ref} = 0.4 μmol·dm^{-3}·min^{-1} ↗		
TiO_2 *Ti^{3+}/TiO_2*	1-methylimidazolium tetrafluoroborate additive	solvothermal	microparticles φ = 20-30 mm	Rhodamine B degradation	C_{phot} = 1 g/L C_0 = 10 mg/mL V_s = 50 mL t = 240 min	300 W Xe (>420 nm)	Y = 40% Y_{ref} = ~32% (P25)	· formation of Ti^3 · formation of OV · narrower the energy band gap · lower electron-hole recombination	43
						300 W Xe	Y = 91% Y_{ref} = no data		
TiO_2 *Pt-Ti^{3+}/TiO_2*				H_2 generation	C_{phot}=1 g/L sacr. agent=MeOH V_s = 50 mL t = 240 min	300 W Xe	r = 0.26 mmol h^{-1} m^{-2} r_{ref} = 0.13 mmol h^{-1} m^{-2} ↗		
TiO_2 *NTs-[BMIM]*	1-butyl-3-methylimidazolium tetrafluoroborate F source	anodic oxidation of Ti foil	nanotubes D = 39 nm l = 0.45 μm φ = 120 nm	Phenol degradation	4 cm^2 of TiO_2 NTs C_0 = 0.21 mM V_s = 10 mL t = 60 min	1000 W Xe lamp (420 nm)	UV-Vis: r = 1.26 mmol/(dm^3·min) Vis: r = 0.30 mmol/(dm^3·min) r_{ref} = no data	· formation of Ti^3 · N and B doping · length control · larger surface area	3
TiO_2 *NTs-[EMIM]*	1-ethyl-3-methylimidazolium tetrafluoroborate F source		nanotubes D = 33 nm l = 0.35 μm φ = 120 nm				UV-Vis: r = 1.00 mmol/(dm^3·min) Vis: r = 0.20 mmol/(dm^3·min) r_{ref} = no data		
TiO_2 *NTs-[OMIM]_90V*	1-methyl-3-octylimidazolium tetrafluoroborate F source		nanotubes D = 36 nm l = 0.85 μm φ = 120 nm				UV-Vis: r = 1.82 mmol/(dm^3·min) Vis: r = 0.63 mmol/(dm^3·min) r_{ref} = no data		
ZnO *Sample 1*	1-ethyl-3-methylimidazolium bromide morphology controlling agent	solid-state	nanorods φ=50-100 nm l=1500-2500 nm S_{BET}=23.50 m^2/g	Rhodamine B degradation	C_{phot} =0.4 g/L C_0 =10^{-5} M V_s=100 mL t = 100 min	125 W high-pressure Hg lamp	Y = 100% Y_{ref} = no data	· defect-related green-yellow emission	46

ZnO *Sample 2*	1-butyl-3-methylimidazolium bromide morphology controlling agent		nanorods φ =50-100 nm l = 1000-1500 nm				no data		
ZnO *Sample 3*	1-hexyl-3-methylimidazolium bromide morphology controlling agent		nanorods φ = 50-100 nm l = 500-1000 nm				no data		
ZnO *Sample 4*	1-methyl-3-octylimidazolium bromide morphology controlling agent		nanorods φ = 40-60 nm, l = 200 nm S_{BET} = 32.10 m^2/g				Y = 100% Y_{ref} = no data		
ZnO *ZnO/C440*	1-butyl-3-methylimidazolium chloride incorporation agent	Microwave-assisted hydrothermal	flower-like φ = 0.919 μm $φ_p$ = 13 nm V_p = 0.029 cm^3/g D = 152.3 nm S_{BET} = 8.3 m^2/g	Rhodamine B degradation	C_{phot} = 1g/L C_0 = 10^{-5} M V_s = 50 mL t = 60 min	6 lamps 15 W each	Y = 47% k = 0.00523min^{-1} Y_{ref} = 30% k_{ref} = 0.00501 min^{-1} ↗	· conversion shallow defects into deep defects	49
ZnO *ZnO/C1640*	1- hexadecyl-3-methylimidazolium chloride incorporation agent		flower-like φ = 0.778 μm $φ_p$ =14 nm V_p = 0.064 cm^3/g D = 126.9 nm S_{BET} = 17.3 m^2/g				Y = 62% k = 0.00954 min^{-1} Y_{ref} = 30% k_{ref} = 0.00501 min^{-1} ↗		
ZnO *ZnO nano-bundles*	1-ethyl-3-methylimidazolium tetrafluoroborate morphology controlling agent	solvothermal	microbundles of nanorods φ = 100-150 nm l = 2-4 μm S_{BET} = 36.6 m^2/g	Methyl orange degradation	C_{phot} = 0.4 g/L C_0 = $5 \cdot 10^{-5}$M V_s = 100mL t = 100 min	125 W high-pressure Hg lamp	Y = 100% Y_{ref} = no data	· OVs presence	57

ZnO	tetrabutylammonium hydroxide adsorbing microwave and acting as solvent, reactant, template	Microwave	microspheres φ = 50-200 nm	Rhodamine B degradation	C_{phot} = 0.6 g/L C_0 = 1.5·10^{-5} mol/L V_s = 50 mL t = 120 min	120 W mercury lamp	Y = ~90% Y_{ref} = no data	· large amount of oxygen defect · large number of defect states	50
ZnO ZnO-5	tetrabutyl-phosphonium hydroxide hydrolyzing agent	Hydrolysis	rods φ = 9 nm l = 21 nm S_{BET} = 96.7 m^2/g	Rhodamine 6G degradation	C_{phot} = 0.33 g/L C_0 = 3 mg/L V_s = 3 mL t = 120 min	UV light irradiation (350 nm)	k = ~0.035 min^1 k_{ref} = no data	· larger amount of OV · high BET surface area	51
				Crystal violet degradation			k = ~0.084 min^1 k_{ref} = no data		
BiOBr *BiOBr-C4*	1-butyl-3-methylimidazolium bromide Br source, template, and solvent	solvothermal	tremella-ball-like structures φ = 2–4 mm	Methyl orange degradation	C_{phot} = 1 g/L C_0=10 mg/L V_s = 100 mL t = 270 min	300 W Xenon lamp (>420 nm)	Y = 94.0% Y_{ref}=no data	· OV formation	47
BiOBr *BiOBr-C16*	1-cetyl-3-methylimidazolium bromide Br source, template, and solvent		-				Y = 69.2% Y_{ref} = no data		
BiOBr *BiOBr-C12*	1-dodecyl-3-methylimidazolium bromide Br source, template, and solvent		-				Y = 83.5% Y_{ref} = no data		
BiOBr *BiOBr-C8*	1-methyl-3-octylimidazolium bromide Br source, template, and solvent		-				Y = 85.1% Y_{ref} = no data		
BiOBr *BiOBr-C$_4$-Br*	1-butyl-3-methylimidazolium bromide	Solvothermal	tremella-ball-like structures φ = 2–4 mm	Methyl orange degradation	C_{phot} = 1 g/L C_0 = 10 mg/L V_s = 100 mL	300 W Xenon lamp	Y = 94.0% k = 0.0098 min^{-1} Y_{ref} = no data`	· OV formation · specific facets	48

	Br source				t = 270min	(>420 nm)		· lower electron hole separation	
				Tetracycline degradation			Y = ~90% Y_{ref} = no data		
BiOBr *BiOBr-BF_4*	1-butyl-3-methylimidazolium bromide and 1-butyl-3-methylimidazolium tetrafluoroborate Br source, surface modification		-	Methyl orange degradation	C_{phot} = 1 g/L C_0 = 10 mg/L V_s = 100 mL t = 270 min		Y = 66.8% k = 0.0023min^{-1} Y_{ref} = no data		
				Tetracycline degradation			Y = ~32% Y_{ref} = no data		
BiOBr *BiOBr-PF_4*	1-butyl-3-methylimidazolium bromide and 1-butyl-3-methylimidazolium hexafluorophosphate Br source, surface modification		-	Methyl orange degradation	C_{phot} = 1 g/L C_0 = 10 mg/L V_s = 100 mL t = 270 min		Y = 23.7% k = 0.0008min^{-1} Y_{ref} = no data		
				Tetracycline degradation			Y = ~27% Y_{ref} = no data		
BiOBr *BiOBr-C16*	1-cetyl-3-methylimidazolium bromide Br source			Methyl orange degradation	C_{phot} = 1 g/L C_0 = 10 mg/L V_s = 100 mL t = 270 min		Y = 69.2% k =0.0039min^{-1} Y_{ref} = no data		
				Tetracycline degradation			Y = ~78% Y_{ref} = no data		
BiOBr *BiOBr-C12*	1-dodecyl-3-methylimidazolium bromide Br source		-	Methyl orange degradation	C_{phot} = 1 g/L C_0 = 10 mg/L V_s = 100 mL t = 270 min		Y = 83.5% k = 0.0047min^{-1} Y_{ref} = no data		
				Tetracycline degradation			Y = ~80% Y_{ref} = no data		
BiOBr *BiOBr-C8*	1-methyl-3-octylimidazolium bromide		-	Methyl orange degradation	C_{phot} = 1 g/L C_0 = 10 mg/L V_s = 100 mL t = 270 min		Y = 85.1%, k = 0.0058min^{-1} Y_{ref} = no data		

	Br source			Tetracycline degradation			Y = ~83% Y_{ref} = no data		
BiOBr/BiOCl *BiOBr/BiOCl*	1-(2-methoxyethyl)-3-methylimidazolium bromide source of Br and morphology directing agent	hydrothermal	flower-like shape assembled by nanosheets S_{BET} = 39.9 m^2/g	Rhodamine B degradation	C_{phot} = 1 g/L C_0 = 10 mg/L V_s = 50 mL t = 50 min	500 W Xe lamp (simulated solar light)	k = 0.0285 min^{-1} k_{ref} = 0.0048 min^{-1} ↗	· high OVs · higher surface area · high separation efficiency of photogenerated carriers	52
BiOCl *Cu/BiOCl (5:1)*	1-methyl-3-octylimidazolium copper trichloride solvent, template, Cl and Cu source	solvothermal	microspheres φ= 3-5 µm S_{BET} = 36.6 m^2/g	Methylene blue degradation	C_{phot} = 0.1 g/L C_0 = 10 mg/L V_s = 100 mL t = 75 min	300 W Xe lamp (400 nm)	Y = 100% Y_{ref} = 44% ↗	· OV formation · evenly distribution of Cu^{2+} · large adsorption capacity · broad light absorption band · low electrons-holes recombination	53
				Bisphenol A degradation	C_{phot} = 0.5 g/L C_0 = 10 mg/L V_s = 100 ml t = 120 min		Y = 96% Y_{ref} = 50% ↗		
$BiVO_4$ *[Bi–Bm][V–Bm]*	1-butyl-3-methylimidazolium tetrachlorobismate Bi source, template, structural agent	mixing and calcination	particles D = 19 nm φ = 1733 nm S_{BET} = 11.66 m^2/g	O_2 evolution	m_{phot} = 25 mg sac. agent0.05 M $Fe(NO_3)_3 \cdot 9H_2O_{aq}$	300 W Xe lamp with an AM 1.5G filter	$Y_{(O2)}$ = 16.6 µmol $Y_{(O2)ref}$ = 10.3 µmol ↗	· OV formation · lower electron-hole recombination	54
$BiVO_4$ *Bi:[V–Bm]*	1-butyl-3-methylimidazolium vanadate V source, template, structural agent		particles D = 18 nm φ = 221 nm S_{BET} = 11.43 m^2/g				$Y_{(O2)}$ = 28.6 µmol $Y_{(O2)ref}$ = 10.3 µmol ↗		
$BiVO_4$ *[Bi–Me]:[V–Me]*	3-(2-methoxyethyl)-1-methylimidazolium tetrachlorobismate		particles D = 19 nm φ = 3236 nm S_{BET} = 11.10 m^2/g				$Y_{(O2)}$ = 3.2 µmol $Y_{(O2)ref}$ = 10.3 µmol ↗		

	Bi source, template, structural agent								
$BiVO_4$ *Bi:[V–Me]*	3-(2-methoxyethyl)-1-methylimidazolium vanadate V source, template, structural agent		particles D = 18 nm φ = 980 nm S_{BET} = 11.79 m^2/g				$Y_{(O2)}$ = 24.2 µmol $Y_{(O2)ref}$ = 10.3 µmol ↗		
BiOI *BiOI-7*	1-ethyl-3-methylimidazolium iodide I source and template	hydrothermal	ultrathin nanosheets φ_p = 19.6 nm th = 3 nm S_{BET} =50 m^2/g	Rhodamine B degradation	C_{phot} = 0.05 g/L C_0 = 10 mg/L V_s = 100 mL t = 40 min	LED lamp, 40 W	Y = 70% k = 0.0287 min^{-1} Y_{ref} = 10% k_{ref} = 0.00248 min^{-1} ↗	· Surface oxygen formation · thinner nanosheets · higher surface area · lower recombination · harvest the light ability · adjustable morphology	55
				Methyl orange degradation	C_{phot} = 0.05 g/L C_0 = 10 mg/L V_s = 100 mL t = 10 min		Y = ~53% Y_{ref} = ~2% ↗		
				Bisphenol A degradation	C_{phot} = 0.05 g/L C_0 = 10 mg/L V_s = 100 mL t =90 min		Y = 86% k = 0.042 min^{-1} Y_{ref} = ~2% ↗		
				H_2 evolution	t = 4 h wit Pt	Xe lamp (>400 nm)	Y_{H2} = 50 µmol Y_{H2ref} = ~15 µmol ↗		
Bi_2SiO_5 *IL-Bi_2SiO_5 3%*	1-butyl-3-methylimidazolium tetrafluoroborate morphology controlling agent	solvothermal	3D flower-like shape assembled by sheets, φ =2-6 nm S_{BET}= 40.8 m^2/g	Rhodamine B degradation	C_{phot} = 2.5 g/L C_0 = 10 mg/L V_s = 50 mL t = 10 min	500 W high-pressure mercury light, UV light	Y = 87% k = 0.20 min^{-1} Y_{ref}=37.4% ↗	· more OVs, · thinner nanosheets, · lower electron-hole recombination	58
$CdWO_4$ *IL-$CdWO_4$*	1-ethyl-3-methylimidazolium dihydrogen phosphate OV defects generation, inhibition of crystal growth	hydrothermal	lump-like particles S_{BET} =62.2 m^2/g	Rhodamine B degradation	C_{phot} = 1 g/L C_0 = 20 mg/L V_S = 50 mL t = 240 min	300 W Xe lamp, (>420 nm)	Y = 84.7% k = 0.2069 h^{-1} Y_{ref} = ~5% ↗	· higher content of OV · higher BET surface area · higher separation efficiency	56
				Tetracycline degradation	C_{phot} = 1 g/L C_0 = 10 mg/L V_S = 50 mL t = 240 min		Y = 61.6% k = 0.1276 h^{-1} Y_{ref} = ~10% ↗		

3) Transfer of photogenerated charges through the composite materials

One of the methods for improving migration process of the photogenerated electrons and holes, is the creation of a heterojunction by connecting two semiconducting materials. The mentioned moieties must be present on the surface of the photocatalyst to efficiently take part in the ongoing reactions by producing reactive species necessary for the photocatalytic process – like for example hydroxyl radicals[59] or superoxide anions[60]. Thus, one of the main factors influencing photocatalytic activity is the efficient transport of photogenerated charge to the surface of the material. If two materials possess compatible locations of conduction and valence bands, such conjugation, as creation of a heterojunction, can lead to a widening of the range of light absorption and reduction of charge recombination probability. In the case of type II heterojunction, the electrons generated after light irradiation are injected into the CB of the p-type semiconductor, to further migrate to the CB of the n-type semiconductor because of internal electric field activity. At the same time, the created holes can migrate from the VB of n-type semiconductor to the VB of p-type semiconductor, which assures their separation from the electrons and prevents recombination. The decreased rate of charge recombination can be confirmed by methods like electrochemical impedance spectroscopy (EIS)[61], surface photovoltage spectroscopy (SPS)[62] or PL[60].

The addition of ILs to the synthesis environment was found to facilitate the creation of heterojunctions, thus to the Fermi level alignment at the interface of the materials, because of the changes in individual energy bands' location. This enables the suitable transfer of charges within the so-connected bands, which cannot be observed when two materials are only mechanically mixed, as the particles are not tightly adhered to each other[63]. Furthermore, the presence of ILs promotes the formation of crystalline phases[64], as well as contributes to the regular dispersity of phases[65–67] and the creation of morphology beneficial for photocatalytic processes (like flake-like[66] shape or nano-flowers aggregated from thin sheets[65]). Among the researched materials, different bismuth oxyhalides (BiOX) and their composites were synthesized by using halide-based ILs as halide precursors. In identical conditions, the replacement of IL with simple salt (e.g., KCl instead of 1-butyl-3-methylimidazolium chloride[64]) did not lead to the obtainment of a composite, but only of BiOX of poor crystallinity instead. The positive polarity of ILs can also facilitate the connection of material characterized by negative polarity with other semiconductors, because of electrostatic attraction[60,68].

The decreased rate of photogenerated charge recombination in studied materials was observed particularly in the assistance of halide-based ILs, of which the anion was playing the role of reagent. The chloride[63,64,68–73], bromide[61,65,72,74–82], and iodide[67,78,83–86] anions of ILs were most often paired with different imidazolium-based cations for example 1-propyl-3-methylimidazolium[78,83], 1-allyl-3-methylimidazolium[73], 1-butyl-3-methylimidazolium[64,67,76,86,87], 1-hexyl-3-methylimidazolium[63,84,85], 1-methyl-3-octylimidazolium[60,61,74], 1- hexadecyl-3-methylimidazolium[65,68,71,72,75,79–82] or 1-methyl-3-[3'-(trimethoxysilyl)propyl]-imidazolium[70]. Among others, ILs possessing cations like N-methyl-2-pyrrolidonium[69], diethylamine[66], tetrabutylammonium[77], tetrachloroferrate[61] or N-butyl-N-methylpiperidinium[61], and anions like dihydrogen phosphate[60], hydrochloride[66] as well as tetrafluoroborate[87], were also utilized. The details of the collected data are presented in Table 3.

Formation of composites in presence of ILs was widely described as a result of their efficient binding and structure-directing abilities. This was further described as the origin of photocatalytic abilities improvement of the as-synthesized materials. Photocurrent measurement [64,65,67,69–72,75–77,79–87], Electrochemical Impedance Spectroscopy (EIS) [60,61,65,67,70–

[73,75–77,79–86], SPS [66,69,78,83], and PL [60,61,63,65,67,70–73,75–77,79–82,84–86] can confirm the decreased rate of charge recombination, and thus the enhanced catalytic efficiency. However, there exist several 'white spots', which should be noted and focused in further research. First concerns limited data regarding confirmation whether the ionic liquid remains at the surface of the photocatalyst, and thus taking part in the light-driven reaction and influencing its mechanism. The presence, or the absence, of ILs on the photocatalyst surface is usually only determined by Fourier-Transform Infrared Spectroscopy (FTIR) [60,63,64,74,79,81,82,84,85]. The second, concerns utilization of halide-based ILs. There is limited information concerning the validity of their use instead of simple halides precursors, especially in terms of bismuth oxyhalides synthesis. Additionally, even though there were various ILs investigated in this field, the vast majority of research is concerning the use of the most popular imidazolium-based ILs. The data regarding other types of ILs is still hardly explored.

Known: ILs are capable of playing the role of reactive structure-directing agents during synthesis of composites

Unknow: exact influence of ILs on photocatalytic reaction mechanism; insufficient investigation over presence of ILs remaining on the surface of the catalyst and its participation in the photocatalytic reaction.

Table 3. *Category: transfer of photogenerated charges through the composite materials.* Preparation conditions, morphology, photocatalytic performance of photocatalysts prepared by ILs-assisted synthesis methods*,**.

Explanation of abbreviations used below in the column:
- *surface properties*: diameter (φ), thickness (th), length (l), width (w), crystallite size (D), specific surface area (S_{BET}), pore volume (V_p), aspect ratio,
- *conditions*: photocatalyst content (C_{phot}), concentration of model pollutant (C_0), volume of solution (V_s), irradiation time (t),
- *efficiency:* efficiency of the most active sample (E_p), efficiency of the refence sample (E_{ref}), ↗ - increase, and ↘ decrease compared to reference sample.

*The table includes all available information.
**The original sample label is given in italics.

Photocatalyst and original sample label	Ionic liquid and its role in the synthesis	Synthesis method	Surface properties	Photocatalytic performance				Mechanism details	Ref.
				Type of model reaction	Conditions	Light source	Yield/reaction rate constant		
Pt/TiO_2 *IL:Pt/TiO₂*	1-butyl-3-methylimidazolium tetrafluoroborate coating and stabilization agent	coating	spherical particles φ = 20-40 nm	H_2 generation	sac. agent triethanolamine C_{phot} = 2 g/L V_s = 600 mL t = 24 h	300 W solar simulator (250−2000 nm, 1 sun, without UV filter)	Y = ~60 μmol·g^{-1}·h^{-1} Y_{ref} = ~21 μmol·g^{-1}·h^{-1}	· lower electron hole recombination	87
Mn-MOF ***1***	1-butyl-3-methylimidazolium bromide charge compensating agent (cations)	solvothermal	rods	CO_2 photoreduction	80 kPa CO_2 m_{phot} = 5 mg C_{phot} = 1.67 g/L V_s = 3 mL t = 240 min	300 W Xe (simulated solar light)	Y_{CH4} = 53 μmol CH_4 h^{-1} g^{-1} Y_{CO} = 21 μmol CO h^{-1} g^{-1} CH_4 selectivity: 71.62	· lower-electron-hole recombination	76
$Bi_2O_3/Bi_2O_2CO_3$ *0.17BBOC*	N-methyl-2-pyrrolidonium chloride C source	solvothermal and in-situ calcination processes	β-Bi_2O_3 nanoparticles are uniformly attached on the $Bi_2O_2CO_3$ nanoplatelets	Rhodamine B degradation	C_{phot} = 1 g/L C_0 = 10 mg/L V_s = 100 mL t = 120 min	300 W Xe lamp, (400 nm)	visible light: Y = 100% Y_{ref} = ~70% ↗ simulated solar-light: Y = ~55% Y_{ref} = 100% ↘	· lower electron-hole recombination · band gap positions	69
Bi_3O_4Br/Bi_2O_3 *0.61BB*	tetrabutylammonium bromide complexing agent and reactant	in situ one-step self-combustion of ionic liquids	Bi_2O_3 spheres uniformly adhered to the surface of Bi_3O_4Br nanosheets, S_{BET} = 4.355 m^2/g V_p = 0.021 cm^3/g Average pore width: 2.544	Methyl orange degradation	C_{phot} = 1 g/L C_0 = 10 mg/L V_s = 100 mL t = 100 min	350 W Xe lamp (400 nm)	Y = 98% k = 0.03703 min^{-1} Y_{ref} = 48% k_{ref} = 0.00716 min^{-1} ↗	· lower electron-hole recombination	77
				Phenol degradation	C_{phot} = 1 g/L C_0 = 10 mg/l V_s = 100 ml		Y = 70% Y_{ref} = ~52% ↗		

					t = 4 h				
$BiOCl/Bi_{24}O_{31}Cl_{10}$ *60%BiOCl*	diethylamine hydrochloride source of cation in IL, reagent/solvent.	self-combustion of ionic liquid	plates (BiOCl) and nanosheets ($Bi_{24}O_{31}Cl_{10}$) S_{BET} = 3.07 m^2/g	Methyl orange degradation	C_{phot} = 1 g/L C_p = 10 mg/L V_s = 100 ml t = 90 min	350 W Xe lamp (400 nm)	k = 0.0135 min^{-1} k_{ref} = 0.0025 min^{-1} ↗	· lower electron-hole recombination	66
				Rhodamine B degradation	C_{phot} = 1 g/L C_p = 10 mg/L V_s = 100 ml t = 40 min		k = 0.0985 min^{-1} k_{ref} = 0.0106 min^{-1} ↗		
				4-chlorophenol degradation	C_{phot} = 1 g/L C_p = 10 mg/L V_s = 100 ml t = 240 min		Y = 88.2% Y_{ref} = no data		
$BiOCl–C_3N_4$ *1BiOCl:1C₃N₄*	1-hexyl-3-methylimidazolium chloride Cl source, template	solvothermal	Dispersed nanoflowers S_{BET} = 24.26 m^2/g	Methyl orange degradation	C_0 = 10 mg L^{-1} C_{phot} = 1 g/L V_S = 200 mL t = 80 min	300 W Xe arc lamp (400 nm)	Y = 94.8% k = 0.0317 min^{-1} $Y_{ref\text{-}BiOCl}$ = 58% $Y_{ref\ C3N4}$ = 11% ↗	· lower electron-hole recombination	63
BiOI/BiOBr *IL-BiOBr*	1-propyl-3-methylimidazolium bromide 1-propyl-3-methylimidazolium iodide additive	solvothermal	thin sheet-like shape, S_{BET} = 11.6 m^2/g V_p = 0.0050 cm^3/g	Rhodamine B degradation	C_{phot} = 1 g/l C_0 = 10 mg/l V_s = 50 ml t = 30 min	500 W Xe lamp	k = 0.084 min^{-1} k_{ref} = 0.0043 min^{-1}	· lower electron-hole recombination · high specific surface area, · high surface hydroxyl content.	78
BiOI/BiOCl *8% BiOI/BiOCl*	1-propyl-3-methylimidazolium iodide solvent and provides I source	hydrothermal	thinner and smaller sheet-like shape with smaller crystallite size th = 2.26 nm	Rhodamine B degradation	C_{phot} = 1 g/L C_0 = 10 mg/L V_s = 50 mL t = 80 min	500 W Xe (simulated sunlight irradiation)	k = 0.023 min^{-1} k_{ref} = 0.004 min^{-1} ↗	· lower electron-hole recombination	83
$Bi_2WO_6/BiOBr$ *50 at% Bi_2WO_6/BiOBr*	1- hexadecyl-3-methylimidazolium bromide solvent, reactant and template	solvothermal	sphere-like BiOBr structures with numerous Bi_2WO_6 nanoparticles cover on the surface φ = 1-2 μm S_{BET} = 59.95 m^2/g	Rhodamine B degradation	C_{phot} = 0.2 g/L C_0 = 20 mg/L V_s = 100 mL t = 150 min	300 W Xe lamp with (400 nm)	Y = 87.9% (after 60 min) Y_{ref} = 48.8% (after 60 min) ↗	· lower electron hole recombination	79
				Bisphenol A degradation	C_{phot} = 0.8 g/L C_0 = 10 mg/L V_s = 50 mL t = 150 min		Y = ~30% Y_{ref} = ~25% ↗		
				Methylene blue degradation	C_{phot} = 0.8 g/L C_0 = 10 mg/L V_s = 50 mL		Y = ~90% Y_{ref} = ~40% ↗		

					t = 150 min				
Bi_2WO_6/BiOBr *W/Br=1:2*	1- hexadecyl-3-methylimidazolium bromide Br source	solvothermal	flower-like structure φ = 200 nm	Rhodamine B degradation	C_{phot} = 0.2 g/L C_p = 10 mg/L V_s = 100 mL t = 90 min	Xe lamp (>420 nm)	Y = 100% Y_{ref} = ~98% ↗	· improved the spatial charge separation, · lower electron-hole recombination	65
				Methylene blue degradation	t = 90 min		Y = 62% Y_{ref} = ~59% ↗		
				Tetracycline degradation	t = 150 min		Y = ~90% Y_{ref} = ~88%		
Bi_2WO_6/BiOCl *S2*	1-butyl-3-methylimidazolium chloride Cl source	an ionic-liquid assisted ultrasonic irradiation at room temperature	diamond microrods coated with nanoparticles l = 5–10 μm φ = 1 μm $φ_{BiOCl}$ = 15-30 nm S_{BET} = 16.88 m^2/g	Rhodamine B degradation	C_0 = 5 mg/L C_{phot} = 1 g/L V_S = 50 mL t = 100 min	300 W Xe lamp (400 nm)	Y = 99% k = 0.0382 min^{-1} $Y_{ref\text{-}Bi2WO6}$ = 47% $Y_{ref\text{-}BiOCl}$ = 98% ↗	· lower-electron-hole recombination	64
				Quinoline blue degradation	C_0 = 5 mg/L C_{phot} = 1 g/L V_S = 50 mL t = 120 min		Y = 97% after k= 0.0217 min^{-1} $Y_{ref\text{-}Bi2WO6}$ = 10% $Y_{ref\text{-}BiOCl}$ = 32% ↗		
				2,4-dinitrophenol degradation	C_0 = 10 mg/L C_{phot} = 1 g/L V_S = 50 mL t = 180 min		After 30 min: Y= 79.08% k = 0.0155 min^{-1} $Y_{ref\text{-}Bi2WO6}$ = 33.25% $Y_{ref\text{-}BiOCl}$ = 56.69% ↗		
BN/BiOBr *0.05 wt% BN/BiOBr*	1- hexadecyl-3-methylimidazolium bromide Br source	solvothermal	hollow desert-rose like microspheres φ = 1-2.6 μm th = 20-30 nm	Rhodamine B degradation	C_0 = 10 mg/L C_{phot} = 0.2 g/L V_S = 100 mL t = 60 min	300 W Xe lamp (400 nm)	Y = ~100% $Y_{ref\text{-}BiOBr}$ = 73.1% ↗	· lower-electron-hole recombination	80
g-C_3N_4/Au/BiOCl *CN/Au/BiOCl-0.48*	1-methyl-3-[3'-(trimethoxysilyl)propyl]-imidazolium chloride template	photoreduction followed by in situ deposition	sandwich structure Au particles φ = 5-10 nm	Rhodamine B degradation	C_{phot} = 0.8 g/L C_0 = 10 mg/L V_s = 50 mL t=60 min	RhB and TC: 500 W Xe lamp (visible light) H_2: 300 W Xe lamp (400 nm)	Y = 97% k = 0.09511 min^{-1} Y_{ref} = 74.3% ↗	· lower electron-hole recombination · improved optical and conductive properties	70
				Tetracycline degradation	C_{phot} = 0.8 g/L C_0 = 10 mg/L V_s = 50 mL t = 120 min		Y = 100% Y_{ref} = 61% ↗		
				H_2 generation	C_{phot} = 0.5 g/L sac. agent 10% MeOH, V_s = 100 mL		Y = ~9.5 μmol Y_{ref} = ~0 μmol ↗		

					t = 3 h				
g-C_3N_4/BiOBr *3 wt% g-C_3N_4/BiOBr*	1- hexadecyl-3-methylimidazolium bromide solvent, reactant, template, and dispersing agent	two steps: polycondensation of dicyandiamide, solvothermal	flower-like microspheres consisted of numerous nanosheets th =~ 10 nm	Rhodamine B degradation	C_{phot} = 1 g/L C_0 = 10 mg/L V_s = 100 mL t = 90 min	300 W Xe lamp (400 nm)	Y = 87% (after 30 min) Y = 100% (after 60 min) Y_{ref} = 39% (after 30 min) Y_{ref} = ~90% (after 60 min) Y_{ref} = ~93% (after 90 min) ↗	· efficient separation and reduced recombination · of electrons and holes;	81
g-C_3N_4/BiOCl *1 % g-C3N4/BiOCl*	1- hexadecyl-3-methylimidazolium chloride dispersing agent, Cl source	solvothermal	spherical structure assembled by nanosheets φ = 1 μm S_{BET} = 22.58 m^2/g	Rhodamine B degradation	C_0 = 10mg/L C_{phot} = 0.1 g/L V_S = 100 mL t = 60 min	solar simulator 300 W Xe lamp (400 nm)	Y = 94% $Y_{ref\text{-}g\text{-}C3N4}$ = 9.1% $Y_{ref\text{-}BiOCl}$ = 50% (after 30 min) ↗	· regular dispersion · lower-electron-hole recombination	68
g-C_3N_4/BiOI *15 wt% g-C_3N_4/BiOI*	1-butyl-3-methylimidazolium iodide solvent, reactant, template and dispersing agent	solvothermal	sphere-like structure φ = 1–2 mm S_{BET} = 73.68 m^2/g	Rhodamine B degradation	C_{phot} = 0.1 g/L C_0 = 10 mg/L Vs = 100 mL t = 50 min	300 W Xe lamp (400 nm)	Y = 100% k = 0.1047 min^{-1} Y_{ref} = 75% k_{ref} = 0.0275 min^{-1} ↗	· lower electron-hole recombination	67
				Methylene blue degradation	C_{phot} = 0.2 g/L C_0 = 10 mg/L V_s = 100 mL t = 80 min		Y = ~95% Y_{ref} = ~80% ↗		
				Methyl orange degradation	C_{phot} = 0.2 g/L C_0 = 10 mg/l V_s = 100 mL t = 120 min		Y = ~92% Y_{ref} = ~80% ↗		
				Bisphenol A degradation	C_{phot} = 0.5 g/L C_0 = 20 mg/l V_s = 100 mL t = 60 min		Y = ~98% Y_{ref} = ~60% ↗		
				4-chlorophenol degradation	C_{phot} = 1 g/L C_0 = 10 mg/L V_s = 100 mL t =180 min		Y = ~20% Y_{ref} = ~6% ↗		
g-C_3N_4/$BiPO_4$ *10 wt% g-C_3N_4/$BiPO_4$*	1-methyl-3-octylimidazolium dihydrogen phosphate solvent, dispersing agent, reactant,	solvothermal	nanoparticles l = ~50 nm	Methylene blue degradation	C_0 = 10 mg/L C_{phot} = 0.3 g/L V_S = 100 mL t = 150 min	250 W high pressure Hg lamp	Y = 89.8% k = 0.0167 min^{-1} $Y_{ref\text{-}BiPO4}$ = 62.0% ↗	· lower-electron-hole recombination	60
				Ciprofloxacin degradation	C_0 = 10 mg/L C_{phot} = 0.3 g/L V_S = 100 mL t = 120 min		Y = 96.6% $Y_{ref\text{-}BiPO4}$ = ~90% ↗		
C_3N_4/$PbBiO_2Cl$	1- hexadecyl-	solvothermal	three-dimensional	Rhodamine B	C_{phot} = 0.3 g/L	300 W Xe lamp	Y = 96%	· lower electron-	71

3 wt% g-C_3N_4/$PbBiO_2Cl$	3-methylimidazolium chloride Cl source, dispersing agent, template		microsphere structure consists ofnumerous NSs th = 15 nm φ = 600 nm S_{BET} = 32.36 m^2/g	degradation	C_0 = 10 mg/L V_s = 100 mL t = 100 min	(400 nm)	k = 0.03078 min^{-1} Y_{ref}=65% k_{ref} = 0.0092 min^{-1} ↗	hole recombination	
				Bisphenol A degradation	C_{phot} = 0.3 g/L C_0 = 10 mg/L V_s = 100 mL t = 210 min		Y = 56% Y_{ref} = 35% ↗		
				Ciprofloxacin degradation	C_{phot} = 0.3 g/L C_0 = 10 mg/L V_s = 100 mL t = 75 min		Y = ~80% Y_{ref} = ~70% ↗		
CQDs/BiOCl/ BiOBr *5 wt% CQDs/BiOCl/ BiOBr*	1- hexadecyl-3-methylimidazolium bromide and 1- hexadecyl-3-methylimidazolium chloride reactant, template, dispersing agent	solvothermal	nanosheets l < 100 nm S_{BET} = 41.28 m^2/g	Rhodamine B degradation	C_0 = 10 mg/L C_{phot} = 0.1 g/L V_S = 100 mL t = 60 min	250 W Xe lamp (400 nm)	Y = ~99% k = 0.0636 min^{-1} Y_{ref} = ~90% ↗	· regular dispersion · lower electron hole recombination	72
				Tetracycline degradation	C_0 = 20 mg/L C_{phot} = 0.3 g/L V_S = 100 mL t = 120 min		Y = 77% k = 0.0135 min^{-1} Y_{ref} = ~40% ↗		
				Ciprofloxacin degradation	C_0 = 10 mg/L C_{phot} = 0.5 g/L V_S = 100 mL t = 240 min		Y = >80% Y_{ref} = ~20% ↗		
				Bisphenol A degradation	C_0 = 10 mg/L C_{phot} = 0.5 g/L V_S = 100 mL t = 240 min		Y = >80% Y_{ref} = ~30% ↗		
CQDs/BiOI *6 wt% CQDs/BiOI*	1-hexyl-3-methylimidazolium iodide I source	solvothermal	microsphere structure φ = 3.5 μm S_{BET} = 29.22 m^2/g	Rhodamine B degradation	C_{phot} = 0.3 g/L C_0 = 10 mg/L V_s = 100 mL t = 120 min	300 W Xe lamp (400 nm)	Y = 94.9% k = 0.0316 min^{-1} Y_{ref} = ~65% k_{ref} = 0.0173 min^{-1} ↗	· lower electron-hole recombination	84
(CQDs)/ $Bi_4O_5I_2$ *1 wt% CQDs/$Bi_4O_5I_2$*	1-hexyl-3-methylimidazolium iodide I source, dispersing agent	solvothermal	CQDs distributed on $Bi_4O_5I_2$ sheet-like structure $th_{Bi4O5I2}$ = 6 nm $φ_{CQDs}$ = 5 nm S_{BET} = 52.60 m^2/g	Rhodamine B degradation	C_0 = 10 m/L C_{phot} = 0.2 g/L V_S = 100 mL t = 120 min	300 W Xe lamp (400 nm)	Y = 94% k = 0.0335 $Y_{ref\text{-}Bi4O5I2}$ = 76% $k_{ref\text{-}Bi4O5I2}$ = 0.0104 min^{-1} ↗	· regular dispersion · lower-electron-hole recombination	85
$FeWO_4$/BiOBr *3 wt% $FeWO_4$/BiOBr*	1-methyl-3-octylimidazolium tetrachloroferrate	solvothermal	BiOBr nanosheets attached to $FeWO_4$	Rhodamine B degradation	C_0 = 10 m/L m_{phot} = 30 mg + 20 μl H_2O_2	300 W Xe lamp (400 nm)	Y = 85% $Y_{ref\text{-}BiOBr}$ = 59.4% ↗	· lower-electron-hole recombination	61

	Fe source, template N-butyl-N-methylpiperidinium bromide Br source, template		microspheres φ = 4 μm		V_S = 100 mL t = 20 min				
				Tetracycline degradation	C_0 = 20 mg/L m_{phot} = 30 mg + 20 μl H_2O_2 V_S = 100 mL t = 20 min		Y = 52.53% $Y_{ref\text{-}FeWO4}$ = ~30% ↗		
In_2O_3/BiOI *In_2O_3/BiOI-2*	1-butyl-3-methylimidazolium iodide I source ,	precipitation	fembronic form of BiOI microspheres with attached In_2O_3 microtubues S_{BET}= 19.2 m^2/g	o-phenylphenol degradation	C_{phot} = 1 g/L C_0 = 30 mg/L V_s = 80 ml t = 200 min	500 W halogen lamp (420 nm)	k = 0.017 min^{-1} k_{ref} = 0.0031 min^{-1} ↗	· rapid interfacial charge transfer, · lower electron-hole recombination · proper band potentials	86
				4-tert-butylphenol degradation	C_{phot} = 1 g/L C_0 = 30 mg/L V_s = 80 mL t = 180 min		k = 0.015 min^{-1} k_{ref} = no data		
MoS_2/BiOBr *3 wt% MoS_2/BiOBr*	1- hexadecyl-3-methylimidazolium bromide reactant, template ad dispersant agent	solvothermal	microspheres	Rhodamnine B degradation	C_{phot} = 0.2 g/L C_0 = 10 mg/L V_s = 100 mL t = 50 min	300 W Xe lamp (UV cutoff filter)	Y = 94% Y_{ref} = 65% ↗	· few-layer structure · lower electron hole recombination	82
NH_2-MIL-125(Ti)/ BiOBr *7 wt%NMT/B*	1-methyl-3-octylimidazolium bromide Br source	solvothermal	irregular NMT nanosheets tightly attached to clustered nanosheets of BiOBr; l_{NMT} = w_{NMT}= 40 – 200 nm S_{BET} = 25.85 m^2/g V_p = 0.103528 cm^3/g	Tetracycline degradation	C_0 = 25 mg/L C_{phot} = 0.2 g/L V_S = 50 mL t = 90 min	400 W Xe lamp (visible light)	Y = 88% $Y_{ref\text{-}NMT}$ = ~50% $Y_{ref\text{-}BiOBr}$ = ~60% ↗	· lower-electron-hole recombination	74
PbS@CuS *PC-5*	1-allyl-3-methylimidazolium chloride morphology agent	hydrothermal	dendritic PbS@CuS core-shell l of PbS dendrites = 5-9.6 μm l of branches = 0.5-3 μm	H_2 generation	C_{phot} = 0.5 g/L sac. agent: NaCl (17.55 g), $Na_2S{\cdot}9H_2O$ (2.4 g), and Na_2SO_3 (0.5 g) V_s=100 mL	300 W Xe	Y = 1736 μmol h^{-1} g^{-1} Y_{ref} = 1288 μmol h^{-1} g^{-1} ↗	· lower electron hole recombination · specific crystal orientation	73

Pd@BiOBr *0.5 wt% Pd/BiOBr*	1- hexadecyl-3-methylimidazolium bromide Br source, dispersing agent	solvothermal	flower-like microsphere structure φ_{BiOBr} = av. 0.8 µm th_{BiOBr} = 10 nm φ_{Pd}= 30 nm	Rhodamine B degradation	C_0 = 10 mg/L C_{phot} = 0.1 g/L V_S = 100 mL t = 50 min	300 W Xe lamp (400 nm)	Y = ~99% k = 0.0902 min^{-1} $Y_{ref\text{-}BiOBr}$ = ~50% ↗	· lower-electron-hole recombination	75

4) Formation of charge-transfer (CT) surface complex

A semiconductor photocatalyst agitated by visible light may be created as a result of interaction between the wide bandgap semiconductor and an organic compound adsorbed on its surface – both of which do not absorb radiation in the visible range. In this occurrence, a charge-transfer (CT) complex between an electron acceptor (semiconductor) and an electron donor (surface adsorbate) may be formed [88]. Surface complexes often consist of a transition metal ion and/or inorganic/organic ligands. Facial of the semiconductor is linked to the adsorbate through various anchors, which can be hydroxyl, carboxyl, amino, and other groups in the case of organic ligands or, for example, CN^-, F^-, PO_4^{3-} in the case of inorganic ligands[89]. Within this mechanism, also called a CT-sensitization or ligand-to-metal charge transfer (LMCT), a direct charge-transfer excitation occurs with no significant involvement of an intermediate excited state (which is common for dye sensitization). In the case of n-type semiconductors (e.g. TiO_2), the localized orbitals of the adsorbate are electronically coupled with empty surface states of the semiconductor. Excitation of the surface complex leads to optical electron transfer from the surface molecule (π electron of the highest occupied molecular orbital, HOMO) to the semiconductor CB ($\pi \rightarrow$ CB) resulting in a decrease in the effective band gap energy of the semiconductor [90,91]. The resulting surface states with HOMO and LUMO characters are mostly located at the adsorbate and belong to the conduction band, respectively.

Since the holes are localized in the organic modifier, and the electrons in the CB of the semiconductor, the hole-electron recombination is prevented, and the lifetime of separated photogenerated charges is extended[90]. Characterization of the surface complex formation is not easy and can be determined by the combination of experimental and theoretical techniques such as UV–visible absorption[92], diffuse reflection (DR)[93], VIS-NIR[94], Attenuated total reflectance-Fourier transform infrared spectroscopy (ATR-FTIR)[95], UV photoemission spectroscopy (UPS), and scanning tunneling microscopy (STM)[96] and quantum chemical calculations[90,97]. In the case of the IL-semiconductor systems, quantum chemical calculations[98] on an anatase vacancy model showed that interactions between halogens (IL anion) and OV are responsible for the excitation of TiO_2 under Vis radiation. The formation of OV on TiO_2, equivalent to the appearance of the Ti^{3+} centers, leads to the formation of unpaired electrons that can form donor levels in the electron structure of TiO_2. The charge transfer between the bromide anion of IL (1-butyl-3-methylimidazolium bromide[4] or 1-butylpyridinium bromide[98]) and molecular oxygen interacting with the vacancy on the TiO_2 surface to form the surface complex ($O_2 \cdots Br^-$ dimer on a TiO_2 vacancy) is a source of is photon-induced photoactivity. Theoretical calculations and experimental research (the apparent quantum efficiency of the photocatalysts) confirmed the presence of a charge transfer complex with a maximum absorption band of about 448 nm for TiO_2 prepared in a presence 1-butyl-3-methylimidazolium bromide. The leading transition (>90%) of 448 nm excitation corresponds to the excitation of an electron from the lone pair in the bromide anion to the π^* orbital localized in the oxygen molecule [98]. FTIR spectra taken for TiO_2 modified by 1-butyl-3-methylimidazolium hydroxide[99] revealed the bands at 1395 cm^{-1} (bending vibrations of $-CH_3$ and $-CH_2-$,), at 2852 and 2920 cm^{-1} (stretching vibrations of aliphatic C–H bonds), which were not present in reference TiO_2. Moreover, comparing the peak areas at 529.9 and 531.8 eV in the O 1 s region obtained from the XPS study, the authors concluded that the decreased number of the surface hydroxyl groups (Ti–OH) is due to the formation of the surface complex between TiO_2 and 1-butyl-3-methylimidazolium hydroxide (Ti–O–C bond formation).

For the semiconductors synthesized in the presence of ionic liquids, the surface complex formation was concluded for the TiO_2 and ZnS photocatalysts with the following ILs: 1-butylpyridinium chloride[98], 1-butyl-3-methylimidazolium hydroxide[99], 1-butyl-3-methylimidazolium nitrate[100], 1-butyl-3-methylimidazolium chloride[2], 1-decyl-3-methylimidazolium chloride[2], 1-methyl-3-octylimidazolium hexafluorophosphate[101], and 1-butyl-3-methylimidazolium bromide[4] as shown in Table 4. Analysis of the electronic structure of ILs revealed that in the case of 1-alkyl-3-methylimidazolium derivatives with halogens as anions, HOMO is localized on the anion whereas in fluorinated ILs HOMO level is associated with the cation or both ions [102–104].

Known: localization of HOMO in ionic liquids

Unknown: geometry of the CT complexes, effect of the IL-derived CT complex on the electronic structure of the semiconductor (new energy levels), energy of charge transfer, correlations between structures of complexes and applicability for photocatalysis, stability of the complexes.

Table 4. *Category: formation of charge transfer (CT) surface complex.* Preparation conditions, morphology, photocatalytic performance of photocatalysts prepared by ILs-assisted synthesis methods*,**.

Explanation of abbreviations used below in the column:
- *surface properties*: diameter (φ), thickness (th), length (l), width (w), crystallite size (D) specific surface area (S_{BET}), pore volume (V_p), pore size (φ_p), aspect ratio,
- *condition:* photocatalyst content (C_{phot}), concentration of model pollutant (C_0), sacrificial agent (sacr. agent), volume of solution (Vs), irradiation time (t),
- *efficiency:* yield (Y)/rate (r)/rate constant (*k*) of the most active sample (Y), and the reference sample (Y_{ref}), ↗ - increase, and ↘ decrease compared to the reference sample.

*The table includes all available information.

**The original sample label is given in italics.

Photocatalyst and the original sample label	Ionic liquid and its role in the synthesis	Synthesis method	Surface properties	Photocatalytic performance				Mechanism details	Ref.
				Type of model reaction	Conditions	Light source	Yield (Y)/ rate (r) /rate constant (*k*)		
TiO_2 *TiO_2_B(1:2)*	1-butyl-3-methylimidazolium bromide additive	solvothemal	porous microparticles φ = 0.5-2.0 mm, S_{BET} = 185 m^2/g	Phenol degradation	C_{phot} = 5 g/L C_0 = 0.21 mM V_s = 25 mL; t = 60 min	1000 W Xe lamp (>420 nm)	Y = 23% r = 1.5 mmol/(dm^3·min^1) Y_{ref} = 1.5% r_{ref} = 0.4 mmol/(dm^3·min^1) ↗	· surface complex between IL anion [Br] and O_2 and TiO_2	4
TiO_2 *TiO_2_[BPy][Br]*	1-butylpyridinium bromide additive	solvothermal	porous microparticles φ = 1.0-3.0 mm	Phenol degradation	C_{phot} = 5 g/L C_0 = 0.21 mM V_s = 25 mL t = 60 min	1000 W Xe lamp (>420 nm)	r = 1.19 mmol/(dm^3·min^1) r_{ref} = 0.22 mmol/(dm^3·min^1) ↗	· surface complex between IL anion [Br] and O_2 anion and TiO2	98
TiO_2 *B3-TiO_2*	1-butyl-3-methylimidazolium hydroxide additive	solvothermal	nanoparticles φ = 10 nm	Methylene blue degradation	C_{phot} = 2 g/L C_0 = 50 ppm V_s = 50 mL t = 180 min	110 W Na (400-800 nm)	Y = ~85% *k* = 0.473 1/h Y_{ref} = ~30% k_{ref} = 0.103 1/h ↗	· surface complex between IL and TiO_2 · electron transfer from LUMO of IL to CB of TiO_2 · lower electron-hole recombination · enhanced adsorption of MB	99
TiO_2 *IL–CD-CNTs/TiO_2*	1-methyl-3-octylimidazolium hexafluorophosphate	solvothermal	carbon nanotubes covered by TiO_2 nanoparticles	Rhodamine B degradation	C_{phot} = 1 g/L C_0 = 20 mg/L V_s = 15 mL	150 W Xe lamp (>420 nm)	Y = 86.7% Y_{ref} = 60% ↗	· surface complex between IL and TiO_2	101

	reaction medium		φ = 20.0-30.0 nm	Methylene blue degradation	t = 180 min		Y = 97.0 % Y_{ref} = 60% ↗	· electron transfer from LUMO of IL to CB of TiO_2 · enhanced adsorption of contaminants	
				Congo red degradation			Y = 88.1% Y_{ref} = 60% ↗		
ZnS *IL-ZnS/GO*	1-butyl-3-methylimidazolium nitrate surface modifier and structure-directing agent	electrostatic adsorption	nanoparticles densely and uniformly decorated on graphene oxide	Rhodamine B degradation	C_{phot} = 0.4 g/L C_0 = 20 mg/L V_s = 20 mL t = 240 min	500 W Xe, (>400 nm)	Y = 80% Y_{ref} = 22% ↗	· surface complex between sulfide nanoparticles and IL cations · strong charge separation (lower electron-hole recombination)	100
Ag_2S *IL-Ag_2S/GO*							Y = 42% Y_{ref} = 22% ↗		
CdS *IL-CdS /GO*							Y = 86% Y_{ref} = 22% ↗		

5) Exposing crystallographic planes

The exposition of specific crystallographic facets or the presence of different phases of one compound (thus the presence of specific facets) can significantly influence the photocatalytic abilities of different crystalline materials. High exposure to specific planes may be beneficial for the increased pollution particles' adsorption capacity. This is due to the presence of a high amount of under-coordinated sites, that are characterized by greater reactivity in comparison with other planes[105], as the molecules in photocatalysis-favorable states can be easily accessed by the particles of contaminants[106]. What is more, the presence of two specific facets can significantly suppress the recombination of photogenerated electron-hole pairs[107]. The reactions of reduction and oxidation can occur on different planes because of their different band structure, as well as the varying positions of the edges of the bands. This leads to the separation of the electrons and holes which are transported to distinct planes[105,108]. The formation of particular facets and their content can be determined by using methods like transmission electron microscopy (TEM) coupled with selected area electron diffraction (SAED)[109] or XRD[110].

The most beneficial form of the growing crystal is one of the possibly lowest surface energies. However, the facets providing reactive centers are characterized by higher surface energy, which makes them unstable. The ILs' ability of weak interaction creation (like hydrogen bonding) can be a useful tool to influence the nucleation and further growth of crystalline solids, because of modified surface energy. This is an effect of the high polarity of ILs, thus low interface tension[111]. Such properties are vital to affecting the growth rate of different planes, as well as the order and arrangement of the unit cell connection. It is possible because of the presence of the weakly-bonded ILs particles present at specific surfaces[112] or edges[110].

Imidazolium-based ILs were mainly utilized to obtain specified crystalline products. Among them ILs like 3-methyl-1-(3-sulfonylpropyl) imidazolium trifluoromethanesulfonate[113], 1-(3-hydroxypropyl)-3-methylimidazolium bis(trifluoromethylsulfonyl)imide[114], 1-butyl-3-methylimidazolium bis(trifluoromethylsulfonyl)imide[114], 1-hexadecyl-3-methylimidazolium bromide[112], 1-hexadecyl-3-methylimidazolium chloride[112], 1-ethyl-3-methylimidazolium tetrafluoroborate[115], 1-butyl-3-methylimidazolium bromide[109], and 1-butyl-3-methylimidazolium tetrafluoroborate[110] can be distinguished. Additionally, papers describing the use of ILs possessing other types of cations like 1-butylpyridinium bis(trifluoromethylsulfonyl)imide[114], 2-hydroxylethylammonium formate[116] or tetradecyltrihexyl phosphonium bis(trifluoromethylsulfonyl)imide[114] were also presented. All the listed ILs are shown in Table 5.

High exposure of specific planes may be beneficial for the increased pollution particles adsorption capacity. In case of bismuth oxyhalides, exposition of {001} facets, resulting in sheet-like structures, can be achieved by introduction of halide-based ILs as the halide source[109,112]. At the same time, the cations of the ILs interact with the oxygen atoms of forming structure net by creation of hydrogen bonding. This process leads to decrease of surface energy of the mentioned facet hindering its growth. Additionally, the manipulation with specific planes growth was connected with improvement of electron-holes separation, when the (002) and (222) facets of NH_2-MIL-125(Ti) were exposed in the fabricated composite[115]. In turn, in case of $SrTiO_3$ it was established that the functionalization of side chain of imidazolate IL can affect the growth in different directions, thus influence the photocatalytic efficiency[114].

As the literature shows, the influence of ILs on forming structure, and thus on the facets being exposed, as well as on the presence of different phases, can be easily confirmed by abovementioned methods[109,110]. The structure-directing abilities of ILs can be verified, by comparison of the material with the reference sample obtained when no IL is added to the reaction environment. However, the information regarding the presence of IL residues on the surface of the catalyst is not always provided. This can raise a question about the participation of IL (or its decomposition products) in photocatalytic process and how does it affect the mechanism of the reaction.

Known: ILs are capable of playing the role of reactive structure-directing agents, and thus affect the electron-hole separation

Unknown: exact influence of ILs on photocatalytic reaction mechanism; insufficient investigation over presence of ILs remaining on the surface of the catalyst and its participation in the photocatalytic reaction

Table 5. *Category: exposing crystallographic planes.* Preparation conditions, morphology, photocatalytic performance of photocatalysts prepared by ILs-assisted synthesis methods*,**.

Explanation of abbreviations used below in the column:
- *surface properties*: diameter (φ), thickness (th), length (l), width (w), crystallite size (D) specific surface area (S_{BET}), pore volume (V_p), pore size (φ_p), aspect ratio,
- *conditions*: photocatalyst content (C_{phot}), the concentration of model pollutant (C_0), sacrificial agent (sacr. agent), volume of solution (Vs), irradiation time (t),
- *efficiency:* yield (Y)/rate (r)/rate constant (*k*) of the most active sample (Y), and the reference sample (Y_{ref}), ↗ - increase, and ↘ decrease compared to the reference sample.

*The table includes all available information.
**The original sample label is given in italics.

Photocatalyst and original sample label	Ionic liquid and its role in the synthesis	Synthesis method	Surface properties	Photocatalytic performance				Mechanism details	Ref.
				Type of model reaction	Conditions	Light source	Yield/reaction rate constant		
TiO_2 *S8*	1-butyl-3-methylimidazolium tetrafluoroborate additive	solvothermal	nanoparticles φ = 8 ± 2 nm S_{BET} = 198.7 m^2/g V_p = 0.35 cm^3/g	p-chlorophenol degradation	m = 50 g C_{phot} = 0.47 mM t = 120 min	250 W Hg lamp	Y = 96.3% Y_{ref} = ~87% ↗	· anatase structure (brookite in ref sample)	110
TiO_2 *S2*	3-methyl-1-(3-sulfonylpropyl)-imidazolium trifluoromethane-sulfonate template, structure directing agent, hydrolyzing agent	sol–gel	bunch of aligned thin flaky nano-rods φ = 3–5 nm S_{BET} = 99.3 m^2/g	Methyl orange degradation	C_{phot} = 0.3 g/L C_0 = 20 ppm V_s= 200 mL t = 120 min	125 W lamp (UV)	Y = 100% Y_{ref} = no data	· higher rutile content	113
TiO_2 *S6*		hydrothermal	nanorods l = 120–170 nm w = 20–24 nm S_{BET} = 48.2 m^2/g		C_{phot} = 0.3 g/L C_0 = 20 ppm V_s= 200 mL t = 240 min		Y = 99% Y_{ref} = no data	· higher rutile content	
RTIL/TiO_2	2-hydroxylethyl-ammonium formate additive	sol–gel	nanoparticles φ = 85 nm	Acetic blue 92 degradation	C_{phot} = 0.1 g/L C_0 = 10 ppm V_s = 100 mL t = 120 min	125 W Hg lamp (UV)	Y = ~70% Y_{ref} = ~57% ↗	· anatase structure (rutile in ref sample)	116
BiOBr *IL-BiOBr*	1-butyl-3-methylimidazolium bromide solvent, reactant and the directing agent	hydrothermal	square nanoplates w = 120–270 nm th = 20–35 nm	Rhodamine B degradation	C_{phot} = 0.5 g/L C_0 = 10 mg/l V_s = 100 mL t = 90 min	300 W Xe lamp (420 nm)	Y = 100% Y_{ref} = 65.7% ↗	· high-ratio exposure of {001} facets	109

$SrTiO_3$ *S1*	1-(3-hydroxypropyl)-3-methylimidazolium bis(trifluoromethyl-sulfonyl)imide solvent, reactant, and morphology directing agent	sonochemical	spherical NPs D~ 20 nm S_{BET} = 50.13 m^2/g V_p = 0.07 cm^3/g	Methylene blue degradation	C_{phot} = 1 g/L C_0 = 10 ppm V_s = 100 mL t = 90 min	290 W Xe arc lamp (>320 nm)	Y = 88% k = 0.0121 min^{-1} k_{ref}=0.014 min^{-1} ↘	· different specific facets	114
				H_2 generation	C_0 = 0.83 g/L sac. agent 10% MeOH V_s = 600 mL 0.025 wt% Rh	700 W Hg lamp	Y = 255.5 µmol/h (with 0.025%Rh ~930 µmol/h) Y_{ref} = 951 µmol/h ↘ (↘)		
$SrTiO_3$ *S2*	1-butyl-3-methylimidazolium bis(trifluoromethyl-sulfonyl)imide solvent, reactant, and morphology directing agent		nanospheres compose of cubic-like aggregates with an overall edge l = 100-300 nm D = 14 nm S_{BET} = 47.08 m^2/g V_p = 0.07 cm^3/g	Methylene blue degradation	C_{phot} = 1 g/L C_0 = 10 ppm V_s = 100 mL t = 90 min	290 W Xe arc lamp (>320 nm)	Y = 41% k = 0.003 min^{-1} k_{ref} = 0.014 min^{-1} ↘		
				H_2 generation	C_0 = 0.83 g/L sac. agent 10% MeOH V_s = 600 mL 0.025 wt% Rh	700 W Hg lamp	Y = 224.4 µmol/h (with 0.025%Rh 1115.4 µmol/h) Y_{ref} = 951 µmol/h ↘ (↗)		
$SrTiO_3$ *S3*	1-butylpyridinium bis(trifluoromethyl-sulfonyl)imide solvent, reactant and morphology directing agent		raspberry-like nanospheres D = 20 nm S_{BET} = 62.28 m^2/g V_p = 0.09 cm^3/g	Methylene blue degradation	C_{phot} = 1 g/L C_0 = 10 ppm V_s = 100 mL t = 90 min	290 W Xe arc lamp (>320 nm)	k = 0.0016 min^{-1} k_{ref} = 0.014 min^{-1} ↘		
				H_2 generation	C_0 = 0.83 g/L sac. agent 10% MeOH V_s = 600 mL 0.025 wt% Rh	700 W Hg lamp	Y = 136.5 µmol/h (with 0.025%Rh ~880 µmol/h) Y_{ref} =951 µmol/h ↘ (↘)		
$SrTiO_3$ *S4*	tetradecyltrihexyl-phosponium bis(trifluoromethyl-sulfonyl)imide solvent, reactant and morphology directing agent		ball-like nanospheres D = 19 nm S_{BET} = 52.79 m^2/g V_p = 0.08 cm^3/g	Methylene blueB degradation	C_{phot} = 1 g/L C_0 = 10 ppm V_s = 100 mL T = 90 min	290 W Xe arc lamp (>320 nm)	k = 0.005 min^{-1} k_{ref} = 0.014 min^{-1} ↘		
				H_2 generation	C_0 = 0.83 g/L sac. agent 10% MeOH V_s = 600 mL 0.025 wt% Rh	700 W Hg lamp	Y = 0 µmol/h (with 0.025%Rh ~80 µmol/h) Y_{ref} = 951 µmol/h ↘ (↘)		

(CQDs)/BiOBr *3wt% CQDs/BiOBr*	1- hexadecyl-3-methylimidazolium bromide solvent, dispersing agent, soft template, reactant	solvothermal	square nanosheets th = 25 nm l = 150 nm	Rhodamine B degradation	C_0 = 0.01 g/L m_{phot} = 20 mg V_S = 100 mL t = 50 min	300 W Xe lamp (400 nm)	Y = ~100%; k = 0.1058 min^{-1} Y_{ref} = 60% ↗	· inhibition of (001) facets growth – preferential growth · lower electron-hole recombination	112
				Ciprofloxacin degradation	C_0 = 0.01 g/L m_{phot} = 30 mg V_S = 100 mL t = 240 min		Y = ~70% Y_{ref} = ~35% ↗		
				Bisphenol A degradation	C_0 = 0.01 g/L m_{phot} = 50 mg V_S = 100 mL t = 180 min		Y = ~55% Y_{ref} = ~35% ↗		
(CQDs)/BiOCl *3 wt% CQDs/BiOCl*	1- hexadecyl-3-methylimidazolium chloride solvent, dispersing agent, soft template, reactant		square nanosheets th = 50 nm l = 300 nm	Rhodamine B degradation	C_0 = 0.01 g/L m_{phot} = 20 mg V_S = 100 mL t = 50 min		Y = ~75% Y_{ref} = ~40% ↗		
				Ciprofloxacin degradation	C_0 = 0.01 g/L m_{phot} = 30 mg V_S = 100 mL t = 240 min		Y = ~20% Y_{ref} = 0% ↗		
IL-PANI/NH_2-MIL-125 *IL-PANI/NMIL(Ti)*	1-ethyl-3-methylimidazolium tetrafluoroborate modulator of facets growth speed	solvothermal	spiked sea-urchin like crystals φ = 30-50 nm S_{BET} = 1125 m^2/g V_p = 0.43 cm^3/g	Acetaldehyde degradation	C_0 = ~300 ppm C_{phot} = 0.04 g/L V_S = 1000 mL t = 15 min	350 W Xe (200–800 nm)	Y = 92% k = 0.262 min^{-1} Y_{ref} = 50% ↗	· specific facets exposed: (002) and (222) · lower electron-hole recombination	115

6) Development of the surface

Improvement of the photocatalytic properties can be also realized through the development of the semiconductor surface. Higher specific surface area results in a larger number of reactive sites where photocatalytic reactions can occur. The increased specific surface area allows for more adsorption sites, enabling better adsorption of reactant molecules onto the photocatalyst's surface[117]. Higher surface area also improves the semiconductor's light-harvesting properties[118]. A larger surface area is available for light absorption, leading to increased utilization of incident photons and improved photoactivity. The increased surface area provides more pathways for charge carriers (such as electrons and holes) to migrate and participate in photocatalytic reactions. A more developed and oriented material's surface enables efficient charge transfer, reducing recombination and prolonging the lifetime of charge carriers[119].

As shown in Table 6 by altering the IL composition it is possible to achieve semiconductors with high/higher specific surface areas, porosity, lower particle size, and specific morphologies. This has been achieved for various semiconductor materials such as TiO_2[120], ZnO[121], BiOI[122], BiOBr[123], BiOCl[124], Bi_2SiO_5[125], $BiPO_4$[126], $SrSnO_3$[127], SnS_2,[128] or composites such as TiO_2/CuO[129], Y_2O_3/TiO_2[130], Bi_2WO_6-Bi_2O_3[131], In_2S_3/TiO_2[132], MoS_2/Bi_5O_7I[133], BiOBr/BiOCl[134], BiOCl/m-$BiVO_4$[135], rGO_Bi_2WO_6[136], NH_2-UiO-66/BiOBr[137], ZrO_2@ HKUST-1[138], Cu_2S–MoS_2[139], Ag_3PO_4/$BiPO_4$[140]. These materials were synthesized using various methods, including hydrothermal, solvothermal, microwave technique, microwave-assisted solvothermal synthesis, ultrasonic processing, and the sol-gel method. Among various ionic liquids, ethylammonium nitrate[6141], 1-(2-methoxyethyl)-3-methylimidazolium methanesulfonate[129,130], 1-(triethoxysilylpropyl)-3-methylimidazolium chloride[142], $[CH_2CH_2]O_2(mm)_2$[121], tetramethylammonium glycine[143], glutamic acid tetrafluoroborate[144], 1-ethyl-3-methylimidazolium ethyl sulfate[145], 1-methyl-3-[3'-(trimethoxysilyl)propyl]-imidazolium[146], 1-butyl-3-methylimidazolium bis(trifluoromethylsulfonyl)imide[127,147], 1-methyl-3-octylimidazolium bis(trifluoromethylsulfonyl)imide[147], 1-decyl-3-methylimidazolium bis(trifluoromethylsulfonyl)imide[147], 1-ethyl-2,3-dimethylimidazolium bis(trifluoromethylsulfonyl)imide[147], trimethylbutylammonium bis(trifluoromethylsulfonyl)imide[147], 1-butyl-3-methylimidazolium thiocyanate[139,147], 1-butyl-2,3-dimethylimidazolium tetrafluoroborate[148], 1-ethyl-3-methylimidazolium tetrafluoroborate[148], 1-butyl-3-methylimidazolium hydroxide[149], 1-dodecyl-3-methylimidazolium hydroxide[149], (2-hydroxyethyl)-trimethylammonium hydroxide[149], 1-ethyl-3-methylimidazolium hexafluorophosphate[150], 1-butyl-3-vinylimidazolium bromide[123], poly-1-butyl-3-vinylimidazolium bromide[123], poly-1-butyl-3-vinylimidazolium bromide acrylamide[123], 1-hexadecyl-3-methylimidazolium bromide[151,152], choline chloride[124], chlorinated pyridine[124], imidazole chloride[124], 1-methyl-3-octylimidazolium dihydrogen phosphate[126], 1,6-bis(3-methylimidazolium-1-yl)hexane bis(trifluoromethylsulfonyl)imide[127], tetradecyltrihexylphosponium bis(trifluoromethylsulfonyl)imide[127], 1-butylpyridinium bis(trifluoromethylsulfonyl)imide[127], 1-hexyl-3-methylimidazolium chloride[128], 1-butyl-3-methylimidazolium acetate[128], 1-allyl-3-methylimidazolium chloride[131], 1-allyl-3-methylimidazolium bromide[134], N,N,N,N',N',N'-hexakis(2-hydroxyethyl)ethane-1,2-diaminium bromide[138], 2-hydroxylethylammonium formate[140], 1-hexadecyl-3-methylimidazolium chloride[153], 1-hexadecyl-3-methylimidazolium bromide[137,153,154], 1-ethyl-3-methylimidazolium iodide[133], 1-butyl-3-methylimidazolium iodide[122,155], 1-butyl-3-methylimidazolium bromide[2,128,156], 1-butyl-3-methylimidazolium chloride[2,128,131,132,135,157], 1-butyl-

2,3-dimethylimidazolium chloride[132], 1-butylpyridinium bromide[158], 1-methyl-3-octylimidazolium tetrafluoroborate[3], and 1-butyl-3-methylimidazolium tetrafluoroborate[58,110,120,125,128,136,148,159] have been widely employed in the semiconductors' synthesis, as shown in Table 6. The aforementioned ILs were added during the synthesis process, serving multiple roles including solvent[122], surface/morphology directing agent[125,127], reactant[123], template[160], source of phosphate[126], iodine[133], fluorine[159] and chlorine [124], as well as functioning as an additive[2] and stabilizer[160].

As summarized in Table 6, the enhanced photocatalytic activity was attributed to several factors: reduced particle size, increased BET surface area, decreased particle aggregation, and the formation of uniform morphologies such as spheres. Additionally, better porous microsphere structure, larger pore volume and size played a significant role. Beyond these factors, the most commonly observed phenomena contributing to increased photocatalytic activity included lower electron-hole recombination, suitable energy band structure, narrower band gap structure, presence of oxygen vacancies, and degree of crystallinity. Paszkiewicz et al.[2] reported that the inclusion of 1-butyl-3-methylimidazolium chloride and 1-decyl-3-methylimidazolium chloride in the solvothermal synthesis of TiO_2 led to improved photoactivity. This enhancement was due to a reduction in particle size, an increase in surface area, and a more regular shape of microspheres compared to the unmodified sample. On the other hand, by altering the types of ILs in terms of both anions and cations, ZnO materials with varying morphologies could be synthesized, specifically nanospheres of different diameters and nanorods with varying lengths and diameters[160]. The morphology of the nanospheres was crucially influenced by the use of 1-methyl-3-octylimidazolium bis(trifluoromethylsulfonyl)imide or 1-decyl-3-methylimidazolium bis(trifluoromethylsulfonyl)imide, while nanorods were obtained using 1-butyl-3-methylimidazolium bis(trifluoromethylsulfonyl)imide, 1-ethyl-2,3-dimethylimidazolium bis(trifluoromethylsulfonyl)imide, trimethylbutylammonium bis(trifluoromethylsulfonyl)imide, and 1-butyl-3-methylimidazolium thiocyanate[160].

Development of the surface can be measured by gas adsorption techniques, atomic force microscopy (AFM), scanning electron microscopy (SEM), and TEM mercury porosimeter[124,137,140,156,161,162]. Alammar and Mudring[160] synthesized ZnO using five different ILs exhibiting various morphology including nanorods, nanospheres, prismatic, flower-like, and nanosheets and morphological parameters such as shape, diameter, and length were possible to determine based on SEM and TEM imaging. Based on nitrogen adsorption–desorption isotherm measurements it was possible to determine BET surface areas of the prepared samples. It was found that the highest surface area reaching the value of 55 m^2/g was achieved by synthesizing ZnO nanospheres with a diameter of 100 nm using IL 1-decyl-3-methylimidazolium bis(trifluoromethylsulfonyl)imide[160] .

As shown in Table 6, the enhancement of photocatalytic properties via the application of ionic liquids to the development of the semiconductor's surface has been the subject of extensive and intensive research in recent years. While the existing research has shed light on the benefits of using ionic liquids in enhancing photocatalytic activity, there remains a critical need for a deeper and more precise understanding of the key factors driving this enhancement. The current hypotheses, which suggest improvements due to unique morphology, reduced particle size, or minimized aggregation, lack clear and consistent support. It is essential to establish more concrete evidence to validate these theories and to identify the principal

mechanisms responsible for the observed enhancements in photocatalytic activity. Although the majority of photoactivity studies have predominantly focused on the degradation of pollutants, it is recommended to broaden the scope of research to encompass other significant reactions. These include hydrogen photogeneration, CO_2 photoreduction, and the transformation of organic compounds. There is currently a lack of clarity regarding the presence of ionic liquids or their residues on semiconductor surfaces and how this might impact subsequent processes, such as photocatalytic reactions.

Known: effect of a wide range of ILs on semiconductor morphology, increased activity in photodegradation of pollutants, ILs decomposition during synthesis of semiconductors, growth mechanisms.

Unknown: what role do the remaining ionic liquids or their residues present on the semiconductor play? which parameter plays a key role in enhanced oh photoactivity, and other photocatalytic applications such as CO_2 photoconversion.

Table 6. *Category: development of the surface.* Preparation conditions, morphology, photocatalytic performance of photocatalysts prepared by ILs-assisted synthesis methods*,**.

Explanation of abbreviations used below in the column:
- *surface properties*: diameter (φ), thickness (th), length (l), width (w), crystallite size (D) specific surface area (S_{BET}), pore volume (V_p), pore size (φ_p), aspect ratio,
- *conditions*: photocatalyst content (C_{phot}), the concentration of model pollutant (C_0), sacrificial agent (sacr. agent), volume of solution (Vs), irradiation time (t),
- *efficiency:* yield (Y)/rate (r)/rate constant (*k*) of the most active sample (Y), and the reference sample (Y_{ref}), ↗ - increase, and ↘ decrease compared to the reference sample.

*The table includes all available information.
**The original sample label is given in italics.

Photocatalyst and original sample label	Ionic liquid and its role in the synthesis	Synthesis method	Surface properties	Photocatalytic performance				Mechanism details	Ref.
				Type of model reaction	Conditions	Light source	Yield (Y)/rate (r)/rate constant (*k*)		
TiO_2 *TiO₂_B(1:2)*	1-butyl-3-methylimidazolium chloride additive	solvothermal	microparticles φ = 0.5-4.0 mm S_{BET} = 202 m^2/g	Phenol degradation	C_{phot} = 0.5 g/L C_0 = 0.43 mM t = 80 min	150 W Hg lamp (UV-Vis)	r = 5.9 mmol·dm^{-3}·min^{-1} r_{ref} = 5.2 mmol·dm^{-3}·min^{-1} ↗	· lower particle size, · higher BET surface area · more regular shape · more regular dispersion	2
TiO_2 *TiO₂_D(1:2)*	1-decyl-3-methylimidazolium chloride additive	solvothermal	microparticles φ = 0.5-4.0 mm S_{BET} = 218 m^2/g	Phenol degradation	C_{phot} = 0.5 g/L C_0 = 0.43 mM t = 80 min	150 W Hg lamp (UV-Vis)	r = 5.5 mmol·dm^{-3}·min^{-1}) r_{ref} = 5.2 mmol·dm^{-3}·min^{-1} ↗		
TiO_2 *TB9*	1-butyl-3-methylimidazolium tetrafluoroborate additive	sol–gel	wormhole-like particles S_{BET} = 102 m^2/g	Methylene blue degradation	C_{phot} = 1 g/L C_0 = 50 mg/dm^3 t = 3 h	100 W UV lamp 365 nm	Y= ~90% Y_{ref} = ~90% →	· higher BET surface area than non-porous P25	120
TiO_2 *S8*	1-butyl-3-methylimidazolium tetrafluoroborate additive	solvothermal	nanoparticles φ = 8 ± 2 nm S_{BET} = 198.7 m^2/g	p-chlorophenol degradation	C_{phot} = 1 g/L C_0 = 0.47 mM t = 120 min	250 W Hg lamp (UV-Vis)	Y = 96.3% Y_{ref} = ~87% ↗	· higher BET surface area	110
TiO_2 *NTs-[OMIM]_90V*	1-methyl-3-octylimidazolium tetrafluoroborate F source	anodic oxidation of Ti foil	nanotubes l = 0.85 mm φ = 120 nm	Phenol degradation	4 cm^2 of TiO_2 NTs C_0 = 0.21 mM V_s = 10 mL t = 60 min	1000 W Xe lamp (>420 nm)	r = 1.82 mmol $dm^{-3}min^{-1}$	· NT length	3
						1000 W Xe lamp (>420 nm)	r = 0.63 mmol $dm^{-3}min^{-1}$		

TiO_2 *NTs*	1-butyl-3-methylimidazolium tetrafluoroborate F source	anodic oxidation of Ti sheets	nanotubes l = 1 mm φ = 280 nm	Methyl orange degradation	1.23 cm^2 of TiO_2 NTs C_0 = 10 ppm V_s = 35 mL t = 150 min	150 W Hg-Xe lamp	Y = ~86% Y_{ref} = no data	NT length	159
TiO_2 *TiO_2 NTs_0.05*	ethylammonium nitrate additive	anodic oxidation of Ti foil	nanotubes l = 6.0 μm φ = 107 nm, wall th = 5.4 nm.	Phenol degradation	4 cm^2 of TiO_2 NTs C_0 = 20 mg/L V_s = 8 mL t = 60 min	1000 W Xe lamp (>350 nm)	k = 0.0941 min^{-1} r = 9.12 μmol min^{-1} dm^{-3} k_{ref} = 0.0712 min^{-1} r_{ref} = 5.53 μmol min^{-1} dm^{-3} ↗	· longer NT · developed surface area	6
TiO_2/CuO TiO_2/CuO NCs (ILAHM)	1-(2-methoxyethyl)-3-methylimidazolium methanesulfonate additive	hydrothermal	irregular particles S_{BET} = 45.6 m^2/g	H_2 generation	C_{phot} = 1 g/L sacr. agent= 2.5 mL EtOH V_s = 7.5 mL t = 280 min	300 W Xe/Hg lamp	Y = 8670 mmol/g Yr_{ef} = ~1300 mmol/g ↗	· higher BET surface area	129
TiO_2 *F-TiO_2-IL[HT]-500*	1-(triethoxysilylpropyl)-3-methylimidazoliumchloride additive	hydrothermal	nanoparticles S_{BET} = 198 m^2/g	Methylene blue degradation	C_{phot} = 0.5 g/L C_0 = 0.04 mM Vs= 50 ml t = 60 min	36 W 370 nm	Y = 98% Y_{ref} = ~91% ↗	· higher BET surface area	142
Y_2O_3/TiO_2 *25 wt%Y_2O_3/TiO_2 NC(ILAHM)*	1-(2-methoxyethyl)-3-methylimidazolium methanesulfonate solvent, surface directing agent	hydrothermal	voluminous porous network with voids Φ = 55 nm S_{BET} = 50.6 m^2/g	H_2 generation	C_{phot} = 1 g/L V_s = 7.5 ml sacr. agent = 2.5 mL EtOH t = 150 min	300 W Xe/Hg lamp	Y = 1380 mmol/g Y_{ref} = ~550 mmol/g ↗	· higher BET surface area · less aggregated particles	130
ZnO *Hexagonal mesoporous plates of ZnO*	{[CH_2CH_2] O_2 $(mm)_2$} templating agent, source of hydroxyl radical	hydrothermal	hexagonal mesoporous plates th= 2 μm l= 2 μm φ= 2 μm S_{BET} = 84 m^2/g	NOx degradation	C_{phot} = 0.15 g/L C_0 = 10 ppm V_s = 0.68 L t = 40 min	2.4 W Philips, λ=200–280 nm	Y =56% Y_{ref}~30% ↗	· higher BET surface area · enhance the adsorption ability · higher separation efficiency of photogenerated e^- and h^+	121
				SO_2 degradation	C_{phot} = 1 g/L C_0 = 2000 ppb V_s = 0.68 L t = 40 min		Y = 81% Y_{ref}~30% ↗		
				CO degradation	C_{phot} = 1 g/L C_0 = 25 ppm V_s = 0.68 L t = 40 min		Y >35% Y_{ref}~21% ↗		

ZnO *MZ-3-8*	tetramethylammonium glycine morphology controlling agent	solvothermal	nanosheets S_{BET}= 4.82 m^2/g	Congo red degradation	C_{phot} = 0.5 g/L C_0 = 50 mg/L V_s = 100 mL t = 200 min	simulated solar light (300 W)	Y = 100% Y_{ref}~30% ↗	· higher BET surface area · the smaller particle size · more electron holes are generated with the increased absorption area	143
ZnO *Water+RTIL*	1-ethyl-3-methylimidazolium ethyl sulfate reaction media	Ultrasonic assisted synthesis	small sized nanocrystalline	Methyl orange degradation	C_{phot} = 0.4 g/L $C_0 = 4.9 \cdot 10^{-5}$ M V_s = 250 mL t = 180 min	125 W UV Osram lamp	Y = 100% Y_{ref}=60% ↗	· small size · lower recombination of electron hole pairs	145
ZnO *ZnO pompons*	glutamic acid tetrafluoroborate reaction medium	microwave heating	nano/micro pompons φ =1.6-3.0 μm S_{BET} =28.3 m^2/g	Methyl orange degradation	C_{phot} = 0.3 g/L C_0 = 10 mg/L V_s = 100 mL t = 420 min	direct sunlight	Y = 74.3% ↗	· uniform morphology and size	144
				Methyl violet degradation	C_{phot} = 0.3 g/L C_0 = 10 mg/L V_s = 100 mL t = 420 min		Y = 96.9% Y_{ref} = ~10% ↗		

ZnO *ZnO*	1-butyl-3-methylimidazolium chloride agglomeration inhibitor	microwave	nanoparticles φ = 15-25 nm D = 18 nm S_{BET} = 30 m^2/g V_p = 0.37 cm^3/g	Malachite green degradation	C_{phot} = 0.1-1 g/L C_0 = 1-3·10^{-5} g/L t = 40 min	125 W Hg vapor lamp	Y = 100% Y_{ref} = no data	· lower agglomeration of nanoparticles	157
ZnO *D*	ethylammonium nitrate morphology agent	hydrothermal	spherical φ_p = 77.64 Å S_{BET}= 7.11 m^2/g	Methylene blue degradation	C_{phot} = 0.02 g/L C_0 = 20 μM V_s = 100 mL t = 55 min	60W mercury lamp	k = ~ 0.035 min^{1} k_{ref} = ~ 0.022 min^{1} ↗	· higher specific surface area · higher average pore size	141
ZnO *ZnO-1.6A*	1-methyl-3-[3'-(trimethoxysilyl)propyl]-imidazolium chloride template	hydrothermal	individual microrods with self-assembled bowknot-like architecture S_{BET}= 14 m^2/g V_p =0.057 cm^3/g φ_p = 16.4 nm	Methylene blue degradation	C_{phot} = 0.3 g/L C_0 = 10 mg/L V_s = 100 mL t = 180 min	UV light irradia-tion (250 W, GY-250, λ = 365 nm)	Y = ~90% Y_{ref} = no data	· high surface area · high adsorption capability of dye, · the separation rate of photogenerated electron–hole pairs	146
				Methyl orange degradation	C_{phot} = 0.3 g/L C_0 = 10 mg/L V_s = 100 mL t = 180 min		Y = ~15% Y_{ref} = no data		
				Rhodamine B degradation	C_{phot} = 0.3 g/L C_0 = 10 mg/L V_s = 100 mL t = 180 min		Y = ~70% Y_{ref} = no data		
ZnO *1*	1-butyl-3-methylimidazolium bis(trifluoromethyl-sulfonyl)imide	ultrasound synthesis	nanorods φ = 20 nm, l = 50-400 nm D = 15 nm S_{BET} = 50 m^2/g	Methyl orange degradation	C_{phot} = 0.5 g/L C_0 = 2 mg V_s = 100 mL t = 540 min	6 W UV light bulbs (λ = 360 nm)	Y = 38.7% Y_{ref} = no data	· high surface area · nanosphere morphologies	147

	solvent, template, and stabilizer,								
ZnO *2*	1-methyl-3-octylimidazolium bis(trifluoromethyl-sulfonyl)imide solvent, template, and stabilizer,		nanospheres φ = 10 nm D = 14.9 nm S_{BET} = 30.1 m^2/g				Y = 84.7% Y_{ref} = no data		
ZnO *3*	1-decyl-3-methylimidazolium bis(trifluoromethyl-sulfonyl)imide solvent, template, and stabilizer,		nanospheres φ = 10 nm D = 10.4 nm S_{BET} = 55 m^2/g				Y = 94.8% Y_{ref} = no data		
ZnO *4*	1-ethyl-2,3-dimethylimidazolium bis(trifluoromethyl-sulfonyl)imide solvent, template, and stabilizer,		nanorods φ = 20 nm l = 50-200 nm D = 10.7 nm S_{BET} = 19 m^2/g				Y = 78.1% Y_{ref} = no data		
ZnO *5*	butyltrimethylammonium bis(trifluoromethyl-sulfonyl)imide solvent, template, and stabilizer,		nanorods φ = 20 nm l = 50-200 nm D = 14.6 nm S_{BET} = 32.7 m^2/g				Y = 77.3% Y_{ref} = no data		
ZnO *6*	1-butyl-3-methylimidazolium thiocyanate solvent, template, and stabilizer,		nanorods φ = 20 nm l = 200-400 nm D = 11.4 nm S_{BET} = 29 m^2/g				Y = 88% Y_{ref} = no data		
ZnO *1*	1-butyl-2,3-dimethylimidazolium tetrafluoroborate morphology agent	solid-state reaction	nanoparticles φ = 10-20 nm S_{BET} = 34.651 m^2/g	Rhodamine B degradation	C_{phot} = 0.2 g/L C_0 = 10^{-5} mol/L V_s = 100 mL t = 80 min	125 W UV lamp	Y = 99.4% Y_{ref} = no data	· smaller diameters, · higher surface area · more intrinsic defects at the surface	148
ZnO *5*	1-butyl-3-methylimidazolium tetrafluoroborate		nanoparticles φ = 30-40 nm				Y = 98.5% Y_{ref} = n data		

	morphology agent								
ZnO *7*	1-ethyl-3-methylimidazolium tetrafluoroborate morphology agent		nanoparticles φ = 10-20 nm S_{BET} = 35.237 m^2/g				Y = 100% Y_{ref} = no		
ZnO *Zno-IL-1*	1-butyl-3-methylimidazolium hydroxide morphology controlling agent	hydrothermal	hexagonal disks and flower-like structure S_{BET} = 13.90 m^2/g D = 45.94 nm	Methyl orange degradation	C_{phot} = 0.3 g/L C_0 = 20 mg/mL V_s = 200 mL t = 240 min	125 W lamp	Y = ~15% Y_{ref} = ~90% ↘	· smaller size, · high surface area · more surface oxygen vacancies · low electron-hole recombination effect	149
ZnO *Zno-IL-2*	1-dodecyl-3-methylimidazolium hydroxide morphology controlling agent		hexagonal disks and rings S_{BET} = 9.05 m^2/g D = 58.75 nm				Y = ~ 25% Y_{ref} = ~90% ↘		
ZnO *Zno-IL-3*	(2-hydroxyethyl)-trimethylammonium hydroxide morphology controlling agent		nanospheres S_{BET} = 26.58 m^2/g D = 29.73 nm				Y = 100% Y_{ref} = ~90% ↗		
BiOI *BiOI porous microspheres*	1-butyl-3-methylimidazolium iodide source of I and template	solvothermal	uniform flower-like porous microspheres φ = 2-3 μm S_{BET} = 28.26 m^2/g	Methyl orange degradation	C_{phot} = 0.4 g/L C_0 = 10 mg/L V_s = 100 mL t = 180 min	two 150 W tungsten halogen lamps (>420 nm)	Y = 97% Y_{ref} = ~42%	· high surface area · high surface-to-volume ratios · energy band structure	122
BiOI *BiOI hollow microspheres*	1-butyl-3-methylimidazolium iodide solvent, source of I and template	solvothermal	hollow microspheres with a hole in the shell φ = 1-2 μm S_{BET} = 61.63 m^2/g	Methyl orange degradation	C_{phot} = 0.3 g/L C_0 = 10 mg/L V_s = 100 mL t = 180 min	two 150 W tungsten halogen lamps (>420 nm)	Y = 92% Y_{ref} = 21% ↗	· high BET surface area, · high surface-to-volume ratios · energy band structure	155

BiOI *IL-BiOI*	1-ethyl-3-methylimidazolium hexafluorophosphate additive	hydrothermal	non-uniform plates S_{BET} = 24.1 m^2/g	Methyl orange degradation	C_{phot} = 1 g/L C_0 = 10 mg/L t = 20 min	500 W Xe lamp (simulated sunlight)	k = 0.117 min^{-1} k_{ref} = 0.013 min^{-1} ↗	· higher specific surface area and the wavelength of phase response · decrease the particle size · increase the photoinduced charge separation rate	150
BiOBr *BiOBr-IL-1*	1-butyl-3-vinylimidazolium bromide template and reactant	solvothermal	porous microspheres φ = 2-3 μm S_{BET} = 44.79 m^2/g V_p = 0.094 cm^3/g	Rhodamine B degradation	C_{phot} = 10 mg/L C_0 = 30 mg V_s = 50 mL t = 105 min	500 W xenon lamp (>420 nm)	Y = 100% k = 0.266 min^{-1} Y_{ref} = ~40% k_{ref} = 0.0055 min^{-1} ↗	· higher surface area, · better porous microsphere structure · the narrower energy band gap	123
				Tetracycline degradation	C_{phot} = 10 mg/L C_0 = 20 mg V_s = 50 mL t = 80 min		Y = 90% Y_{ref} = ~16% ↗		
BiOBr *BiOBr-IL-2*	poly(1-butyl-3-vinylimidazolium bromide) template and reactant		microspheres with many ellipsoid structures S_{BET} = 25.9 m^2/g V_p = 0.065 cm^3/g	Rhodamine B degradation	C_{phot} = 10 mg/L C_0 = 30 mg V_s = 50 mL t = 105 min		Y = 60% k = 0.00972 min^{-1} Y_{ref} = ~40% k_{ref} = 0.0055 min^{-1} ↗		
				TetracyclineC degradation	C_{phot} = 10 mg/L C_0 = 20 mg V_s = 50 mL t = 80 min		Y = 28% Y_{ref} = ~16% ↗		
BiOBr *BiOBr-IL-3*	poly(1-butyl-3-vinylimidazolium bromide acrylamide) template and reactant		porous microspheres φ = 2-3 μm S_{BET} = 33.3 m^2/g V_p = 0.098 cm^3/g	Rhodamine B degradation	C_{phot} = 10 mg/L C_0 = 30 mg V_s = 50 mL t = 105 min		Y = 85% k = 0.0214 min^{-1}, Y_{ref} = ~40% k_{ref} = 0.0055 min^{-1} ↗		

				Tetracycline degradation	C_{phot} = 10 mg/L C_0 = 20 mg V_s = 50 mL t = 80 min		Y = 39% Y_{ref} = ~16% ↗		
BiOBr *Porous nanospheres*	1- hexadecyl-3-methylimidazolium bromide solvent, reactant, template	solvothermal	nanospheres, φ = 0.5–1 mm S_{BET} = 31.50 m^2/g	Rhodamine B degradation	C_{phot} = 10 mg/L C_0 = 0.2 g/L V_s = 100 mL t = 105 min	two 150 W tungsten halogen lamps (>420 nm)	Y = 97% Y_{ref} = 79% ↗	· high BET surface area, · smaller particle size · energy band structure	151
BiOCl *Choline chloride-BiOCl*	choline chloride Cl source and crystal control agent	precipitation	flower-like microsphere (the hollyhock) φ = 2–2.5 μm th = 30-50 nm S_{BET} = 16.35 m^2/g V_p=0.073 cm^3/g D = 14.13 nm	Rhodamine B degradation	C_{phot} = 10 mg/L C_0 = 1 mg/L V_s = 100 mL t = 120 min	1000 W iodine-tungsten lamp (>420 nm) or 150 W (UV light)	Y = 97.2% Y_{ref} =88.5% ↗	· higher specific surface area, · porous structure · thinner laminar	124
BiOCl *chlorinated pyridine-BiOCl*	chlorinated pyridine Cl source and crystal control agent		flower-like microsphere (the hollyhock with nanoplates) φ = 2-2.5 μm th = 50 nm S_{BET} = 13.74 m^2/g V_p = 0.064 cm^3/g D = 15.30 nm				Y = 96.3% Y_{ref} = 88.5% ↗		
BiOCl *imidazole chloride-BiOCl*	imidazole chloride Cl source and crystal control agent		flower-like microsphere with several nanoplates φ = 2-2.5 μm th = 50 nm S_{BET} = 13.54 m^2/ V_p = 0.071 cm^3/g D = 16.71 nm				Y = 92.4% Y_{ref} = 88.5% ↗		
$Bi_{12}TiO_{20}$ *$Bi_{12}TiO_{20}$*	1-butyl-3-methylimidazolium bromide structural agent	hydrothermal	nanorods φ = 20-30 nm l = 100-270 nm S_{BET} = 36.109 m^2/g	Methyl orange degradation	C_{phot} = 0.4 g/L C_0 = 10 mg/L V_s = 100 mL t = 180 min	300 W Xe lamp (>420 nm)	Y = 96.8% Y_{ref} = 66.7% ↗	· higher specific surface area, · the highest degree of crystallinity · one-dimensional	156

								morphology · the smallest bandgap energy · higher separation between the photoelectrons and vacancies	
Bi_2SiO_5 *IL-Bi_2SiO_5*	1-butyl-3-methylimidazolium tetrafluoroborate solvent and template	hydrothermal	nanosheet th = 37.6 nm S_{BET} = 55.6 m^2/g D = 10.53 nm φ_p = 10.0 nm	Rhodamine B degradation	C_{phot} = 1 g/L C_0 = 0.05 mmol/L t = 20 min	UV light	Y = 96.8% k = 0.070 min^{-1} Y_{ref} = 40% k_{ref} = 0.0087 min^{-1} ↗	· high BET surface area · lower electron-hole recombination	125
Bi_2SiO_5 *IL-Bi_2SiO_5 3%*	1-butyl-3-methylimidazolium tetrafluoroborate morphology controlling agent	solvothermal	flower-like shape assembled by sheets S_{BET} = 40.8 m^2/g	Rhodamine B degradation	C_{phot} = 1 g/L C_0 = 10 mg/L V_s = 50 mL t = 10 min	500 W high-pressure mercury light, UV light	Y = 87% k = 0.20 min^{-1} Y_{ref} = 37.4% ↗	· thinner sheets · higher specific surface area · presence of more OVs · lower electron-hole recombination	58
$BiPO_4$ *$BiPO_4$-H_2O*	1-methyl-3-octylimidazolium dihydrogen phosphate source of phosphate	solvothermal	nanorods with smooth surfaces and clear edges l = 300 nm S_{BET} = 9.16 m^2/g	Ciprofloxacin degradation	C_{phot} = 0.3 g/L C_0 = 10 mg/L V_s = 100 mL t = 120 min	250 W high-pressure Hg lamp, UV-Vis range	Y = 100% (100% after 90 min) Y_{ref} = ~65% ↗	different morphologies and surface microstructures	126
BiOBr *porous BiOBr*	1- hexadecyl-3-methylimidazolium bromide solvent, reactant, and template	solvothermal	incompact flower-like microspheres φ = 1 μm th = 5 nm D = 12.8 nm S_{BET} = 41.04 m^2/g	Rhodamine B degradation	C_{phot} = 0.2 g/L C_0 = 10 mg/L V_s = 100 mL t = 105 min	300 W Xe lamp (>400 nm)	Y = 100% Y_{ref} = 95% ~	· novel structure, · larger specific surface area · smaller particle size · narrower band gap structure	152
$SrSnO_3$ *S1/[C_4(mim)$_2$][Tf_2N]$_2$*	1-butyl-3-methylimidazolium bis(trifluoromethyl-sulfonyl)imide morphology directing agent	microwave	rod-shaped S_{BET} = 10.28 m^2/g D = 53.2 nm V_p =0.031 cm^3/g	H_2 generation	C_{phot} = 0.83 g/L sac. agent MeOH (0.83 g/L), V_s = 600 mL 0.025wt.% Rh	700 W Hg immersion lamp	Y = 99 μmol h^{-1} Y_{ref} = no data	· large surface area · nanosized crystals · suitable energy band structure	127

$SrSnO_3$ *S2/[C_6(mim)$_2$][Tf_2N]$_2$*	1,6-bis (3-methylimidazolium-1-yl)hexanebis(trifluoro-methylsulfonyl)-imide morphology directing agent		rod-shaped S_{BET} = 8.98 m^2/g D = 51.7 nm V_p =0.029 cm^3/g				Y = 90 μmol h^{-1} Y_{ref} = no data		
$SrSnO_3$ *S3/[P_{66614}]Tf_2N*	tetradecyltrihexyl-phosphonium bis(trifluoromethane-sulfonyl)amide morphology directing agent		rod-shaped S_{BET} = 6.58 m^2/g D = 51.6 nm V_p =0.022 cm^3/g				Y = 100 μmol h^{-1} Y_{ref} = no data		
$SrSnO_3$ *S4/[C_4Py]Tf_2N*	1-butylpyridinium bis(trifluoromethyl-sulfonyl)imide morphology directing agent		nanospheres φ = 50 nm S_{BET} = 11.48 m^2/g D = 40 nm V_p = 0.032cm^3/g				Y = 110 μmol h^{-1} Y_{ref} = no data		
SnS_2 *IL1*	1-butyl-3-methylimidazolium tetrafluoroborate structure-directing agent	microwave	desert rose like structures t = 150-200 nm S_{BET} = 6.50 m^2/g;	Rhodamine B degradation	C_{phot} = 0.3 g/L C_0 = 20 mg/L V_S = 100 mL t = 300 min	300 W Xe arc lamp (>420 nm)	Y = ~100% Y_{ref} = 66.2% ↗	· larger BET surface area	128
SnS_2 *IL2*	1-butyl-3-methylimidazolium bromide structure-directing agent		micro-sized spherical particles φ = 2–4 μm S_{BET} = 1.89 m^2/g				Y_{ref} = 66.2% Y = ~80% ↗		
SnS_2 *IL3*	1-hexyl-3-methylimidazolium chloride structure-directing agent		flowerlike microspheres φ = 2–3 μm t = 30-50 nm S_{BET} = 16.90 m^2/g				Y = ~100% Y_{ref} = 66.2% ↗		

SnS_2 *IL4*	1-butyl-3-methylimidazolium chloride structure-directing agent		flowerlike microspheres φ = 4–6 μm t = 30-50 nm S_{BET} = 14.47 m^2/g				Y= ~100% Y_{ref} = 66.2% ↗		
SnS_2 I*L5*	1-butyl-3-methylimidazolium acetate structure-directing agent		reunited nanoparticles φ = 100–200 nm S_{BET} = 23.15 m^2/g				Y= ~100% Y_{ref} = 66.2% ↗		
Cellulose/ SnS_2 *IL4*	1-butyl-3-methylimidazolium chloride structure-directing agent		flower-like structure composed of 2D SnS_2 nanoplates tightly anchored on the surface of cellulose S_{BET} = 23.15 m^2/g				Y = ~100% (after 150 min) Y_{ref} = 66.2% ↗	· larger BET surface area · lower electron hole recombination	
Bi_2WO_6-Bi_2O_3 *BWA400*	1-allyl-3-methylimidazolium chloride structure-controlling agent, template	two steps: solvothermal and calcination	flower-like hierarchical microspheres assembled by nanosheets φ = 2.8 μm S_{BET} = 30.71 m^2/g V_p = 0.1452 cm^3/g	H_2 generation	C_{phot} = 0.5 g/L V_s = 100 ml sacr. agent: containing 2.4 g Na_2S, 17.55 g NaCl and 0.5 g Na_2SO_3 t = 120 min	300 W Xe lamp (>420 nm)	UV-Vis: Y =878 μmol/g·h Y_{ref} = 447 μmol/g·h Vis: Y_{H2} = 58 μmol/g·h ↗	· increased surface area · matching band structure, · lower electron-hole recombination	131
Bi_2WO_6-Bi_2O_3 *BWB400*	1-butyl-3-methylimidazolium chloride structure-controlling agent, tmplate		flower-like hierarchical microflowers assembled by nanosheets φ = 1.7-33 μm S_{BET} = 25.90 m^2/g V_p = 0.0581 cm^3/g				UV-Vis: Y = 814 μmol/g·h Y_{ref} = 447 μmol/gh ↗		
In_2S_3/TiO_2 *S0.5*	1-butyl-2,3-dimethylimidazolium chloride and 1-butyl-3-methylimidazolium chloride	microwave-assisted solvothermal synthesis	In_2S_3 nanoparticles on the TiO_2 mesoporous surface S_{BET} = 225.0 m^2/g	H_2 generation	C_{phot} = 0.5 g/L sac. agent MeOH V_s = 100 mL t = 1 h	300 W Xenon arc lamp	Y = 637.9 μmol/g·h Y_{ref} = 111.3 μmol/g·h ↗	· small size of In_2S_3 on TiO_2, · higher surface area, · promoted charge transfer	132

	reagent, morphology-controlling agent		V_p = 0.31 cm^3/g φ_p = 5.55 nm					· lower electron-hole recombination	
MoS_2/Bi_5O_7I *0.2 wt.% MoS_2/Bi_5O_7I*	1-ethyl-3-methylimidazolium iodide I source and dispersant	solvothermal	MoS_2 nanosheets attached on the surface of Bi_5O_7I nanorods S_{BET} = 56.4603 m^2/g	Bisphenol A degradation	C_{phot} = 0.5 g/L C_0 = 10 mg/L V_s = 100 mL t = 60 min	300 W (>400 nm)	Y = 99% Y_{ref} = 10% ↗	· higher specific surface area increased light-capturing ability, · lower electron-hole recombination · improved utilization efficiency	133
				Ciprofloxacin degradation	C_{phot} = 0.5 g/L C_0 = 10 mg/L V_s = 100 mL t = 120 min		Y = ~60% Y_{ref} = ~6% ↗		
				Tetracycline degradation	C_{phot} = 0.3 g/L C_0 = 20 mg/L V_s = 100 mL t = 60 min		Y = ~82% Y_{ref} = ~11% ↗		
BiOBr/BiOCl *HE-BiOCl*	1-allyl-3-methylimidazolium bromide Br source and morphology controlling agent	solvothermal	flower-like shape assembled by thin sheets S_{BET} = 36.5 m^2/g	Rhodamine B degradation	C_{phot} = 10 mg/L C_0 = 1 g/l t = 50 min	500 W Xe lamp	k = 0.0595 min^{-1} k_{ref} = 0.0090 min^{-1} ↗	· higher surface area · lower electron-hole recombination	134
BiOCl/m-$BiVO_4$ *S4*	1-butyl-3-methylimidazolium chloride Cl source	ultrasonic	square blocks are self-assembled by numerous nanoplates th nanoplates = 10-20 nm S_{BET} = 4.00 m^2/g V_p = 0.0322 cm^3/g φ_p = 42.35 nm	Rhodamine B degradation	C_{phot} = 1 g/L C_0 = 2x10^{-5} M V_s = 50 mL t = 180 min	350 W Xe lamp (>400 nm)	Y = 99% Y_{ref} = 16% ↗	· larger pore volume and pore size · lower electron-hole recombination	135

BiOBr/BiOCl *IL-BiOCl*	1-butylpyridinium bromide Br source and morphology directing agent	hydrothermal	flower-like structure assembled by sheets S_{BET} = 30.0 m^2/g V_p = 0.010 cm^3/g	Rhodamine B degradation	C_{phot} = 1 g/L C_0 = 10 mg/L V_s = 100 mL t = 90 min	500 W Xe visible light	k = 0.021 min^{-1} k_{ref} = 0.008 min^{-1} ↗	· higher specific surface area · lower electron-hole recombination by interfacial electric field formed by the BiOBr/BiOCl heterojunctions	158
rGO_Bi_2WO_6 *5.0%-RGO–BWO*	1-butyl-3-methylimidazolium tetrafluoroborate dispersant agent, morphology directing agent	hydrothermal	nest-like structures φ = 3–5 mm S_{BET} = 45.5 m^2/g	Rhodamine B degradation	C_{phot} = 0.1 g/L C_0 = 10 mg/L V_s = 100 mL t = 120 min	300 W Xe visible irradiation	Y = 93.1% Y_{ref} = ~30% ↗	· higher surface area · lower electron-hole recombination	136
NH_2-UiO-66/BiOBr *NU/BOB-15*	1- hexadecyl-3-methylimidazolium bromide Br source	solvothermal	BiOBr nanosheets distributed uniformly on the outer surface of NH_2-UiO-66 octahedrons S_{BET} = 70.64 m^2/g	Tetracycline degradation	C_{phot} = 0.4 g/L C_0 = 20 mg/L V_S = 100 mL t = 150 min	250 W Xe lamp (>400 nm)	Y = 75% k = 0.0104 min^{-1} Y_{ref} = 50 % ↗	· higher BET surface area	137
				Cr(VI) degradation	C_{phot} = 1 g/L C_0 = 10 mg/L V_S = 100 mL t = 360 min		Y = 88% Y_{ref} = 56 % ↗		
ZrO_2@ HKUST-1 *ZrO_2@ HKUST-1*	N,N,N,N',N',N'-hexakis-(2-hydroxyethyl)ethane-1,2-diaminium bromide deprotonation agent	sol-gel	MOF octahedrons with rough surface due to formation of ZrO_2 S_{BET} = 1152 m^2/g V_p = 0.88 cm^3/g	Cyhalothrin degradation	C_{phot} = 0.33 g/L C_0 = 60 mg/L V_S = 30 mL t = 360 min	14 W, visible light	Y = 99.6% Y_{ref} = 33.8 % ↗	· higher BET surface area	138
g-C_3N_4/ $Bi_4O_5Br_2$ *10 wt% g-C_3N_4/$Bi_4O_5Br_2$*	1- hexadecyl-3-methylimidazolium bromide solvent, dispersing agent and reactant	solvothermal	rod-like g-C_3N_4 combined with sheet-like $Bi_4O_5Br_2$	Ciprofloxacin degradation	C_{phot} = 0.5 g/L C_0 = 10 mg/L V_S = 100 mL t = 150 min	300 W Xe arc lamp visible light	Y= 67% Y_{ref} = 48 % ↗	· regular dispersion	154

				Rhodamine B degradation	C_{phot} = 0.5 g/L C_0 = 10 mg/L V_S = 100 mL t = 150 min		Y = 81% Y_{ref} = 42 % ↗		
$Cu_2S–MoS_2$ *$Cu_2S–MoS_2(1:1)$*	1-butyl-3-methylimidazolium thiocyanate sulfur source, Structure-directing agent	hydrothermal	nanoflowers assembled from nanosheets φ = 0.8-1.0 μm S_{BET}= 49 m^2/g	Methylene blue degradation	C_{phot} = 0.83 g/L C_0 = 10^{-4} mol/L V_S = 60 mL t = 75 min	500 W Xe lamp	Y = ~100% k = 0.0471 min^{-1} Y_{ref} = ~30% ↗	· larger BET surface area, more regular shape	139
Ag_3PO_4/ $BiPO_4$ *Ag_3PO_4/ $BiPO_4$ in RTIL*	2-hydroxylethyl-ammonium formate solvent, surface directing agent	hydrothermal co-precipitation	agglomerated rods of $BiPO_4$ with spherical-like Ag_3PO_4 on the surface	Reactive blue 21 degradation	C_{phot} = 0.01 g/L C_0 = 10 ppm V_S = 100 mL t = 120 min	125 W high-pressure Hg lamp 400–700 nm	UV: Y = 93% $Y_{ref\ BiPO4}$ = 65.2% $Y_{ref\ Ag3PO4}$ = 25.3% ↗ Vis: Y = 80.52% $Y_{ref\ BiPO4}$ = 6.3% $Y_{ref\ Ag3PO4}$ = 34.4% ↗	· lower particle size · lower electron hole recombination	140
BiOCl/BiOBr *BiOCl/BiOBr*	1- hexadecyl-3-methylimidazolium bromide and 1- hexadecyl-3-methylimidazolium chloride solvent, reactant, template	solvothermal	flower-like microspheres φ = 0.5–1 μm th = 5-10 nm	Rhodamine B degradation	C_{phot} = 0.2 g/L C_0 = 10 mg/L V_S = 100 mL t = 60 min	300 W Xe lamp (>400 nm)	Y = 99% $Y_{ref\ BiOBr}$ = 73% $Y_{ref\ BiOCl}$ = 66% ↗	larger BET surface area lower electron hole recombination	153

7) Surface modification

In photocatalytic reactions, various subsequent processes occur at the interface between the semiconductor and the components of the reaction medium. These steps typically involve the initial adsorption of reactants, followed by the reaction itself, and finally the desorption process[17]. Therefore, improvement of photocatalytic properties can occur by enhancing the adsorption of specific molecules on a semiconductor surface[163,164]. This increased adsorption promotes a higher concentration of reactants at the surface, facilitating more efficient photocatalytic reactions. One way to influence the adsorption of reactants is to modify the semiconductor surface with ionic liquids. ILs or IL-derived residues formed during synthesis can alter the surface charge, polarity, and enter functional groups, affecting the adsorption behavior of reactant molecules on a semiconductor surface.

Table 7 provides an overview of the enhancement of photocatalytic activity through surface modification of semiconductors using ionic liquids. These modifications can indeed be carried out during the synthesis of the semiconductor material[165] or as a post-synthesis modification[166]. In some cases, an ionic liquid was added directly to the semiconductor during the investigation of photocatalytic activity[167]. Surface modification using ILs was carried out on various semiconductor materials, including TiO_2[167], C_3N_4 [168], as well as the bismuth-based compounds $BiOBr/Bi_2WO_6$[169] and BiOI [165]. In most cases, ionic liquids (ILs) were applied to the surface of semiconductors using the impregnation method. To achieve surface modification aimed at enhancing photoactivity the following ILs have been employe 1-butyl-3-methylimidazolium imidazolate, 1-butyl-1-metylpyrrolidinium imidazolate, tributylethylphosphonium imidazolate $[(But)_3EP][Im]$, $[P_{4444}]_3$[p-2,6-O-4-COO], $[P_{4444}]_2$[p-2-O-4-COO], $[P_{4444}]$[p-2-O], [P4444][p-4-COO][170], 1-butyl-3-methylimidazolium tetrafluoroborate[167], 1-butyl-3-methylimidazolium iodide[165], 1-butylpyridinium bromide[169], 1-butyl-3-methylimidazolium chloride[166], 1-butyl-3-methylimidazolium bis(trifluoromethylsulfonyl)imide[166], 1-ethyl-3-methylimidazolium tetrafluoroborate[168].

The presence of the 1-butyl-3-methylimidazolium cation was found to promote the adsorption of methyl orange molecules onto the TiO_2 surface[167]. Suppression of recombination in photoinduced electron-hole pairs in BiOI was possible to achieve by effectively capturing and trapping the photogenerated electrons through the surface modification provided by 1-butyl-3-methylimidazolium iodide[165]. The N- and Br-modified surface of $BiOBr/Bi_2WO_6$ originated from the application of 1-butylpyridinium bromide enhanced photocatalytic activity in the degradation of phenol under visible light[169]. Liu et al.[168] discovered that the incorporation of 1-ethyl-3-methylimidazolium tetrafluoroborate into the Co-B-C_3N_4 surface resulted in enhanced efficiency in the conversion of CO_2 into CH_4 and CO through photocatalysis. This improvement was attributed to the surface loading of IL, which acted as a cocatalyst, facilitating the achievement of superior photocatalytic performance. Additionally, the impregnation of TiO_2 with IL led to modifications in the surface electronic structure. It was observed that TiO_2-bearing imidazolate anions from the IL reduced the activation energy barrier for the CO_2 photoreduction reaction[166]. On the other hand, Łuczak et al. [12] found out that ILs or organic residues derived from ILs can create a unique form of surface modification that enhances photocatalytic activity in the phenol degradation reaction. This surface modification of TiO_2 involves covering the surface with an amorphous layer consisting of either hydrophobic organic residues or hydrophilic, likely ionic, organic residues.

Surface modifications of semiconductors using ILs can be identified using a wide range of techniques, such as: XPS[12], FTIR[171,172], DRS UV-Vis,[99] and electrophoretic mobility[173] measurements. For example, the IR spectrum of IL-modified BiOI and 1-butyl-3-methylimidazolium iodide exhibited distinct peaks at 1170, 815, and 714 cm^{-1}, which were absent in the spectrum of the reference sample (P-BiOI)[165]. These peaks, indicative of plane deformation and out-of-plane deformation of the C-H bond suggested successful surface modification of BiOI by ILs. The confirmation of IL surface impregnation can be achieved by analyzing the C1s spectrum, particularly through the detection of components attributed to the C=C aromatic carbon bond. Additionally, the presence of IL species on the surface can also be confirmed by examining the N1s and Br 3d spectra[169].

The field of semiconductor surface modification with ILs has shown promising results, particularly in photocatalytic applications. However, to fully harness this potential, several key areas require further exploration and improvement. Current research primarily utilizes a limited range of ionic liquids. The development of methods enabling the adsorption of ionic liquids during semiconductor synthesis must ensure that the ionic liquids are effectively integrated without undergoing degradation or decomposition. A deeper understanding of the photocatalytic reactions in the presence of ionic liquids is essential. This can be achieved by corroborating experimental findings with theoretical studies. Such an approach would provide a more comprehensive understanding of how these reactions occur and the role ionic liquids play in them. Determining the universal role of ionic liquids, based on their type, in photocatalytic reactions would be a significant advancement.

Known: the creation of junctions between semiconductors and ILs, increases photoactivity by lowering energy activation,

Unknown: more specific role of ILs depending on ILs structure, stability of ILs during measurements, effect on mass and charge carrier transfer as well as selectivity of reaction.

Table 7. *Category: surface modification.* Preparation conditions, morphology, photocatalytic performance of photocatalysts prepared by ILs-assisted synthesis methods*,**.

Explanation of abbreviations used below in the column:
- *surface properties*: diameter (φ), thickness (th), length (l), width (w), crystallite size (D) specific surface area (S_{BET}), pore volume (V_p), pore size (φ_p), aspect ratio,
- *conditions*: photocatalyst content (C_{phot}), the concentration of model pollutant (C_0), sacrificial agent (sacr. agent), volume of solution (Vs), irradiation time (t),
- *efficiency:* yield (Y)/rate (r)/rate constant (*k*) of the most active sample (Y), and the reference sample (Y_{ref}), ↗ - increase, and ↘ decrease compared to the reference sample.

*The table includes all available information.
**The original sample label is given in italics.

Photocatalyst and original sample label	Ionic liquid and its role in the synthesis	Synthesis method	Surface properties	Photocatalytic performance				Mechanism details	Ref.
				Type of model reaction	Conditions	Light source	Yield (Y)/rate (r)/rate constant (*k*)		
TiO_2 *MO+IL*	1-buty-3-methylimidazolium tetrafluoroborate additive	the addition of IL to the solution of P25 during the photocatalytic test	-	Methyl orange degradation	C_{phot} = 2 g/L C_0 = $5.0 \cdot 10^{-5}$ M t = 90 min	300 W Xe lamp 20 mW/cm^2	Y = ~95% Y_{ref} = ~92% ↗	· enhanced pollutant sorption	167
				Rhodamine B degradation	C_{phot} = 2 g/L C_0 = $1 \cdot 10^{-5}$ M t = 90 min		Y = ~55% Y_{ref} = ~92% ↘	· weakened pollutant sorption	
BiOI *IL-BiOI*	1-buty-3-methylimidazolium iodide source of I and surface modified agent	chemical precipitation	thin nanoflakes th = 40 nm S_{BET} = 8.2 m^2/g	Methyl orange degradation	C_{phot} = 1 g/L C_0 = 10 mg/L V_s = 100 mL t = 180 min	500 W tungsten halogen lamp (>*420* nm)	Y = 87% k = 0.569 h^{-1}, Y_{ref} = 27% k_{ref} = 0.081 h^{-1} ↗	· IL surface modification inhibited recombination of photoinduced electron-hole	165
				Salicylic acid degradation	C_{phot} = 1 g/L C_0 = 10 mg/L t = 240 min		Y = 46%, Y_{ref} = 15% ↗		
$BiOBr/Bi_2WO_6$ *$BiOBr/Bi_2WO_6$_1*	1-butylpyridinium bromide Br source, N source, morphology directing agent	I step: anodization, II step: hydrothermal	BiOBr plates cover Bi_2WO_6 flower-like surface	Phenol degradation	anodized surface of thin film C_0 = 20 mg/L V_s=8 mL t = 240 min	1000 W Xenon lamp (>420 nm)	Y = 44% Y_{ref}= 16% ↗	· N-modified surface · interactions of bromide ions	169
TiO_2 *TiO_2@[BMIm][Im]*	1-butyl-3-methylimidazolium imidazole	impregnation method	nanoparticles S_{BET} = 19.2 m^2/g	CO_2 reduction	C_{phot} = 10 g/L C_0 = 50 bar of CO_2	300 W Xenon lamp	Y = 455±96 µmol/g Y_{ref} = 3±1 µmol/g ↗	· red shift and thus a modification of the TiO_2 surface	166

	additive				V_s = 2 mL t = 120 min			electronic structure · TiO_2 with IL bearing imidazolate anions lowered the CO_2 activation energy barrier	
TiO_2 *TiO_2@[BMPy][Im]*	1-butyl-1-metylpyrrolidinium imidazolate additive		nanoparticles S_{BET} = 33.8 m^2/g				Y = 80±7 µmol/g Y_{ref} = 3±1 µmol/g ↗		
TiO_2 *TiO_2@[(But)$_3$EP][Im]*	tributylethyl-phosphonium imidazolate additive		nanoparticles S_{BET} = 29.2 m^2/g				Y = 207±16 µmol/g Y_{ref} = 3±1 µmol/g ↗		
TiO_2 *TiO_2@[BMIm]Cl*	1-butyl-3-methylimidazolium chloride additive		nanoparticles S_{BET} = 20.8 m^2/g				Y = 220±23 µmol/g Y_{ref} = 3±1 µmol/g ↗		
TiO_2 *TiO_2@[BMIm][NTf$_2$]*	1-butyl-3-methylimidazolium bis(trifluoromethyl-sulfonyl)imide additive		nanoparticles S_{BET} = 18.9 m^2/g				Y = 101±55 µmol/g Y_{ref} = 3±1 µmol/g ↗		
TiO_2 *TiO_2−[P$_{4444}$]$_3$[p-2,6-O-4-COO]*	[P$_{4444}$]$_3$[p-2,6-O-4-COO] additive	the addition of IL to the solution of P25 during the photocatalytic test	φ = 5−10 nm	CO_2 reduction	C_{phot} = 0.4 g t = 600 min	300 W Xenon lamp (>420 nm)	Y = 3.52 µmol/g·h Y_{ref} = 0.13 µmol/g·h ↗	· immobilized IL on the TiO_2 may serve as an absorbent and photosensitizer	170
TiO_2 *TiO_2−[P$_{4444}$]$_2$[p-2-O-4-COO]*	[P$_{4444}$]$_2$[p-2-O-4-COO] additive						Y = 0.19 µmol/g·h Y_{ref} = 0.13 µmol/g·h ↗		
TiO_2 *TiO_2−[P$_{4444}$][p-2-O]*	[P$_{4444}$][p-2-O] additive						Y = 0.10 µmol/g·h Y_{ref} = 0.13 µmol/g·h ↘		
TiO_2 *TiO_2−[P$_{4444}$][p-4-COO]*	[P$_{4444}$][p-4-COO] additive						Y = 0.10 µmol/g·h Y_{ref} = 0.13 µmol/g·h ↘		
IL/Co-B-C_3N_4 *IL/Co-bCN*	1-ethyl-3-methylimidazolium tetrafluoroborate additive	impregnation	ultrathin silky nanosheets with random mesopores	CO_2 reduction	Pressure: 15 bar (CO_2) Sacr. agent: water C_{phot} = 16.7 g/L	300 Xenon lamp	Y_{CH4} = 6.3 µmol/h·g Y_{CO} = 40.5 µmol/h·g $Y_{ref\text{-}CH4}$ = 1.7 µmol/h·g $Y_{ref\text{-}CO}$ = 3.9 µmol/h·g ↗	· surface loaded with IL playing role of cocatalyst	168

					V_s = 3 mL t = 240 min				

8) Thickness control

Ultrathin two-dimensional (2D) materials composed of single, or few layers have garnered significant interest owing to their fascinating physical-chemical properties. As photocatalytic materials decrease in thickness, they exhibit novel properties that are not present in analogous three-dimensional (3D) counterparts[174,175]. 2D materials typically have a higher surface area that provides more active sites for catalytic reactions. This increased surface area is attributed to the unique geometry of 2D materials (having length and width, but negligible thickness). Among their advantages can be mentioned: (i) more exposed active sites (atoms or functional groups on the surface of 2D materials are more exposed and accessible, making them more reactive), and (ii) more efficient adsorption of reactant molecules onto the material's surface. Besides, 2D materials possess shorter diffusion paths resulting in faster charge carrier transport, reducing the likelihood of recombination and enhancing the overall efficiency of the photocatalytic process[176,177]. They can exhibit enhanced light absorption due to the quantum confinement effect and reduced light reflection[178,179]. Controlling the thickness allows for tuning the band alignment, ensuring that the energy levels of the valence and conduction bands are suitable for promoting charge separation and facilitating redox reactions. Evaluation of material thickness can be conducted using SEM[180–185], TEM [180–187], AFM [180,182], and high-angle annular dark-field scanning transmission electron microscopy (HAADF-STEM)[188]. These techniques insights into the morphological characteristics and thickness uniformity of the synthesized materials.

The application of specific ILs, as illustrated in Table 8, such as 1-hexyl-3-methylimidazolium iodide[184,185], 1- hexadecyl-3-methylimidazolium bromide[180–182,187,189], 1-butyl-3-methylimidazolium iodide[186], and tetrabutylammonium chloride[183], played the crucial role in the precise regulation of the thickness of ultrathin 2D materials. Imidazolium-based ILs are commonly employed in the synthesis of 2D ultrathin nanosheets due to their unique properties. The formation of hydrogen bonds between the hydrogen atom in ILs' aromatic ring and the oxygen atoms from the external plane of photocatalysts facilitates the uniform adsorption of nuclei at the initiation of the reaction. By adjusting the amount of IL, control over the number of adsorbed hydrogen bonds on the crystal surface is achieved, leading to preferential growth along the 2D direction[190].

The literature data demonstrate that ILs have a significant impact on the morphology to form thinner nanosheet structures. It is known that ILs can work in two ways (i) provide halogen atoms to form photocatalyst 2D nanostructures[182,184,185], and (ii) as morphology-directing agents facilitating the formation of ultrathin materials in the range of 3 – 8 nm[182,183]. In addition, the presence of ILs could potentially influence the growth and stability of the nanosheets during the synthesis [180]. It can be inferred that these ultrathin nanosheets have a notably brief distance for the diffusion of photoinduced carriers. This characteristic proves advantageous in effectively separating and transferring photoinduced carriers from the bulk phase to the surface of the photocatalyst, thus contributing to improved photocatalytic performance[185,187]. In the case of heterojunction, IL as a source of halogen atoms can form a bridge to facilitate the intimate integration of two different components and play a crucial role in the formation and stabilization of heterojunctions[181]. In addition, the uniform dispersion of ultrasmall nanosheets on the ultrathin photocatalyst surface ensures a well-distributed and intimate contact between the 2D-2D materials[184].

While the use of ionic liquids (ILs) in the synthesis of 2D photocatalysts can offer several advantages, it's essential to consider potential challenges or "white spots" that may arise. The presence of residual ILs can alter the material properties and affect photocatalytic performance. It's crucial to develop effective methods for IL removal to ensure the purity of

the final product. Currently, little is said about the methods of how to remove them. To optimize IL-assisted synthesis, researchers need to delve deeper into the mechanisms through which ILs interact with precursor materials, affect growth processes, and influence the resulting morphology and properties of 2D photocatalysts. Understanding how ILs influence the band structure, energy levels, and charge carrier dynamics is crucial for tailoring these materials for specific photocatalytic applications.

Known: facilitate formation of ultrathin materials (morphology-directing agent); provide halogen atoms to form 2D materials, bridge heterojunctions, and ensure uniform dispersion of ultrasmall nanosheets on the photocatalyst surface in 2D-2D materials;

Unknown: mechanisms of IL or its residual interaction with precursor of 2D materials;

Table 8. *Category: thickness control <10 nm.* Preparation conditions, morphology, photocatalytic performance of photocatalysts prepared by ILs-assisted synthesis methods*, **.

Explanation of abbreviations used below in the column:
- *surface properties*: shape (s), diameter (φ), thickness (th), length (l), width (w), crystallite size (D) specific surface area (S_{BET}), pore volume (V_p), pore size (φ_p), aspect ratio,
- *conditions*: photocatalyst content (m_{phot}), the concentration of model pollutant (C_0), sacrificial agent (sacr. agent), volume of solution (Vs), irradiation time (t),
- *efficiency:* yield (Y)/rate (r)/rate constant (*k*) of the most active sample (Y_{phot}), and the reference sample (Y_{ref}), ↗ - increase, and ↘ decrease compared to the reference sample.

*The table includes all available information.
**The original sample label is given in italics.

Photocatalyst and original sample label**	Ionic liquid and its role in the synthesis	Synthesis method	Surface properties	Photocatalytic performance				Mechanism details	Ref.
				Type of model reaction	Conditions	Light source	Yield (Y)/rate (r)/rate constant (*k*)		
BiOBr *BiOBr-IL*	1- hexadecyl-3-methylimidazolium bromide reactant and morphology-directing agent	mechanochemical	ultrathin nanosheets φ = 200–300 nm th = 3–4 nm, S_{BET}=6.6 m^2/g	Bisphenol A degradation	C_{phot} = 0.5 g/L C_0 = 10 mg/L V_s = 100 mL t = 180 min	300 W Xe lamp (>400 nm)	Y = 87% k = 0.61 h^{-1} Y_{ref} = 41.1% k_{ref} = 0.16 h^{-1} ↗	· thickness regulation · shorter photoinduced carrier diffusion distance, · lower electron-hole recombination	182
				Tetracycline degradation	C_{phot} = 0.5 g/L C_0 = 20 mg/L V_s = 100 mL t = 120 min		Y = 41.4%, Y_{ref} = 19.61% ↗		
				Rhodamine B degradation	C_{phot} = 0.2 g/L C_0 = 10 mg/L V_s = 100 mL t = 60 min		Y = ~83.5% Y_{ref} = ~10% ↗		
$Bi_4O_5Br_2$ *$Bi_4O_5Br_2$*	1- hexadecyl-3-methylimidazolium bromide solvent, reactant, template	solvothermal	numerous irregular ultrathin nanosheets stacked together th = 6 nm	Bisphenol A degradation	C_{phot} = 0.5 g/L C_0 = 10 mg/L V_s = 100 mL t = 210 min	300 W Xe lamp (UV filter)	Y = 91.2% k = 0.01086 min^{-1} Y_{ref} = 24.4% k_{ref}= 0.00136 min^{-1} ↗	· thickness regulation · reduced band gap · lower electron-hole recombination	187
$Bi_4O_5Br_2$ *$Bi_4O_5Br_2$*	1- hexadecyl-3-methylimidazolium bromide solvent, reactant, template	solvothermal	ultrathin nanosheets φ = 100 nm-1 μm th = 8 nm l=120 nm w = 70 nm S_{BET} = 12.98 m^2/g	Ciprofloxacin degradation	C_{phot} = 0.5 g/L C_0 = 10 mg/L V_s = 100 mL t = 120 min	300 W Xe lamp (λ>400 nm)	Y = 75% k = 0.0113 min^{-1} Y_{ref} = 51.4% k_{ref} = 0.0059 min^{-1} ↗	· ultrathin structure · lower electron-hole recombination	180

$Bi_4O_5I_2$ *$Bi_4O_5I_2$*	1-hexyl-3-methylimidazolium iodide solvent, capping agent, and I source	solvothermal	ultrasmall nanosheets consisted of about 6 layers φ = 37-52 nm th = 5-6 nm S_{BET} = 49.04 m^2/g	Rhodamine B degradation	C_{phot} = 0.2 g/L C_0 = 10 mg/L V_s = 100 mL t = 120 min	300 W Xe lamp (>400 nm)	Y = 99% k = 0.0319 min^{-1} Y_{ref} = 50% ↗	· ultrasmall few-layer structure · efficient separation of electron-hole pairs · lower valence position	185
				Ciprofloxacin degradation	C_{phot} = 0.5 g/L C_0 = 10 mg/L V_s = 100 mL t = 240 min		Y = 80% Y_{ref}=~0% ↗		
$C_3N_4/Bi_4O_5I_2$ *3 wt% ultrathin $C_3N_4/Bi_4O_5I_2$*	1-hexyl-3-methylimidazolium iodide I source, template, and dispersing agent	solvothermal	ultrathin C_3N_4 and $Bi_4O_5I_2$ nanomaterials th = 6 nm ($Bi_4O_5I_2$ nanosheets) S_{BET} = 41.07 m^2/g	Rhodamine B degradation	C_{phot} = 0.2 g/l C_0 = 10 mg/L V_s = 100 mL t = 120min	300 W Xe lamp (>400 nm)	Y=~95% Y_{ref}=~55% ↗	· well dispersion of ultra-small nanosheets on ultrathin structure · lower electron-hole recombination	184
				Bisphenol A degradation	$C_{pho\ t}$= 0.5 g/L C_0 = 10 mg/L V_s = 100 mL t = 60 min		Y = 100% (~90% after 20 min) Y_{ref} = 100% (35% after 20 min) ↗		
$C_3N4/Bi_4O_5Br_2$ *1 wt% g-$C_3N_4/Bi_4O_5Br_2$*	1- hexadecyl-3-methylimidazolium bromide Br source, template, and dispersing agent	solvothermal	ultrathin $Bi_4O_5Br_2$ nanosheets dispersed on g-C_3N_4 nanosheets th =7 nm ($Bi_4O_5Br_2$ nanosheets) S_{BET}= 156.2 m^2/g	Ciprofloxacin degradation	C_{phot} = 0.5 g/L C_0 = 10 mg/L V_s = 100 mL t = 150 min	300 W Xe lamp (>400 nm)	Y = ~70% Y_{ref} = ~40% ↗	· 2D-2D ultrathin structure · matched energy band structure · lower electron-hole recombination	189
				Rhodamine B degradation	C_{phot} = 0.1 g/L C_0 = 10 mg/L V_s = 100 mL t=75 min		Y_{phot} = 91% Y_{ref} = 65% ↗		
N-CQDs/BiOBr *N-CQD/BiOBr-3*	1- hexadecyl-3-methylimidazolium bromide Br source, dispersing agent	solvothermal	BiOBr nanosheets decorated with spherical N-CQDs l_{BiOBr} = w_{BiOBr} = 100-400 nm th_{BiOBr}=~12 nm φ_{CQDs} = ~6 nm S_{BET} = 6.86 m^2/g	Ciprofloxacin degradation	C_{phot}=0.5 g/L C_0=10 mg/L V_S=100 mL t=120 min	300 W Xe lamp (>400 nm)	Y = 88% Y = 40.1% ↗	· ultrathin structure · regular dispersion	181
				Rhodamine B degradation	C_{phot}=0.2 g/L C_0=10 mg/L V_S=100 mL t=50 min		Y = 96.5% (after 30 min) Y_{ref} = ~80% ↗		
				Tetracycline degradation	C_{phot} = 0.5 g/L C_0 = 20 mg/L V_S = 100 mL t = 120 min		Y =67.1% Y_{ref} = 38.6% ↗		
				Rhodamine B degradation	C_{phot} = 0.5 g/L C_0 = 10 mg/L V_S = 100 mL t = 210 min		Y=~60% Y_{ref}=~25% ↗		

Bi_2WO_6 *IL_BWO3*	tetrabutylammonium chloride morphology directing agent	solvothermal	ultrathin nanosheets th = 8 nm S_{BET} = 47.60 m^2/g V_p = 0.0232 cm^3/g	Phenol degradation	C_{phot} = 5 g/L C_0 = 20 mg/L V_s = 25 mL t = 60 min	1000 W Xenon lamp (UV–Vis light)	Y = 86% k = 0.0282 min^{-1} Y_{ref} = 38% ↗	· ultrathin structure · formation of OV	183
GO-BiOI *1 wt% GO/BiOI*	1-butyl-3-methylimidazolium iodide I source, soft template, capping agent	solvothermal	narrow and long BiOI nanoplates randomly dispersed on 2D graphene sheets	Rhodamine B degradation	C_{phot} = 0.2 g/L C_0 = 10 mg/L V_S = 100 mL t = 100 min	300 W Xe lamp (>400 nm)	Y_{ref} = ~90% Y_{phot} = 98.8% ↗	· 2D structure · lower electron-hole recombination	186

Conclusions and future prospect

Increasing the maturity of technology using heterogeneous photocatalysis requires rational design and synthesis of new photocatalytic materials and application of reagents affecting the final properties of obtained materials, such as ionic liquids-assisted materials. Thus, this paper distinguishes and summarizes eight main mechanisms describing interactions between ionic liquids and growing semiconducting particles and their final effect on surface and photocatalytic properties of semiconductors, i.e.: (i) doping of elemental atoms from ILs, (ii) surface defect formation, (iii) formation of charge transfer surface complex, (iv) promoting of charge transfer; (v) facet-control synthesis; (vi) altering size and porosity of materials, (vii) affecting sorption properties due to presence of ILs, and (viii) regulating the thickness of synthesized materials.

The choice of ionic liquids for the synthesis of semiconductor particles should be preceded by a theoretical consideration of how this ionic liquid will behave during synthesis, including whether it will not decompose during solvothermal synthesis. Very generally it can be stated that ionic liquids that are not stable under elevated temperature and pressure conditions could be used as a source of elements doped into the crystal structure of semiconductor particles and finally affect their band structure. On the other hand, ionic liquids surviving conditions of solvothermal synthesis could be adsorbed at the surface of the semiconductor and form a charge-transfer complex between an electron acceptor (semiconductor) and an electron donor (surface adsorbate). This kind of interaction (i.e. the presence of CT-complex) could shift the photoactivity of semiconducting materials from the UV region to visible light.

The wide spectrum of imidazolium ionic liquids have been used to promote the intentional formation of oxygen vacancies especially in the case of TiO_2 or to form surface defects in the case of other materials such as ZnO, BiOBr, or $BiVO_4$. The existence of surface defects could suppress the recombination of photoinduced electron-hole pairs, which is crucial for the photoactivity of excited semiconductor material. Moreover, surface defects may appear to narrow the band gap (by creating new energy states in the band gag) and work as active sites, affecting finally observing reaction efficiency.

Finally, ionic liquids could serve as additives helpful in morphology control by influencing the type of facets/planes formed during synthesis, the thickness of the resulting nano- and microparticles, as well as their size and porosity.

Therefore, careful analysis of the ionic liquid's properties and their appropriate selection for the synthesis of semiconductor materials is a promising way of synthesizing materials with the desired photoactivity but requires further systematic research. It seems particularly desirable to use theoretical methods that allow predicting these interactions between the ionic liquid and the growing semiconductor particles, such as Virtual High Throughput Screening, including predictive multi-scale Molecular Modeling and Machine Learning based models.

Moreover, based on available literature we have diagnosed the following challenges for the future in this field:

1. The use of ionic liquids for the synthesis of semiconductor photocatalysts as a reagent that allows controlling the selectivity of obtained materials (e.g. obtaining photocatalysts possessing the assumed selectivity in the CO_2 photoreduction or alcohol oxidation reactions);
2. The employment of ionic liquids for the synthesis of semiconductor photocatalysts as a reagent allows obtaining photocatalysts activated by sunlight. Even if there are now reports of obtaining photocatalysts activated by light in the visible range, no studies

are showing whether such photocatalysts are useful for use on a larger scale and in the presence of solar radiation;

3. There is a lack of research showing whether photocatalysts obtained in the presence of ionic liquids are characterized by long-term stability, because the ionic liquid or its decay products - being on the surface of the photocatalyst - may undergo transformations in photocatalytic processes and thus affect its activity. This aspect would also require deeper research;
4. To understand the role of ionic liquids in the interaction with the semiconductor particle during its growth and in its use in the photocatalytic reaction – there is a need to have easily accessible data on the type of interactions and their strength between ionic liquids and their degradation products and the surface of semiconductors.

Author contributions

J. Ł. wrote the Sections 1 and 4. A. P. wrote the Sections 2 and 8. M. K. wrote the Sections 3 and 5. P. M. wrote the Sections 6 and 7. A. Z. M. wrote the Introduction and Conclusions parts. P. M. prepared the figure. A. P. and M. K. combined, formatted, and proofread the manuscript. J. Ł. and A. Z. M. led and coordinated the writing of this paper. All authors provided critical feedback and helped shape the manuscript.

Conflicts of Interest

The authors declare that they have no known competing financial interests or personal relationships that could have appeared to influence the work reported in this paper.

Acknowledgements

This research was supported by the Polish National Science Center under the grant 2021/41/B/ST4/00849.

References

1. Łuczak J, Paszkiewicz M, Krukowska A, Malankowska A, Zaleska-Medynska A. Ionic liquids for nano- and microstructures preparation. Part 1: Properties and multifunctional role. *Adv Colloid Interface Sci*. 2016;230:13-28. doi:10.1016/j.cis.2015.08.006

2. Paszkiewicz M, Łuczak J, Lisowski W, Patyk P, Zaleska-Medynska A. The ILs-assisted solvothermal synthesis of TiO2 spheres: The effect of ionic liquids on morphology and photoactivity of TiO2. *Appl Catal B Environ*. 2016;184:223-237. doi:10.1016/j.apcatb.2015.11.019

3. Mazierski P, Łuczak J, Lisowski W, Winiarski MJ, Klimczuk T, Zaleska-Medynska A. The ILs-assisted electrochemical synthesis of TiO2 nanotubes: The effect of ionic liquids on morphology and photoactivity. *Appl Catal B Environ*. 2017;214:100-113. doi:10.1016/j.apcatb.2017.05.005

4. Łuczak J, Paszkiewicz-Gawron M, Długokęcka M, et al. Visible-Light Photocatalytic Activity of Ionic Liquid TiO2 Spheres: Effect of the Ionic Liquid's Anion Structure. *ChemCatChem*. 2017;9(23):4377-4388. doi:10.1002/cctc.201700861

5. Gołąbiewska A, Checa-Suárez M, Paszkiewicz-Gawron M, et al. Highly active TiO2 microspheres formation in the presence of ethylammonium nitrate ionic liquid. *Catalysts*. 2018;8(7):279. doi:10.3390/catal8070279

6. Pancielejko A, Mazierski P, Lisowski W, Zaleska-Medynska A, Kosek K, Łuczak J. Facile Formation of Self-Organized TiO2 Nanotubes in Electrolyte Containing Ionic Liquid-Ethylammonium Nitrate and Their Remarkable Photocatalytic Properties. *ACS Sustain Chem Eng*. 2018;6(11):14510-14522. doi:10.1021/acssuschemeng.8b03154

7. Paszkiewicz-Gawron M, Długokęcka M, Lisowski W, et al. Dependence between Ionic Liquid Structure and Mechanism of Visible-Light-Induced Activity of TiO2 Obtained by Ionic-Liquid-Assisted Solvothermal Synthesis. *ACS Sustain Chem Eng*. 2018;6(3):3927-3937. doi:10.1021/acssuschemeng.7b04291

8. Paszkiewicz-Gawron M, Gołabiewska A, Pancielejko A, et al. Impact of tetrazolium ionic liquid thermal decomposition in solvothermal reaction on the remarkable photocatalytic properties of TiO2 particles. *Nanomaterials*. 2019;9(5):744. doi:10.3390/nano9050744

9. Pancielejko A, Mazierski P, Lisowski W, Zaleska-Medynska A, Łuczak J. Ordered TiO2 Nanotubes with Improved Photoactivity through Self-organizing Anodization with the Addition of an Ionic Liquid: Effects of the Preparation Conditions. *ACS Sustain Chem Eng*. 2019;7(18):15585-15596. doi:10.1021/acssuschemeng.9b03589

10. Rybińska-Fryca A, Mikolajczyk A, Łuczak J, et al. How thermal stability of ionic liquids leads to more efficient TiO2-based nanophotocatalysts: Theoretical and experimental studies. *J Colloid Interface Sci*. 2020;572:396-407. doi:10.1016/j.jcis.2020.03.079

11. Nitta A, Takase M, Takashima M, Murakami N, Ohtani B. A fingerprint of metal-oxide powders: Energy-resolved distribution of electron traps. *Chem Commun*. 2016;52(81):12096-12099. doi:10.1039/c6cc04999k

12. Łuczak J, Pancielejko A, Chen G, Takashima M, Zaleska-Medynska A, Ohtani B. How Do Ionic Liquids Affect the Surface Structure of Titania Photocatalyst? An Electron-Trap Distribution-Analysis Study. *J Phys Chem C*. 2021;125(51):28143-28149. doi:10.1021/acs.jpcc.1c09174

13. Duan X, Ma J, Lian J, Zheng W. The art of using ionic liquids in the synthesis of inorganic nanomaterials. *CrystEngComm*. 2014;16(13):2550-2559. doi:10.1039/c3ce41203b

14. Kaur N, Singh V. Current status and future challenges in ionic liquids, functionalized ionic liquids and deep eutectic solvent-mediated synthesis of nanostructured TiO2: a review. *New J Chem*. 2017;41(8):2844-2868. doi:10.1039/c6nj04073j

15. Hammond OS, Mudring AV. Ionic liquids and deep eutectics as a transformative platform for the synthesis of nanomaterials. *Chem Commun*. 2022;58(24):3865-3892. doi:10.1039/d1cc06543b

16. Sa N, Wu M, Wang HQ. Review of the role of ionic liquids in two-dimensional materials. *Front Phys*. 2023;18(4):43601. doi:10.1007/s11467-023-1258-6

17. Ohtani B. Photocatalysis A to Z-What we know and what we do not know in a scientific sense. *J Photochem Photobiol C Photochem Rev*. 2010;11(4):157-178. doi:10.1016/j.jphotochemrev.2011.02.001

18. Haouas M, Volkringer C, Loiseau T, Férey G, Taulelle F. In situ NMR, ex situ XRD and SEM study of the hydrothermal crystallization of nanoporous aluminum trimesates MIL-96, MIL-100, and MIL-110. *Chem Mater*. 2012;24(13):2462-2471. doi:10.1021/cm300439e

19. Gao M, Zhu L, Peh CK, Ho GW. Solar absorber material and system designs for photothermal water vaporization towards clean water and energy production. *Energy Environ Sci*.

2019;12(3):841-864. doi:10.1039/c8ee01146j

20. Asahi R, Morikawa T, Ohwaki T, Aoki K, Taga Y. Visible-light photocatalysis in nitrogen-doped titanium oxides. *Science (80-)*. 2001;293(5528):269-271. doi:10.1126/science.1061051

21. Di Valentin C, Pacchioni G, Selloni A, Livraghi S, Giamello E. Characterization of paramagnetic species in N-doped TiO 2 powders by EPR spectroscopy and DFT calculations. *J Phys Chem B*. 2005;109(23):11414-11419. doi:10.1021/jp051756t

22. Li J, Wu N. Semiconductor-based photocatalysts and photoelectrochemical cells for solar fuel generation: A review. *Catal Sci Technol*. 2015;5(3):1360-1384. doi:10.1039/c4cy00974f

23. Batzill M, Morales EH, Diebold U. Influence of nitrogen doping on the defect formation and surface properties of TiO2 rutile and anatase. *Phys Rev Lett*. 2006;96(2):026103. doi:10.1103/PhysRevLett.96.026103

24. Liu G, Zhao Y, Sun C, Li F, Lu GQ, Cheng HM. Synergistic effects of B/N doping on the visible-light photocatalytic activity of mesoporous TiO2. *Angew Chemie - Int Ed*. 2008;47(24):4516-4520. doi:10.1002/anie.200705633

25. Li F tang, Wang X jing, Zhao Y, et al. Ionic-liquid-assisted synthesis of high-visible-light-activated N-B-F-tri-doped mesoporous TiO2 via a microwave route. *Appl Catal B Environ*. 2014;144:442-453. doi:10.1016/j.apcatb.2013.07.050

26. Yu J, Li Q, Liu S, Jaroniec M. Ionic-liquid-assisted synthesis of uniform fluorinated B/C-codoped TiO 2 nanocrystals and their enhanced visible-light photocatalytic activity. *Chem - A Eur J*. 2013;19(7):2433-2441. doi:10.1002/chem.201202778

27. Ramanathan R, Bansal V. Ionic liquid mediated synthesis of nitrogen, carbon and fluorine-codoped rutile TiO2 nanorods for improved UV and visible light photocatalysis. *RSC Adv*. 2015;5(2):1424-1429. doi:10.1039/c4ra14510k

28. Liu SH, Syu HR. High visible-light photocatalytic hydrogen evolution of C,N-codoped mesoporous TiO2 nanoparticles prepared via an ionic-liquidtemplate approach. *Int J Hydrogen Energy*. 2013;38(32):13856-13865. doi:10.1016/j.ijhydene.2013.08.094

29. Tan X, Zhang J, Tan D, et al. Ionic liquids produce heteroatom-doped Pt/TiO2 nanocrystals for efficient photocatalytic hydrogen production. *Nano Res*. 2019;12(8):1967-1972. doi:10.1007/s12274-019-2466-9

30. Qiang Z, Liu X, Li F, et al. Iodine doped Z-scheme Bi2O2CO3/Bi2WO6 photocatalysts: Facile synthesis, efficient visible light photocatalysis, and photocatalytic mechanism. *Chem Eng J*. 2021;403:126327. doi:10.1016/j.cej.2020.126327

31. Zhao K, Khan I, Qi K, Liu Y, Khataee A. Ionic liquid assisted preparation of phosphorus-doped g-C3N4 photocatalyst for decomposition of emerging water pollutants. *Mater Chem Phys*. 2020;253:123322. doi:10.1016/j.matchemphys.2020.123322

32. Kowsari E, Ghezelbash MR. Synthesis of cactus-like zincoxysulfide (ZnOxS1-x) nanostructures assisted by a task-specific ionic liquid and their photocatalytic activities. *Mater Lett*. 2011;65(23-24):3371-3373. doi:10.1016/j.matlet.2011.07.078

33. Song H, Liu L, Feng B, et al. Modified g-C3N4 derived from ionic liquid and urea for promoting visible-light photodegradation of organic pollutants. *Chinese J Chem Eng*. 2021;40:293-303. doi:10.1016/j.cjche.2021.06.021

34. Xia J, Xu L, Zhang J, et al. Improved visible light photocatalytic properties of Fe/BiOCl microspheres synthesized via self-doped reactable ionic liquids. *CrystEngComm*. 2013;15(46):10132-10141. doi:10.1039/c3ce41555d

35. Li X, Wang B, Huang Y, et al. Boosting photocatalytic degradation of RhB via interfacial

electronic effects between Fe-based ionic liquid and g-C3N4. *Green Energy Environ*. 2019;4(2):198-206. doi:10.1016/j.gee.2019.02.002

36. Liu SH, Tang WT, Lin WX. Self-assembled ionic liquid synthesis of nitrogen-doped mesoporous TiO2 for visible-light-responsive hydrogen production. *Int J Hydrogen Energy*. 2017;42(38):24006-24013. doi:10.1016/j.ijhydene.2017.08.009

37. Di J, Chen J, Ji M, et al. Reactable ionic liquid induced homogeneous carbon superdoping of BiPO4 for superior photocatalytic removal of 4-chlorophenol. *Chem Eng J*. 2017;313:1477-1485. doi:10.1016/j.cej.2016.11.045

38. Saroj S, Singh L, Ranjan R, Singh SV. Enhancement of photocatalytic activity and regeneration of Fe-doped TiO 2 (Ti 1−x Fe x O 2) nanocrystalline particles synthesized using inexpensive TiO 2 precursor. *Res Chem Intermed*. 2019;45(4):1883-1906. doi:10.1007/s11164-018-3708-2

39. Khlyustova A, Sirotkin N, Kusova T, Kraev A, Titov V, Agafonov A. Doped TiO2: The effect of doping elements on photocatalytic activity. *Mater Adv*. 2020;1(5):1193-1201. doi:10.1039/d0ma00171f

40. Yan X, Ohno T, Nishijima K, Abe R, Ohtani B. Is methylene blue an appropriate substrate for a photocatalytic activity test? A study with visible-light responsive titania. *Chem Phys Lett*. 2006;429(4-6):606-610. doi:10.1016/j.cplett.2006.08.081

41. Bai S, Zhang N, Gao C, Xiong Y. Defect engineering in photocatalytic materials. *Nano Energy*. 2018;53:296-336. doi:10.1016/j.nanoen.2018.08.058

42. Künneth C, Batra R, Rossetti GA, Ramprasad R, Kersch A. Thermodynamics of phase stability and ferroelectricity from first principles. In: *Ferroelectricity in Doped Hafnium Oxide: Materials, Properties and Devices*. Elsevier; 2019:245-289. doi:10.1016/B978-0-08-102430-0.00006-1

43. Li G, Lian Z, Li X, et al. Ionothermal synthesis of black Ti3+-doped single-crystal TiO2 as an active photocatalyst for pollutant degradation and H2 generation. *J Mater Chem A*. 2015;3(7):3748-3756. doi:10.1039/c4ta02873b

44. Chen Y, Li W, Wang J, Gan Y, Liu L, Ju M. Microwave-assisted ionic liquid synthesis of Ti3+ self-doped TiO2 hollow nanocrystals with enhanced visible-light photoactivity. *Appl Catal B Environ*. 2016;191:94-105. doi:10.1016/j.apcatb.2016.03.021

45. Xiao S, Lu Y, Li X, et al. Hierarchically Dual-Mesoporous TiO2 Microspheres for Enhanced Photocatalytic Properties and Lithium Storage. *Chem - A Eur J*. 2018;24(50):13246-13252. doi:10.1002/chem.201801933

46. Wang L, Chang LX, Wei LQ, Xu SZ, Zeng MH, Pan SL. The effect of 1-N-alkyl chain of ionic liquids [Cnmim] +Br- (n = 2, 4, 6, 8) on the aspect ratio of ZnO nanorods: Syntheses, morphology, forming mechanism, photoluminescence and recyclable photocatalytic activity. *J Mater Chem*. 2011;21(39):15732-15740. doi:10.1039/c1jm12095f

47. Wei ZD, Wang R. Hierarchical BiOBr microspheres with oxygen vacancies synthesized via reactable ionic liquids for dyes removal. *Chinese Chem Lett*. 2016;27(5):769-772. doi:10.1016/j.cclet.2016.03.013

48. Wei Z, Li R, Wang R. Enhanced visible light photocatalytic activity of BiOBr by: In situ reactable ionic liquid modification for pollutant degradation. *RSC Adv*. 2018;8(15):7956-7962. doi:10.1039/c7ra13779f

49. da Trindade LG, Zanchet L, Trench AB, et al. Flower-like ZnO/ionic liquid composites: structure, morphology, and photocatalytic activity. *Ionics (Kiel)*. 2019;25(7):3197-3210. doi:10.1007/s11581-018-2822-x

50. Zou H, Li Z, Luan Y, et al. Fast synthesis of nanostructured ZnO particles from an ionic liquid precursor tetrabutylammonium hydroxide. *Curr Opin Solid State Mater Sci*. 2010;14(5):75-82. doi:10.1016/j.cossms.2010.03.001

51. Raula M, Biswas M, Mandal TK. Ionic liquid-based solvent-induced shape-tunable small-sized ZnO nanostructures with interesting optical properties and photocatalytic activities. *RSC Adv*. 2014;4(10):5055-5064. doi:10.1039/c3ra44859b

52. Liao H, Zhong J, Li J, Huang S, Duan R. Photocatalytic properties of flower-like BiOBr/BiOCl heterojunctions in-situ constructed by a reactable ionic liquid. *Inorg Chem Commun*. 2021;134:109063. doi:10.1016/j.inoche.2021.109063

53. Di J, Xia J, Yin S, et al. One-pot solvothermal synthesis of Cu-modified BiOCl via a Cu-containing ionic liquid and its visible-light photocatalytic properties. *RSC Adv*. 2014;4(27):14281-14290. doi:10.1039/c3ra45670f

54. Khan N, Wolff RN, Ullah H, et al. Ionic liquid based dopant-free band edge shift in BiVO4 particles for photocatalysis under simulated sunlight irradiation. *Mater Adv*. 2022;3(16):6485-6495. doi:10.1039/d2ma00259k

55. Zhao S, Dou Z, Liu Y, et al. Ionic liquid-assisted synthesis of defect-rich BiOI with controllable structure and high surface area for excellent visible-light photocatalytic activity. *Appl Organomet Chem*. 2020;34(10). doi:10.1002/aoc.5816

56. Rao F, Qin C, Zhong J, Li J. Oxygen vacancies facilitated visible light photoactivity of CdWO4 prepared by ionic liquid assisted hydrothermal method. *Ceram Int*. 2021;47(18):26572-26578. doi:10.1016/j.ceramint.2021.06.019

57. Wang L, Xu SZ, Li HJ, et al. Microbundles of zinc oxide nanorods: Assembly in ionic liquid [EMIM] +[BF4]-, photoluminescence and photocatalytic properties. *J Solid State Chem*. 2011;184(3):720-724. doi:10.1016/j.jssc.2011.01.032

58. Jin X, Dou L, Zhong J, Zhang S. Enhanced photocatalytic performance of three-dimensional microstructure Bi2SiO5 by ionic liquid assisted hydrothermal synthesis. *J Phys Chem Solids*. 2021;154:110063. doi:10.1016/j.jpcs.2021.110063

59. Tang X, Cai Z, Zhong JB, Li JZ, Ma D. Enhanced photocatalytic performance of biocl benefited from the effective separation of photogenerated carriers and enhanced surface hydroxyl content. *Desalin Water Treat*. 2020;203:230-237. doi:10.5004/dwt.2020.26223

60. Xia J, Zhao J, Chen J, et al. Facile fabrication of g-C3N4/BiPO4 hybrid materials via a reactable ionic liquid for the photocatalytic degradation of antibiotic ciprofloxacin. *J Photochem Photobiol A Chem*. 2017;339:59-66. doi:10.1016/j.jphotochem.2017.02.010

61. Zhang Y, Di J, Tong W, et al. Controllable synthesis of FeWO4/BiOBr in reactive ionic liquid with effective charge separation towards photocatalytic pollutant removal. *Res Chem Intermed*. 2019;45(2):437-451. doi:10.1007/s11164-018-3610-y

62. Zheng XW, Xiao ZH, Zhong JB, Hu W. Ionic liquid-assisted fabrication of ZnO with enhanced photocatalytic performance. *Appl Mech Mater*. 2013;361-363:722-725. doi:10.4028/www.scientific.net/AMM.361-363.722

63. Wang X jing, Wang Q, Li F tang, et al. Novel BiOCl-C3N4 heterojunction photocatalysts: In situ preparation via an ionic-liquid-assisted solvent-thermal route and their visible-light photocatalytic activities. *Chem Eng J*. 2013;234:361-371. doi:10.1016/j.cej.2013.08.112

64. Zhu S, Yang C, Li F, Li T, Zhang M, Cao W. Improved photocatalytic Bi2WO6/BiOCl heterojunctions: One-step synthesis via an ionic-liquid assisted ultrasonic method and first-principles calculations. *Mol Catal*. 2017;435:33-48. doi:10.1016/j.mcat.2017.03.016

65. Ren X, Wu K, Qin Z, Zhao X, Yang H. The construction of type II heterojunction of Bi2WO6/BiOBr photocatalyst with improved photocatalytic performance. *J Alloys Compd*. 2019;788:102-109. doi:10.1016/j.jallcom.2019.02.211

66. Li F tang, Wang Q, Wang X jing, et al. In-situ one-step synthesis of novel BiOCl/Bi24O31Cl10 heterojunctions via self-combustion of ionic liquid with enhanced visible-light photocatalytic activities. *Appl Catal B Environ*. 2014;150-151:574-584. doi:10.1016/j.apcatb.2014.01.009

67. Di J, Xia J, Yin S, et al. Preparation of sphere-like g-C3N4/BiOI photocatalysts via a reactable ionic liquid for visible-light-driven photocatalytic degradation of pollutants. *J Mater Chem A*. 2014;2(15):5340-5351. doi:10.1039/c3ta14617k

68. Yin S, Di J, Li M, et al. Ionic liquid-assisted synthesis and improved photocatalytic activity of p-n junction g-C3N4/BiOCl. *J Mater Sci*. 2016;51(10):4769-4777. doi:10.1007/s10853-016-9746-5

69. Li J hao, Ren J, Hao Y juan, et al. Construction of β-Bi2O3/Bi2O2CO3 heterojunction photocatalyst for deep understanding the importance of separation efficiency and valence band position. *J Hazard Mater*. 2021;401:123262. doi:10.1016/j.jhazmat.2020.123262

70. Zhao S, Zhang Y, Zhou Y, et al. Fabrication of sandwich-structured g-C3N4/Au/BiOCl Z-scheme photocatalyst with enhanced photocatalytic performance under visible light irradiation. *J Mater Sci*. 2018;53(8):6008-6020. doi:10.1007/s10853-018-1995-z

71. Hu Q, Yin S, Ding Y, et al. Ultrathin graphitic carbon nitride modified PbBiO2Cl microspheres with accelerating interfacial charge transfer for the photodegradation of organic contaminants. *Colloids Surfaces A Physicochem Eng Asp*. 2019;582:123804. doi:10.1016/j.colsurfa.2019.123804

72. Hu Q, Ji M, Di J, et al. Ionic liquid-induced double regulation of carbon quantum dots modified bismuth oxychloride/bismuth oxybromide nanosheets with enhanced visible-light photocatalytic activity. *J Colloid Interface Sci*. 2018;519:263-272. doi:10.1016/j.jcis.2018.02.057

73. Chang CJ, Lin YG, Chen J, Huang CY, Hsieh SC, Wu SY. Ionic liquid/surfactant-hydrothermal synthesis of dendritic PbS@CuS core-shell photocatalysts with improved photocatalytic performance. *Appl Surf Sci*. 2021;546:149106. doi:10.1016/j.apsusc.2021.149106

74. Wang Y, Feng S, Wu W, et al. Ionic liquid-assisted solvothermal construction of NH2-MIL-125(Ti)/BiOBr heterojunction for removing tetracycline under visible light. *Opt Mater (Amst)*. 2022;123:111817. doi:10.1016/j.optmat.2021.111817

75. Di J, Xia JX, Yin S, et al. Reactable ionic liquid assisted synthesis of Pd modified BiOBr flower-like microsphere with high dispersion and their enhanced photocatalytic performances. *Mater Technol*. 2015;30(2):113-121. doi:10.1179/1753555714Y.0000000226

76. Qin JH, Xu P, Huang YD, et al. High loading of Mn(ii)-metalated porphyrin in a MOF for photocatalytic CO2reduction in gas-solid conditions. *Chem Commun*. 2021;57(68):8468-8471. doi:10.1039/d1cc02847b

77. Guo J guo, Liu Y, Hao Y juan, et al. Comparison of importance between separation efficiency and valence band position: The case of heterostructured Bi3O4Br/A-Bi2O3 photocatalysts. *Appl Catal B Environ*. 2018;224:841-853. doi:10.1016/j.apcatb.2017.11.046

78. Cai Z, Zhong J, Li J. Ionic liquid assisted one-pot solvothermal preparation of BiOI/BiOBr heterojunctions with excellent photocatalytic activity. *Mater Lett*. 2020;271:127812. doi:10.1016/j.matlet.2020.127812

79. Xia J, Di J, Yin S, et al. Facile fabrication of the visible-light-driven Bi2WO 6/BiOBr composite with enhanced photocatalytic activity. *RSC Adv*. 2014;4(1):82-90. doi:10.1039/c3ra44191a

80. Wang B, Di J, Xia J, et al. Graphene-like BN/BiOBr composite: synthesis via a reactable ionic liquid and enhanced visible light photocatalytic performance. *Mater Technol*. 2016;31(8):463-470. doi:10.1080/10667857.2015.1105579

81. Di J, Xia J, Yin S, et al. A g-C3N4/BiOBr visible-light-driven composite: Synthesis via a reactable ionic liquid and improved photocatalytic activity. *RSC Adv*. 2013;3(42):19624-19631. doi:10.1039/c3ra42269k

82. Di J, Xia J, Ge Y, et al. Facile fabrication and enhanced visible light photocatalytic activity of few-layer MoS2 coupled BiOBr microspheres. *Dalt Trans*. 2014;43(41):15429-15438. doi:10.1039/c4dt01652a

83. Liu H, Yang C, Huang J, Chen J, Zhong J, Li J. Ionic liquid-assisted hydrothermal preparation of BiOI/BiOCl heterojunctions with enhanced separation efficiency of photo-generated charge pairs and photocatalytic performance. *Inorg Chem Commun*. 2020;113:107806. doi:10.1016/j.inoche.2020.107806

84. Di J, Xia J, Ji M, et al. Carbon quantum dots in situ coupling to bismuth oxyiodide via reactable ionic liquid with enhanced photocatalytic molecular oxygen activation performance. *Carbon N Y*. 2016;98:613-623. doi:10.1016/j.carbon.2015.11.015

85. Ji M, Xia J, Di J, et al. Ionic liquid-assisted bidirectional regulation strategy for carbon quantum dots (CQDs)/Bi4O5I2 nanomaterials and enhanced photocatalytic properties. *J Colloid Interface Sci*. 2016;478:324-333. doi:10.1016/j.jcis.2016.05.059

86. Sun M, Li F, Zhao F, et al. Ionic liquid-assisted fabrication of metal–organic framework-derived indium oxide/bismuth oxyiodide p-n junction photocatalysts for robust photocatalysis against phenolic pollutants. *J Colloid Interface Sci*. 2022;606:1261-1273. doi:10.1016/j.jcis.2021.08.132

87. Can E, Uralcan B, Yildirim R. Enhancing Charge Transfer in Photocatalytic Hydrogen Production over Dye-Sensitized Pt/TiO2by Ionic Liquid Coating. *ACS Appl Energy Mater*. 2021;4(10):10931-10939. doi:10.1021/acsaem.1c01553

88. Zaleska-Medynska A. *Metal Oxide-Based Photocatalysis: Fundamentals and Prospects for Application*. (Zaleska-Medynska A, ed.). Elsevier; 2018. doi:10.1016/C2016-0-01872-7

89. Macyk W, Szaciłowski K, Stochel G, Buchalska M, Kuncewicz J, Łabuz P. Titanium(IV) complexes as direct TiO2 photosensitizers. *Coord Chem Rev*. 2010;254(21-22):2687-2701. doi:10.1016/j.ccr.2009.12.037

90. Savić TD, Ćomor MI, Abazović ND, et al. Anatase nanoparticles surface modified with fused ring salicylate-type ligands (1-hydroxy-2-naphthoic acids): A combined DFT and experimental study. *J Alloys Compd*. 2015;630:226-235. doi:10.1016/j.jallcom.2015.01.041

91. Persson P, Bergstrom R, Lunell S. Quantum chemical study of photoinjection processes in dye-sensitized TiO2 nanoparticles. *J Phys Chem B*. 2000;104(44):10348-10351. doi:10.1021/jp002550p

92. Kim G, Choi W. Charge-transfer surface complex of EDTA-TiO2 and its effect on photocatalysis under visible light. *Appl Catal B Environ*. 2010;100(1-2):77-83. doi:10.1016/j.apcatb.2010.07.014

93. Ikeda S, Abe C, Torimoto T, Ohtani B. Photochemical hydrogen evolution from aqueous triethanolamine solutions sensitized by binaphthol-modified titanium(IV) oxide under visible-light irradiation. *J Photochem Photobiol A Chem*. 2003;160(1-2):61-67. doi:10.1016/S1010-

6030(03)00222-3

94. Kisch H. Tailoring of solid state electrical conductivity and optical electron transfer activation of dioxygen in solution through supramolecular charge-transfer interaction in ion pairs. *Coord Chem Rev*. 1997;159:385-396. doi:10.1016/s0010-8545(96)01312-4

95. Weisz AD, García Rodenas L, Morando PJ, Regazzoni AE, Blesa MA. FTIR study of the adsorption of single pollutants and mixtures of pollutants onto titanium dioxide in water: Oxalic and salicylic acids. *Catal Today*. 2002;76(2-4):103-112. doi:10.1016/S0920-5861(02)00210-9

96. Li SC, Wang JG, Jacobson P, Gong XQ, Selloni A, Diebold U. Correlation between bonding geometry and band gap states at organic-inorganic interfaces: Catechol on rutile TiO 2(110). *J Am Chem Soc*. 2009;131(3):980-984. doi:10.1021/ja803595u

97. Ojamäe L, Aulin C, Pedersen H, Käll PO. IR and quantum-chemical studies of carboxylic acid and glycine adsorption on rutile TiO2 nanoparticles. *J Colloid Interface Sci*. 2006;296(1):71-78. doi:10.1016/j.jcis.2005.08.037

98. Paszkiewicz-Gawron M, Makurat S, Rak J, et al. Theoretical and experimental studies on the visible light activity of Tio2 modified with halide-based ionic liquids. *Catalysts*. 2020;10(4):371. doi:10.3390/catal10040371

99. Hu S, Wang A, Li X, Wang Y, Löwe H. Hydrothermal synthesis of ionic liquid [Bmim]OH-modified TiO2 nanoparticles with enhanced photocatalytic activity under visible light. *Chem - An Asian J*. 2010;5(5):1171-1177. doi:10.1002/asia.200900629

100. Zhang Y, Pei Q, Feng T, et al. Ionic liquid-modified metal sulfides/graphene oxide nanocomposites for photoelectric conversion. *Appl Surf Sci*. 2015;346:194-200. doi:10.1016/j.apsusc.2015.03.213

101. Zhang Y, Li Q, Gao Q, Li J, Shen Y, Zhu X. An aspirated in-syringe device fixed with ionic liquid and β-cyclodextrin-functionalized CNTs/TiO2 for rapid adsorption and visible-light-induced photocatalytic activity. *New J Chem*. 2019;43(24):9345-9353. doi:10.1039/c9nj01602c

102. Kanai K, Nishi T, Iwahashi T, et al. Electronic structures of imidazolium-based ionic liquids. *J Electron Spectros Relat Phenomena*. 2009;174(1-3):110-115. doi:10.1016/j.elspec.2009.02.004

103. Fogarty RM, Palgrave RG, Bourne RA, et al. Electron spectroscopy of ionic liquids: Experimental identification of atomic orbital contributions to valence electronic structure. *Phys Chem Chem Phys*. 2019;21(35):18893-18910. doi:10.1039/c9cp02200g

104. Kanai K, Nishi T, Iwahashi T, et al. Anomalous electronic structure of ionic liquids determined by soft x-ray emission spectroscopy: Contributions from the cations and anions to the occupied electronic structure. *J Chem Phys*. 2008;129(22). doi:10.1063/1.3036925

105. Liu G, Yu JC, Lu GQ, Cheng HM. Crystal facet engineering of semiconductor photocatalysts: Motivations, advances and unique properties. *Chem Commun*. 2011;47(24):6763-6783. doi:10.1039/c1cc10665a

106. Tu W, Guo W, Hu J, et al. State-of-the-art advancements of crystal facet-exposed photocatalysts beyond TiO2: Design and dependent performance for solar energy conversion and environment applications. *Mater Today*. 2020;33:75-86. doi:10.1016/j.mattod.2019.09.003

107. Li R, Zhang F, Wang D, et al. Spatial separation of photogenerated electrons and holes among {010} and {110} crystal facets of BiVO 4. *Nat Commun*. 2013;4(1):1432. doi:10.1038/ncomms2401

108. Yu J, Low J, Xiao W, Zhou P, Jaroniec M. Enhanced photocatalytic CO2-Reduction activity of anatase TiO2 by Coexposed {001} and {101} facets. *J Am Chem Soc*. 2014;136(25):8839-

8842. doi:10.1021/ja5044787

109. Mao D, Lü X, Jiang Z, et al. Ionic liquid-assisted hydrothermal synthesis of square BiOBr nanoplates with highly efficient photocatalytic activity. *Mater Lett*. 2014;118:154-157. doi:10.1016/j.matlet.2013.12.049

110. Liu H, Liang Y, Hu H, Wang M. Hydrothermal synthesis of mesostructured nanocrystalline TiO2 in an ionic liquid-water mixture and its photocatalytic performance. *Solid State Sci*. 2009;11(9):1655-1660. doi:10.1016/j.solidstatesciences.2009.06.011

111. Antonietti M, Kuang D, Smarsly B, Zhou Y. Ionic liquids for the convenient synthesis of functional nanoparticles and other inorganic nanostructures. *Angew Chemie - Int Ed*. 2004;43(38):4988-4992. doi:10.1002/anie.200460091

112. Xia J, Di J, Li H, Xu H, Li H, Guo S. Ionic liquid-induced strategy for carbon quantum dots/BiOX (X=Br, Cl) hybrid nanosheets with superior visible light-driven photocatalysis. *Appl Catal B Environ*. 2016;181:260-269. doi:10.1016/j.apcatb.2015.07.035

113. Shahi SK, Kaur N, Singh V. Fabrication of phase and morphology controlled pure rutile and rutile/anatase TiO 2 nanostructures in functional ionic liquid/water. *Appl Surf Sci*. 2016;360:953-960. doi:10.1016/j.apsusc.2015.11.092

114. Alammar T, Smetana V, Pei H, Hamm I, Wark M, Mudring AV. The Power of Ionic Liquids: Crystal Facet Engineering of SrTiO3 Nanoparticles for Tailored Photocatalytic Applications. *Adv Sustain Syst*. 2021;5(2). doi:10.1002/adsu.202000180

115. Shah SJ, Wang R, Gao Z, et al. IL-assisted synthesis of defect-rich polyaniline/NH2-MIL-125 nanohybrids with strengthened interfacial contact for ultra-fast photocatalytic degradation of acetaldehyde under high humidity. *Chem Eng J*. 2021;411:128590. doi:10.1016/j.cej.2021.128590

116. Mohaghegh N, Eshaghi B, Rahimi E, Gholami MR. Ag2CO3 sensitized TiO2 nanoparticles prepared in ionic liquid medium: A new Ag2CO3/TiO2/RTIL heterostructure with highly efficient photocatalytic activity. *J Mol Catal A Chem*. 2015;406:152-158. doi:10.1016/j.molcata.2015.06.004

117. Schneider J, Matsuoka M, Takeuchi M, et al. Understanding TiO2photocatalysis: Mechanisms and materials. *Chem Rev*. 2014;114(19):9919-9986. doi:10.1021/cr5001892

118. Kundu S, Patra A. Nanoscale strategies for light harvesting. *Chem Rev*. 2017;117(2):712-757. doi:10.1021/acs.chemrev.6b00036

119. Liu X, Tang L, Zhou G, et al. In situ formation of BiVO4/MoS2 heterojunction: Enhanced photogenerated carrier transfer rate through electron transport channels constructed by graphene oxide. *Mater Res Bull*. 2023;157:112040. doi:10.1016/j.materresbull.2022.112040

120. Han CC, Ho SY, Lin YP, Lai YC, Liang WC, Chen-Yang YW. Effect of π-π stacking of water miscible ionic liquid template with different cation chain length and content on morphology of mesoporous TiO2 prepared via sol-gel method and the applications. *Microporous Mesoporous Mater*. 2010;131(1-3):217-223. doi:10.1016/j.micromeso.2009.12.026

121. Kowsari E, Abdpour S. In-situ functionalization of mesoporous hexagonal ZnO synthesized in task specific ionic liquid as a photocatalyst for elimination of SO2, NOx, and CO. *J Solid State Chem*. 2017;256:141-150. doi:10.1016/j.jssc.2017.08.038

122. Xia J, Yin S, Li H, Xu H, Xu L, Zhang Q. Enhanced photocatalytic activity of bismuth oxyiodine (BiOI) porous microspheres synthesized via reactable ionic liquid-assisted solvothermal method. *Colloids Surfaces A Physicochem Eng Asp*. 2011;387(1-3):23-28. doi:10.1016/j.colsurfa.2011.07.023

123. Nan Q, Huang S, Zhou Y, et al. Ionic liquid-assisted synthesis of porous BiOBr microspheres with enhanced visible light photocatalytic performance. *Appl Organomet Chem*. 2018;32(12). doi:10.1002/aoc.4596

124. Zhao R, Li X, Zhai Y, Li Q. Effect of chlorine source on the morphology of flower-like BiOCl and its photocatalytic activity. *J Adv Oxid Technol*. 2015;18(2):353-360. doi:10.1515/jaots-2015-0223

125. Dou L, Xiang Y, Zhong J, Li J, Huang S. Ionic liquid-assisted preparation of thin Bi2SiO5 nanosheets for effective photocatalytic degradation of RhB. *Mater Lett*. 2020;261:127117. doi:10.1016/j.matlet.2019.127117

126. Chen J, Xia J, Di J, et al. Reactable ionic liquid assisted synthesis of BiPO4 and the influences of solvent on structure, morphology and photocatalytic performance. *Colloids Surfaces A Physicochem Eng Asp*. 2016;488:110-117. doi:10.1016/j.colsurfa.2015.09.061

127. Alammar T, Hamm I, Grasmik V, Wark M, Mudring AV. Microwave-Assisted Synthesis of Perovskite SrSnO3 Nanocrystals in Ionic Liquids for Photocatalytic Applications. *Inorg Chem*. 2017;56(12):6920-6932. doi:10.1021/acs.inorgchem.7b00279

128. Lin C, Zhu M, Zhang T, et al. Cellulose/SnS2 composite with enhanced visible-light photocatalytic activity prepared by microwave-assisted ionic liquid method. *RSC Adv*. 2017;7(20):12255-12264. doi:10.1039/c7ra00558j

129. Ravishankar TN, Vaz M de O, Khan S, et al. Ionic Liquid Assisted Hydrothermal Syntheses of TiO2/CuO Nano-Composites for Enhanced Photocatalytic Hydrogen Production from Water. *ChemistrySelect*. 2016;1(10):2199-2206. doi:10.1002/slct.201600068

130. Ravishankar TN, De Oliveira Vaz M, Khan S, et al. Enhanced photocatalytic hydrogen production from Y2O3/TiO2 nano-composites: A comparative study on hydrothermal synthesis with and without an ionic liquid. *New J Chem*. 2016;40(4):3578-3587. doi:10.1039/c5nj03711e

131. Chao PY, Chang CJ, Lin KS, Wang CF. Synergistic effects of morphology control and calcination on the activity of flower-like Bi2WO6-Bi2O3 photocatalysts prepared by an ionic liquid-assisted solvothermal method. *J Alloys Compd*. 2021;883:160920. doi:10.1016/j.jallcom.2021.160920

132. Hu Q, Chen G, Wang Y, et al. Enhancing photocatalytic H2 evolution on In2S3/mesoporous TiO2 nanocomposites: Via one-pot microwave-assisted synthesis using an ionic liquid. *Nanoscale*. 2020;12(23):12336-12345. doi:10.1039/d0nr02958k

133. Yin S, Chen R, Ji M, et al. Construction of ultrathin MoS2/Bi5O7I composites: Effective charge separation and increased photocatalytic activity. *J Colloid Interface Sci*. 2020;560:475-484. doi:10.1016/j.jcis.2019.10.081

134. Yang C, Zhong J, Li J, Huang S, Duan R. In-situ construction of flower-like BiOBr/BiOCl heterojunctions assembled by thin sheets using an ionic liquid. *Mater Lett*. 2020;259:126766. doi:10.1016/j.matlet.2019.126766

135. Yang C, Li F, Li T. A one-step ionic liquid-assisted ultrasonic method for the preparation of BiOCl/m-BiVO4 heterojunctions with enhanced visible light photocatalytic activity. *CrystEngComm*. 2015;17(40):7676-7683. doi:10.1039/c5ce01312g

136. Lv H, Liu Y, Hu J, Li Z, Lu Y. Ionic liquid-assisted hydrothermal synthesis of Bi2WO6-reduced graphene oxide composites with enhanced photocatalytic activity. *RSC Adv*. 2014;4(108):63239-63245. doi:10.1039/c4ra11276h

137. Hu Q, Chen Y, Li M, et al. Construction of NH2-UiO-66/BiOBr composites with boosted photocatalytic activity for the removal of contaminants. *Colloids Surfaces A Physicochem Eng Asp*. 2019;579:123625. doi:10.1016/j.colsurfa.2019.123625

138. Fan C, Dong H, Liang Y, et al. Sustainable synthesis of HKUST-1 and its composite by biocompatible ionic liquid for enhancing visible-light photocatalytic performance. *J Clean Prod*. 2019;208:353-362. doi:10.1016/j.jclepro.2018.10.141

139. Chen Y, Su P, Liu X, et al. One-pot synthesis of 3D Cu2S-MoS2 nanocomposites by an ionic liquid-assisted strategy with high photocatalytic activity. *New J Chem*. 2019;43(1):269-276. doi:10.1039/c8nj05229h

140. Mohaghegh N, Rahimi E, Gholami MR. Ag3PO4/BiPO4 p-n heterojunction nanocomposite prepared in room-temperature ionic liquid medium with improved photocatalytic activity. *Mater Sci Semicond Process*. 2015;39:506-514. doi:10.1016/j.mssp.2015.05.066

141. Das S, Ghosh S. Fabrication of different morphologies of ZnO superstructures in presence of synthesized ethylammonium nitrate (EAN) ionic liquid: Synthesis, characterization and analysis. *Dalt Trans*. 2013;42(5):1645-1656. doi:10.1039/c2dt31920a

142. Díaz-Sánchez M, Reñones P, Mena-Palomo I, et al. Ionic liquid-assisted synthesis of F-doped titanium dioxide nanomaterials with high surface area for multi-functional catalytic and photocatalytic applications. *Appl Catal A Gen*. 2021;613:118029. doi:10.1016/j.apcata.2021.118029

143. Li Z, Sun L, Zhang J, Tang S. Controllable Synthesis of Zinc Oxide with Ionic Liquid and Supramolecular Gel as Co-Template for the Degradation of Organic Dyes. *SSRN Electron J*. 2022;39(12):3277-3285. doi:10.2139/ssrn.3996895

144. Tong LG, Liu JY, Wang CC, Rong H, Li W. Preparation of micro/nano ZnO pompons and their catalytic activity for the solar degradation of organic dyes. *Wuli Huaxue Xuebao/ Acta Phys - Chim Sin*. 2015;31(8):1615-1620. doi:10.3866/PKU.WHXB201505141

145. Barzegar M, Habibi-Yangjeh A, Behboudnia M. Template-free preparation and characterization of nanocrystalline ZnO in aqueous solution of [EMIM][EtSO4] as a low-cost ionic liquid using ultrasonic irradiation and photocatalytic activity. *J Phys Chem Solids*. 2009;70(10):1353-1358. doi:10.1016/j.jpcs.2009.07.025

146. Yang Y, Zhang Y, Zhou Y, et al. Ionic liquid-assisted synthesis of highly dispersive bowknot-like ZnO microrods for photocatalytic applications. *Appl Surf Sci*. 2017;400:269-276. doi:10.1016/j.apsusc.2016.12.168

147. Alammar T, Mudring AV. Sonochemical synthesis of 0D, 1D, and 2D zinc oxide nanostructures in ionic liquids and their photocatalytic activity. *ChemSusChem*. 2011;4(12):1796-1804. doi:10.1002/cssc.201100263

148. Wang L, Chang L, Zhao B, Yuan Z, Shao G, Zheng W. Systematic investigation on morphologies, forming mechanism, photocatalytic and photoluminescent properties of ZnO nanostructures constructed in ionic liquids. *Inorg Chem*. 2008;47(5):1443-1452. doi:10.1021/ic701094a

149. Shahi SK, Kaur N, Shahi JS, Singh V. Investigation of morphologies, photoluminescence and photocatalytic properties of ZnO nanostructures fabricated using different basic ionic liquids. *J Environ Chem Eng*. 2018;6(3):3718-3725. doi:10.1016/j.jece.2016.12.029

150. Huang S, Zhong J, Li J, et al. Charge separation and photocatalytic properties of BiOI prepared by ionic liquid-assisted hydrothermal method. *Mater Lett*. 2016;183:248-250. doi:10.1016/j.matlet.2016.07.119

151. Xia J, Yin S, Li H, Xu H, Xu L, Xu Y. Improved visible light photocatalytic activity of sphere-like BiOBr hollow and porous structures synthesized via a reactable ionic liquid. *Dalt Trans*. 2011;40(19):5249-5258. doi:10.1039/c0dt01511c

152. Chen Z, Zeng J, Di J, et al. Facile microwave-assisted ionic liquid synthesis of sphere-like

BiOBr hollow and porous nanostructures with enhanced photocatalytic performance. *Green Energy Environ*. 2017;2(2):124-133. doi:10.1016/j.gee.2017.01.005

153. Zhang J, Xia J, Yin S, et al. Improvement of visible light photocatalytic activity over flower-like BiOCl/BiOBr microspheres synthesized by reactable ionic liquids. *Colloids Surfaces A Physicochem Eng Asp*. 2013;420:89-95. doi:10.1016/j.colsurfa.2012.11.054

154. Zhao J, Ji M, Di J, et al. Synthesis of g-C3N4/Bi4O5Br2 via reactable ionic liquid and its cooperation effect for the enhanced photocatalytic behavior towards ciprofloxacin degradation. *J Photochem Photobiol A Chem*. 2017;347:168-176. doi:10.1016/j.jphotochem.2017.07.023

155. Xia J, Yin S, Li H, Xu H, Yan Y, Zhang Q. Self-assembly and enhanced photocatalytic properties of BiOI hollow microspheres via a reactable ionic liquid. *Langmuir*. 2011;27(3):1200-1206. doi:10.1021/la104054r

156. Ren JF, Li JZ, Song ZW. Ionic liquid-assisted synthesis of Bi12TiO20 nanostructures and their visible-light photocatalytic performance. *Mater Technol*. 2016;31(10):557-561. doi:10.1080/10667857.2016.1147129

157. Rabieh S, Bagheri M, Heydari M, Badiei E. Microwave assisted synthesis of ZnO nanoparticles in ionic liquid [Bmim]cl and their photocatalytic investigation. *Mater Sci Semicond Process*. 2014;26(1):244-250. doi:10.1016/j.mssp.2014.05.013

158. Ma D, Liu H, Huang J, Zhong J, Li J, Wang D. Improved photocatalytic performance of flower-like BiOBr/BiOCl heterojunctions prepared by an ionic liquid assisted one-step hydrothermal method. *Mater Lett*. 2019;238:147-150. doi:10.1016/j.matlet.2018.12.004

159. Wender H, Feil AF, Diaz LB, et al. Self-organized TiO 2 nanotube arrays: Synthesis by anodization in an ionic liquid and assessment of photocatalytic properties. *ACS Appl Mater Interfaces*. 2011;3(4):1359-1365. doi:10.1021/am200156d

160. Alammar T, Mudring AV. Sonochemical synthesis of 0D, 1D, and 2D zinc oxide nanostructures in ionic liquids and their photocatalytic activity. *ChemSusChem*. 2011;4(12):1796-1804. doi:10.1002/cssc.201100263

161. Haugen H, Will J, Köhler A, Hopfner U, Aigner J, Wintermantel E. Ceramic TiO2-foams: Characterisation of a potential scaffold. *J Eur Ceram Soc*. 2004;24(4):661-668. doi:10.1016/S0955-2219(03)00255-3

162. Chen Y, Zhang C, Huang W, et al. Synthesis of porous ZnO/TiO2 thin films with superhydrophilicity and photocatalytic activity via a template-free sol-gel method. *Surf Coatings Technol*. 2014;258:531-538. doi:10.1016/j.surfcoat.2014.08.042

163. Hoffmann MR, Martin ST, Choi W, Bahnemann DW. Environmental Applications of Semiconductor Photocatalysis. *Chem Rev*. 1995;95(1):69-96. doi:10.1021/cr00033a004

164. Park H, Park Y, Kim W, Choi W. Surface modification of TiO2 photocatalyst for environmental applications. *J Photochem Photobiol C Photochem Rev*. 2013;15(1):1-20. doi:10.1016/j.jphotochemrev.2012.10.001

165. Wang Y, Deng K, Zhang L. Visible light photocatalysis of BiOI and its photocatalytic activity enhancement by in situ ionic liquid modification. *J Phys Chem C*. 2011;115(29):14300-14308. doi:10.1021/jp2042069

166. Qadir MI, Zanatta M, Pinto J, et al. Reverse Semi-Combustion Driven by Titanium Dioxide-Ionic Liquid Hybrid Photocatalyst. *ChemSusChem*. 2020;13(20):5580-5585. doi:10.1002/cssc.202001717

167. Qi L, Yu J, Jaroniec M. Enhanced and suppressed effects of ionic liquid on the photocatalytic activity of TiO2. *Adsorption*. 2013;19(2-4):557-561. doi:10.1007/s10450-013-9478-7

168. Liu Y, Sun J, Huang H, et al. Improving CO2 photoconversion with ionic liquid and Co single atoms. *Nat Commun*. 2023;14(1):1457. doi:10.1038/s41467-023-36980-5

169. Pancielejko A, Łuczak J, Lisowski W, Zaleska-Medynska A, Mazierski P. Novel two-step synthesis method of thin film heterojunction of BiOBr/Bi2WO6 with improved visible-light-driven photocatalytic activity. *Appl Surf Sci*. 2021;569:151082. doi:10.1016/j.apsusc.2021.151082

170. Chen Y, Zhao Y, Yu B, et al. Visible Light-Driven Photoreduction of CO2 to CH4 over TiO2Using a Multiple-Site Ionic Liquid as an Absorbent and Photosensitizer. *ACS Sustain Chem Eng*. 2020;8(24):9088-9094. doi:10.1021/acssuschemeng.0c02333

171. Zhang G, Zhao X, Jin X, et al. Ionic-liquid-modified TiO2 spheres and their enhanced electrorheological responses. *J Mol Liq*. 2021;338:116696. doi:10.1016/j.molliq.2021.116696

172. Wu L, Xia Y, Xiong S, Wu H, Chen Z. Effect of ionic liquids modified nano-TiO2as additive on tribological properties of silicone grease. *Mater Res Express*. 2021;8(10):105011. doi:10.1088/2053-1591/ac0bd7

173. Holmberg JP, Ahlberg E, Bergenholtz J, Hassellöv M, Abbas Z. Surface charge and interfacial potential of titanium dioxide nanoparticles: Experimental and theoretical investigations. *J Colloid Interface Sci*. 2013;407:168-176. doi:10.1016/j.jcis.2013.06.015

174. Di J, Xiong J, Li H, Liu Z. Ultrathin 2D Photocatalysts: Electronic-Structure Tailoring, Hybridization, and Applications. *Adv Mater*. 2018;30(1). doi:10.1002/adma.201704548

175. Li M, Zhang H, Zhao Z, Wang P, Li Y, Zhan S. Inorganic Ultrathin 2D Photocatalysts: Modulation Strategies and Environmental/Energy Applications. *Accounts Mater Res*. 2023;4(1):4-15. doi:10.1021/accountsmr.2c00172

176. Zhao Y, Zhang S, Shi R, Waterhouse GIN, Tang J, Zhang T. Two-dimensional photocatalyst design: A critical review of recent experimental and computational advances. *Mater Today*. 2020;34:78-91. doi:10.1016/j.mattod.2019.10.022

177. Yang W, Zhang X, Xie Y. Advances and challenges in chemistry of two-dimensional nanosheets. *Nano Today*. 2016;11(6):793-816. doi:10.1016/j.nantod.2016.10.004

178. Ramalingam G, Kathirgamanathan P, Ravi G, et al. Quantum Confinement Effect of 2D Nanomaterials. In: *Quantum Dots - Fundamental and Applications*. IntechOpen; 2020. doi:10.5772/intechopen.90140

179. Wang H, Zhang X, Xie Y. Recent progress in ultrathin two-dimensional semiconductors for photocatalysis. *Mater Sci Eng R Reports*. 2018;130:1-39. doi:10.1016/j.mser.2018.04.002

180. Di J, Xia J, Ji M, et al. Controllable synthesis of Bi4O5Br2 ultrathin nanosheets for photocatalytic removal of ciprofloxacin and mechanism insight. *J Mater Chem A*. 2015;3(29):15108-15118. doi:10.1039/c5ta02388b

181. Di J, Xia J, Ji M, et al. Nitrogen-Doped Carbon Quantum Dots/BiOBr Ultrathin Nanosheets: In Situ Strong Coupling and Improved Molecular Oxygen Activation Ability under Visible Light Irradiation. *ACS Sustain Chem Eng*. 2016;4(1):136-146. doi:10.1021/acssuschemeng.5b00862

182. Jiang Q, Ji M, Chen R, et al. Ionic liquid induced mechanochemical synthesis of BiOBr ultrathin nanosheets at ambient temperature with superior visible-light-driven photocatalysis. *J Colloid Interface Sci*. 2020;574:131-139. doi:10.1016/j.jcis.2020.04.018

183. Pancielejko A, Łuczak J, Lisowski W, et al. Ionic liquid as morphology-directing agent of two-dimensional Bi2WO6: New insight into photocatalytic and antibacterial activity. *Appl Surf Sci*. 2022;599:153971. doi:10.1016/j.apsusc.2022.153971

184. Xia J, Ji M, Di J, et al. Construction of ultrathin C3N4/Bi4O5I2 layered nanojunctions via ionic

liquid with enhanced photocatalytic performance and mechanism insight. *Appl Catal B Environ*. 2016;191:235-245. doi:10.1016/j.apcatb.2016.02.058

185. Xia J, Ji M, Di J, et al. Improved photocatalytic activity of few-layer Bi4O5I2 nanosheets induced by efficient charge separation and lower valence position. *J Alloys Compd*. 2017;695:922-930. doi:10.1016/j.jallcom.2016.10.203

186. Tong W, Zhu L, Xia J, et al. One-pot ionic liquid-assisted strategy for GO/BiOI hybrids with superior visible-driven photocatalysis and mechanism research. *Mater Technol*. 2017;32(3):131-139. doi:10.1080/10667857.2016.1157914

187. Xia J, Ge Y, Di J, et al. Ionic liquid-assisted strategy for bismuth-rich bismuth oxybromides nanosheets with superior visible light-driven photocatalytic removal of bisphenol-A. *J Colloid Interface Sci*. 2016;473:112-119. doi:10.1016/j.jcis.2016.03.046

188. Lu X, Xu K, Tao S, et al. Engineering the electronic structure of two-dimensional subnanopore nanosheets using molecular titanium-oxide incorporation for enhanced photocatalytic activity. *Chem Sci*. 2016;7(2):1462-1467. doi:10.1039/c5sc03551a

189. Ji M, Di J, Ge Y, Xia J, Li H. 2D-2D stacking of graphene-like g-C 3 N 4 /Ultrathin Bi4O5Br2 with matched energy band structure towards antibiotic removal. *Appl Surf Sci*. 2017;413:372-380. doi:10.1016/j.apsusc.2017.03.287

190. Sun Y, Zheng W. Ultrathin SmVO4 nanosheets: Ionic liquid-assisted hydrothermal synthesis, characterization, formation mechanism and optical property. *Dalt Trans*. 2010;39(30):7098-7103. doi:10.1039/c002626c